

**UNCLASSIFIED**

---

---

**AD 269 387**

*Reproduced  
by the*

**ARMED SERVICES TECHNICAL INFORMATION AGENCY  
ARLINGTON HALL STATION  
ARLINGTON 12, VIRGINIA**



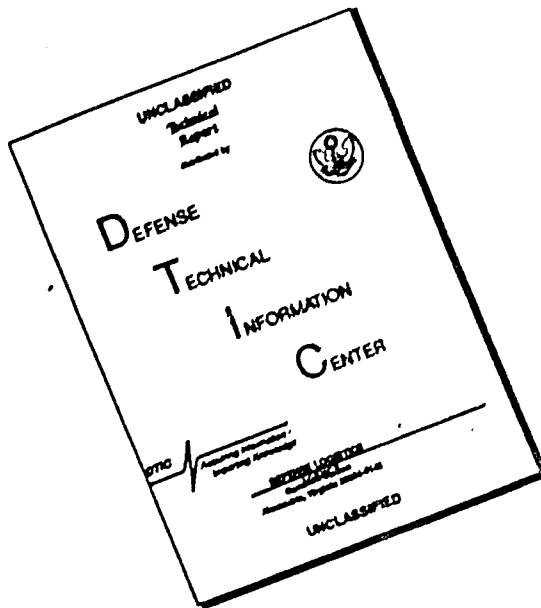
---

---

**UNCLASSIFIED**

NOTICE: When government or other drawings, specifications or other data are used for any purpose other than in connection with a definitely related government procurement operation, the U. S. Government thereby incurs no responsibility, nor any obligation whatsoever; and the fact that the Government may have formulated, furnished, or in any way supplied the said drawings, specifications, or other data is not to be regarded by implication or otherwise as in any manner licensing the holder or any other person or corporation, or conveying any rights or permission to manufacture, use or sell any patented invention that may in any way be related thereto.

# **DISCLAIMER NOTICE**



**THIS DOCUMENT IS BEST  
QUALITY AVAILABLE. THE COPY  
FURNISHED TO DTIC CONTAINED  
A SIGNIFICANT NUMBER OF  
PAGES WHICH DO NOT  
REPRODUCE LEGIBLY.**

269387

FINAL REPORT  
AFOSR 1904  
DECEMBER 1961

AIR FORCE OFFICE OF SCIENTIFIC RESEARCH  
CONTRACT AF49(638)-413

# OBSERVED EMISSITIVES OF ROCKET COMBUSTION GASES

BY D. E. ROBISON AND S. J. VAN GROUW

FLIGHT PROPULSION LABORATORY DEPARTMENT  
GENERAL  ELECTRIC  
CINCINNATI 15, OHIO

Final Report  
AFOSR 1904  
December 1961

OBSERVED EMISSIVITIES  
OF  
ROCKET COMBUSTION GASES

By

D. E. Robison  
S. J. Van Grouw

Air Force Office of Scientific Research  
Contract AF 49(638)-413

Flight Propulsion Laboratory Department  
General Electric Company

Cincinnati, Ohio

#### ACKNOWLEDGEMENT

The investigation of thermal radiation from rocket combustion gases reported herein was initiated in 1958 under contract with the Air Force Office of Scientific Research and has for the past three years been supported by this office. The work was carried out with research equipment and facilities furnished by the General Electric Company, Flight Propulsion Laboratory Department.

That any useful data have been derived at all from this work is due in large measure to the tireless efforts of

G. R. Brown  
M. W. Cook  
A. D. Howard  
I. Segalman  
J. G. Spraul  
M. E. Streetman

each of whom was connected with this problem at one time or another during the contract period, in either developing the necessary apparatus, instrumentation, testing, and calculating procedures, or in carrying out the experiments.

Special acknowledgement is due Mr. Howard for doing most of the detail design work on the combustion hardware and for his close assistance in completing the calculations and drawings necessary for this report.

The authors are indebted to Mr. Spraul for his original work in setting up the data reduction procedures, for his early assistance in developing the laboratory facilities, and later for assisting Mr. Cook in carrying out the experiments.

The data reduction and other calculation procedures that were developed for

the digital computer were programmed by Mrs. Marcia Streetman, to whom the authors wish to express their sincere gratitude. Our thanks are also extended to Mrs. Doris Warlick for calculating the theoretical composition and performance data.

The authors also wish to thank Miss Barbara West for her patience and forbearance in typing the manuscript.

## TABLE OF CONTENTS

	Page
INTRODUCTION.....	1
SUMMARY OF RESULTS.....	2
Observed Spectral Intensity.....	7
Total Emissivity.....	13
Pressure Correction Factor.....	19
Absorption Coefficient.....	21
EXPERIMENTAL METHOD.....	37
THEORETICAL CONSIDERATIONS.....	51
Measured Emissivity.....	51
Reflected Intensity.....	65
True Emissivity.....	74
Effective Beam Length.....	75
COMBUSTION TEMPERATURE.....	81
Thermodynamic Temperature.....	81
Approximate State Paths.....	94
Average Combustion Temperature.....	99
CALIBRATION AND CORRECTIONS.....	101
Calibration.....	101
Corrections.....	106
LIST OF PRINCIPAL SYMBOLS.....	116
REFERENCES.....	119
APPENDIX A: PERFORMANCE AND PROPELLANT DATA.....	120

## LIST OF FIGURES

Figure	Page
1. Schematic Diagram of Detector Arrangement.....	3
2. Spectral Intensity for Combustion Products..... of Nitric Acid and Ammonia	8
3. Spectral Intensity for Combustion Products..... of Nitrogen Tetroxide and Ammonia	10
4. Spectral Intensity for Combustion Products..... of Nitrogen Tetroxide and Hydrazine	11
5. Measured Emissivities.....	14
6. Corrected Emissivity.....	18
7. Extrapolation of Pressure Correction Factor.....	20
8. Effective Absorption Coefficient.....	22
1.1 Experimental Flow System.....	38
1.2 Instrument Console.....	39
1.3 Control Console.....	40
1.4 Thrust Chamber Assembly.....	42
1.5 Spectrometer System.....	44
1.6 Spectrometer Amplifying and Recording System.....	45
1.7 Cross Section of Laboratory Blackbody.....	48
1.8 Experimental Apparatus with Blackbody..... in Position for Calibration	49
1.9 Experimental Apparatus Ready for Test.....	50
2.1 Chamber Geometry.....	51
2.2 Typical Spectral Distribution.....	52
2.3 Effective Cylindrical Volume.....	55

**LIST OF FIGURES (Continued)**

Figure	Page
2.4 Cone of View.....	59
2.5 Polar Coordinate System.....	66
2.6 Empirical Fit of $e^{-\mu r}$ .....	68
2.7 Effective Beam Length.....	76
3.1 Measured Variables.....	82
3.2 Application of First Law.....	84
3.3 Geometry Assumed for Heat Transfer.....	89
3.4 Heat Flow and Temperature Functions.....	90
3.5 Approximate Path.....	94
4.1 Chart Trace of Calibration Curves and Gas Emission for Run 50	102
4.2 Thermopile Calibration.....	104
4.3 Pyrometer Calibration.....	105
4.4 Effect of Back Wall Reflection on the Observed Emissivity	107
4.5 Effect of Back Wall Reflection on the Observed Emissivity	108
5.1 Theoretical Performance at 700 psia for $\text{HNO}_3-\text{NH}_3 + .84\% \text{ N}_2$	121
5.2 Performance Characteristics of $\text{N}_2\text{O}_4-\text{NH}_3 + .9\% \text{ N}_2$	122
5.3 Theoretical Performance of $\text{N}_2\text{O}_4-\text{N}_2\text{H}_4 + 1\% \text{ N}_2$	123
5.4 Theoretical Flame Temperature for $\text{N}_2\text{O}_4-(\text{N}_2\text{H}_4 + 1.7\% \text{ H}_2\text{O}) + 1\% \text{ N}_2$	124

## LIST OF TABLES

Table	Page
1. Measured and Corrected Emissivity Data.....	5
2. Wavelengths of Maximum and Minimum Intensities.....	12
3. Measured Spectral Properties.....	25
4. Calculated Values of $\epsilon_m$ from Eqs. (2.60) and (2.71).....	73
5. Parameters for Calculating Combustion Temperature.....	98
6. Spectral Properties Based on a Background..... Reflectivity of $f_\lambda = 0.24$ .	110
7. Typical Propellant Composition.....	125
8. List of Experimental Tests.....	126
9. Propellant Specifications.....	129

## INTRODUCTION

Radiation from combustion gases is an important engineering consideration in many industrial applications, but it achieves special significance in rocket engines because of the unusually high gas pressures and temperatures that are employed. The fact that many of the molecular species that appear in rocket and jet engine combustion gases have strong radiation bands in the infra-red region of the spectrum has been recognized for decades. Yet, remarkably little practical information is available today that is directly applicable to radiation from combustion products, particularly for high pressures and temperatures. Significant progress has been made in the past few years toward extending the theory (1, 2, 3) of spectral emission from gases. However, much of this work applies to the molecular aspects of pure monatomic or diatomic species, and is difficult to apply to complex mixtures. Very little is actually known about the radiation from mixtures, other than that an anomalous behavior is not unusual. The situation is complicated further by the fact that there are practically no experimental data from which to derive even empirical correlations for high pressure radiating systems.

Water vapor is one of the most important of the radiating gases. This product is formed in high concentrations by nearly every major rocket or jet propellant fuel in use today, and it has one of the highest emissivities. It also happens to be one of the most difficult of the emitters to treat analytically. Until recently, the charts developed by Hottel (4) offered the only practical means of estimating the emissivity of water vapor or mixture containing water vapor. However, this work is far too limited for reliable application to the

extreme conditions found in rocket chambers. Hottel's correlations are based on experimental data, but the data were obtained at pressures of less than 10 atm and temperatures below 3500°R. The use of these charts for present day rocket combustion systems requires extrapolation to pressures and temperatures of up to 100 atm and 6000°R.

The subject of gas radiation has been reviewed and extended considerably recently by Penner<sup>(1)</sup> in a comprehensive treatment of the statistical theory of spectral emission in gases. Close agreement between theory and experiment is shown for diatomic gases, but as Penner points out, emissivity calculations from first principles are virtually impossible for triatomic molecules such as H<sub>2</sub>O. Reasonable approximations of the emissivities of H<sub>2</sub>O appear to be possible presently only through semi-empirical correlations of experimental data. Penner develops correlations of this type for pure water vapor. However, the adjustable parameters that appear in his correlations are based on the low pressure (.5 atm) data of Hottel, and cannot be applied with certainty to mixtures at high pressures without additional experimental data. There is an obvious need for experimental data in this area.

#### SUMMARY OF RESULTS

The broad objective of the present experiments was to measure the total and the spectral intensity of the radiation emitted by rocket combustion products at high pressures. This report presents measured spectral and total radiation data for three rocket propellant systems; namely, nitric acid and ammonia, nitrogen tetroxide and ammonia, and nitrogen tetroxide and hydrazine. Each of these combinations contains H<sub>2</sub>O as the principal radiating gas. The radiation measurements

were made at nominal combustion pressure of 700 psia. Total emissivity correlations are developed and compared with the values predicted by Hottel. In addition, methods are developed for approximating the effective beam length and the effect of reflection from combustion chamber walls, and for estimating the temperature of the combustion gas from performance data. No consideration is given in this report to the calculation of gas emissivities from statistical or quantum theory.

The radiation measurements were obtained by a direct observation of the high temperature gases contained inside the combustion chamber of a small rocket motor. A special technique was developed to accomplish this. The essential elements of the method employed for observing the gas are shown in Fig. 1. The gas inside the chamber was viewed through a disk collimator and a small (.070 in. dia) aperture in the chamber wall. Outward flow of the hot combustion gases through the aperture was prevented by forcing a small flow of nitrogen gas into the chamber through the collimator and the aperture.

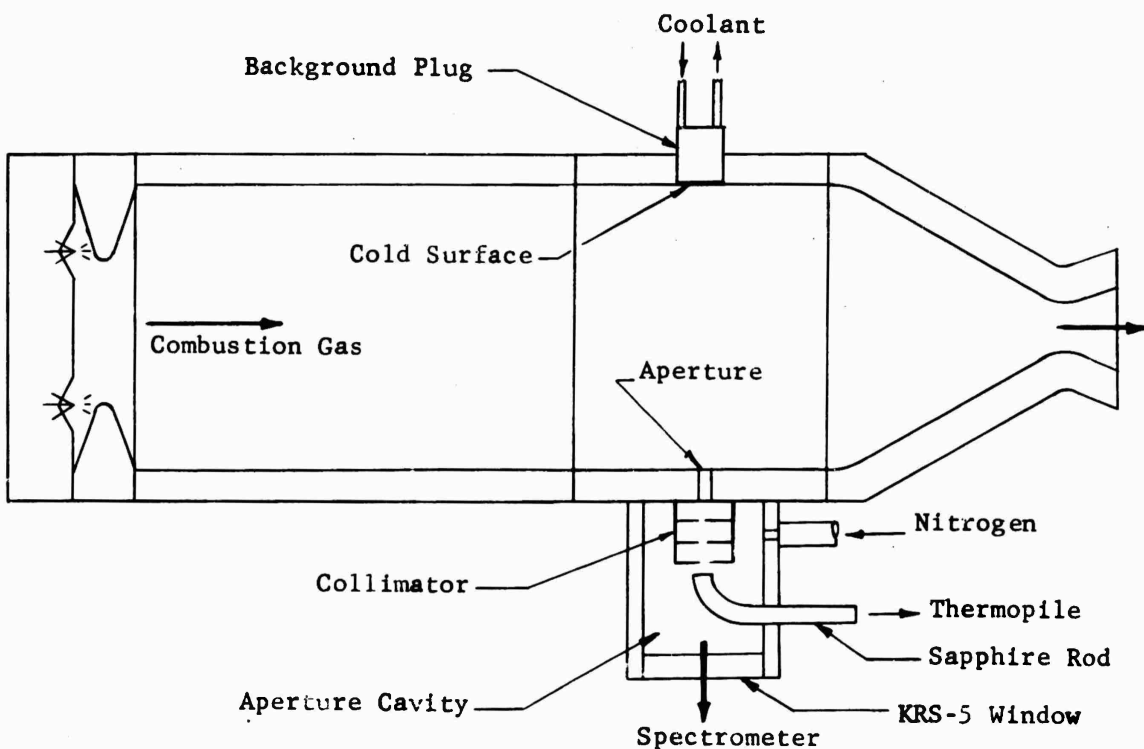


Fig. 1 Schematic Diagram of Detector Arrangement

Two instruments were employed for detecting the intensity of the radiation. The total intensity was measured by means of a thermopile. Fig. 1 does not show the thermopile, but it was coupled to the end of the 1/8 in. sapphire rod that protrudes through the wall of the cavity. The radiation that emanated from the disk collimator was "piped" directly to the thermopile element by means of the curved sapphire rod. Measurements of the spectral intensity were obtained by observing the gas through the same aperture with a high-speed recording spectrometer. The spectrometer was contained in an evacuated chamber which was isolated from the thermopile cavity by the KRS-5 window shown in Fig. 1. The absolute intensity of the gas emission was determined by comparing the detector output created by the gas radiation with the output created by a laboratory blackbody radiating through the same aperture. The black radiation was directed through the aperture before and after each run, but not during the run.

Out of a total of 56 test runs, only 13 provided usable data. At least four usable experiments were obtained for each propellant combination. The experimental data derived from these tests are listed in Table 1. The table shows the measured and the corrected emissivities as well as the pertinent performance variables. The measured combustion pressure is denoted by  $p_c$ . The symbol  $T_c$  denotes the combustion temperature calculated from the performance and heat transfer data. The concentrations of water vapor and molecular hydrogen are designated as  $(H_2O)$  and  $(H_2)$ . As a matter of interest, the table also presents the propellant mixture ratio O/F (by weight), the ratio of  $T_c$  to the theoretical value  $T'_c$  and the calculated gas density .

It will be noted that except for Run 41, the chamber pressure did not depart significantly from 700 psia for the first two propellant systems. However, a variation of approximately 22% was obtained for the  $N_2O_4-N_2H_4$  combination. For the range of mixture ratios achieved in the usable experiments, the three

Table 1. Measured and Corrected Emissivity Data

Run	O/F	C*	P <sub>C</sub>	T <sub>C</sub> °R	T <sub>C</sub> /T' <sub>C</sub>	R	ρ × 10 <sup>4</sup> lb/in. <sup>3</sup>	(H <sub>2</sub> O)	(H <sub>2</sub> )	m <sub>g</sub> (N <sub>2</sub> ) lb/sec
		ft/sec	psia			in lb <sub>f</sub> / 1b °R				
<b>HNO<sub>3</sub> - NH<sub>3</sub></b>										
41	2.71	2283	398	4184	.935	903.6	1.690	.630	.0020	
43	2.11	5005	696.7	4563	.957	958.6	1.749	.6536	.0358	.0191
45	1.82	4792	691.4	4123	.934	860.3	1.901	.5878	.1109	.0188
46	2.74	4611	686.5	4198	.935			.6105	.0218	.0181
<b>N<sub>2</sub>O<sub>4</sub> - NH<sub>3</sub></b>										
47	1.63	5110	692.8	4652	.944	951.7	1.565	.5198	.1262	.0186
48	1.95	5216	702.6	5100	.962	876.0	1.573	.5793	.0366	.0195
49	1.98	5274	700.1	5150	.969	877.5	1.549	.5734	.0353	.0193
50	1.61	5291	694.0	4841	.988	946.3	1.515	.5132	.1307	.0189
<b>N<sub>2</sub>O<sub>4</sub> - N<sub>2</sub>H<sub>4</sub></b>										
51	1.11	5618	607.5	5381	.967	940.0	1.201	.4298	.1318	.0188
53	1.27	5596	614.7	5486	.973	902.9	1.241	.4465	.0877	.0185
54	1.38	5514	698.2	5541	.969	875.3	1.440	.4649	.0592	.0192
55	1.75	5584	666.8	5632	1.009	846.3	1.399	.4106	.0580	.0204
56	1.21	5632	764.4	5509	.978	912.6	1.520	.4467	.0997	.0185

TABLE 1 (Continued)

Run	$\epsilon_{ms}$	$\epsilon_{mt}$	$B_{va}$	$B_{vb}$	$B_{vc}$	$\bar{\epsilon}$	$\epsilon_t$	$\epsilon_s$	$p_d e$ ft atm	$\epsilon_{cs}$	$\epsilon_{ct}$
1.14 $\mu$											
				5.5 $\mu$	10 $\mu$	5.5-10 $\mu$					
41	.3965	.5380	.192	.9537	.9908	.7	.440	.3803	6.10	.516	
43	.3883	.5570	.250	.9618	.9930	.700	.4213	.3803	11.08	.407	.393
45	.4575	.6065	.183	.9520	.9906	.934	.5069	.4531	9.89	.508	.454
46	.4529	.3923	.194	.9536	.9911	.998	.3306	.4349	10.20	.329	.432
$N_2O_4-NH_3$											
47	.5057	.261	.9640	.9932	.89	.3844			8.76	.448	
48	.346	.4172	.327	.9716	.9946	.785	.2895	.3433	9.90	.290	.344
49		.4778	.333	.9722	.9947	.78	.3249		9.76	.327	
50	.3751	.4165	.320	.9683	.9939	.885	.2962	.3718	8.66	.310	.389
$N_2O_4-N_2H_4$											
51		.2876	.363	.9755	.9951	.8	.1954		6.35	.226	
53	.2290	.3945	.378	.9765	.9952	.827	.2539	.2268	6.68	.289	.258
54	.2320	.3552	.382	.9770	.9953	.774	.2279	.2294	7.94	.246	.247
55		.3263	.396	.9784	.9954	.8	.2061		6.66	.236	
56		.3725	.380	.9768	.9952	.8	.2391		8.31	.254	

propellant systems provide combustion temperatures of  $4100^{\circ}\text{R}$  to  $5700^{\circ}\text{R}$ , with  $\text{H}_2\text{O}$  concentrations of 0.65 to 0.41.

The ratio of the observed intensity emitted from the chamber to the observed intensity produced by the blackbody radiating at the calculated gas temperature is called the measured emissivity, and is denoted by  $\epsilon_m$  in Table 1. This is not the true emissivity of the gas, since the observed radiation also includes the radiation reflected from the background plate. The true emissivity of the gas is denoted by  $\epsilon$ . This value includes several corrections in addition to the correction for reflection. The corrections are explained later in the report. The subscript s designates the emissivities derived from the spectrometer data, and the subscript t designates the emissivities determined from the thermopile data.

Observed Spectral Intensity. The spectral intensity was measured for at least two different operating conditions for each propellant combination. Except for Run 54, each spectral curve was obtained with a Beckman IR-2 monochrometer, using a KBR prism and a slit width of 1.2 mm. The spectral data for Run 54 was obtained with a different IR-2 monochrometer, using a NaCl prism and a slit width of 0.8 mm. Both monochrometers were equipped with Golay detectors.

The spectral intensity of the radiation emitted by the products of the nitric acid and ammonia system is shown in Fig. 2 for two different mixture ratios. The monochromatic intensity, ( $I_\lambda$ ), is compared with the intensity of black radiation ( $B_\lambda$ ) at the combustion temperature. According to Penner<sup>(1)</sup>, the principal band centers for  $\text{H}_2\text{O}$  emission are reported to occur at  $1.1\mu$ ,  $1.38\mu$ ,  $1.87\mu$ ,  $2.7\mu$ ,  $6.3\mu$ , and  $20\mu$ . The band at  $1.1\mu$  is relatively weak. From the data of Howard, Burch and Williams<sup>(6)</sup>, Penner obtains an integrated absorption of  $\alpha_i = 0.32 \text{ cm}^{-2} \text{ atm}^{-1}$  compared with  $378 \text{ cm}^{-2} \text{ atm}^{-1}$  for the sum of the

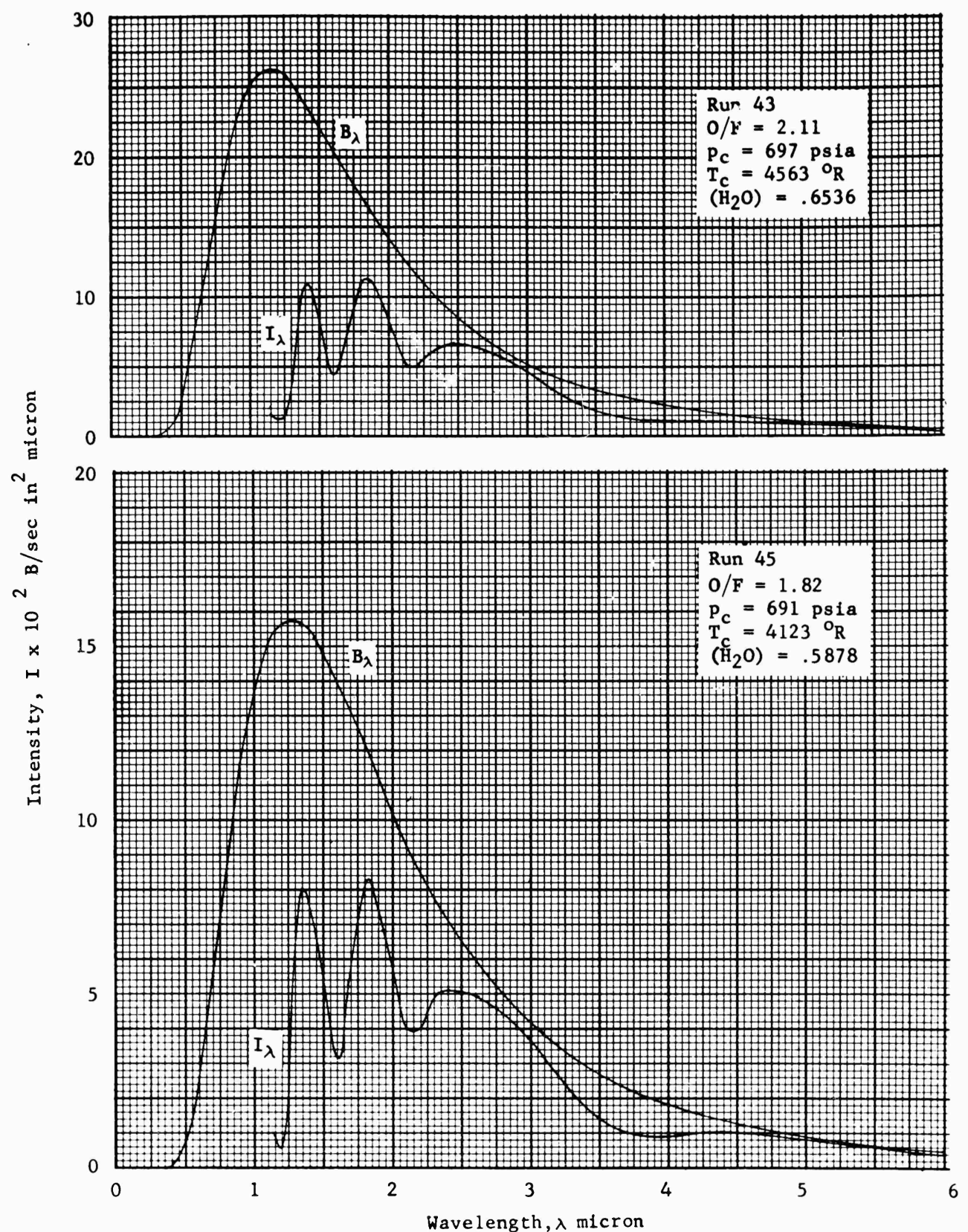


Fig. 2. Spectral Intensity for Combustion Products  
of Nitric Acid and Ammonia  
 $(HNO_3 + 1.05\% H_2O) + NH_3 + .84\% N_2 \rightarrow$  Products

absorptions for the other bands for  $600^{\circ}\text{R}$  and 0.5 atm. Thus, the  $1.1\mu$  band should emit less than 0.1% of the total energy. Reference (7) also shows an even weaker band at about  $0.94\mu$ . It will be seen in Fig. 2 that the spectral curve extends only to  $1.14\mu$ . This value represents the lower scanning limit of the spectrometer, and unfortunately it was not possible to obtain data at lower wavelengths. Nevertheless, it appears that roughly a third or more of the  $1.1\mu$  band is represented anyway, and the error in the total emissivity due to ignoring the energy below  $1.14\mu$  is negligibly small. It will be noted that the maximum band intensities fall remarkably close to the wavelengths given above for the  $1.38\mu$  and  $1.87\mu$  band centers. The agreement is not so good for the  $2.7\mu$  band. The maximum intensity of this band occurs at  $2.4\mu$  rather than  $2.7\mu$  in both runs.

The emission characteristics of the nitrogen tetroxide and ammonia products are plotted in Fig. 3. The distribution of energy in the spectrum for this system is quite similar to that for the nitric acid and ammonia combination. The only significant difference is that the band that occurs between  $2\mu$  and  $3\mu$  peaks rather sharply at  $2.25\mu$ . The shape of the curve in this region has the character of two overlapping bands, one centered at  $2.25\mu$ , the other centered at approximately  $2.6\mu$ . However, there is no other evidence to support such an assumption. The combustion products for this system are not significantly different than those produced by the nitric acid ammonia propellants.

The spectral radiation emitted by the nitrogen tetroxide and hydrazine products is presented in Fig. 4. The character of the spectral curves for these propellants differs little from that of the nitric acid and ammonia products

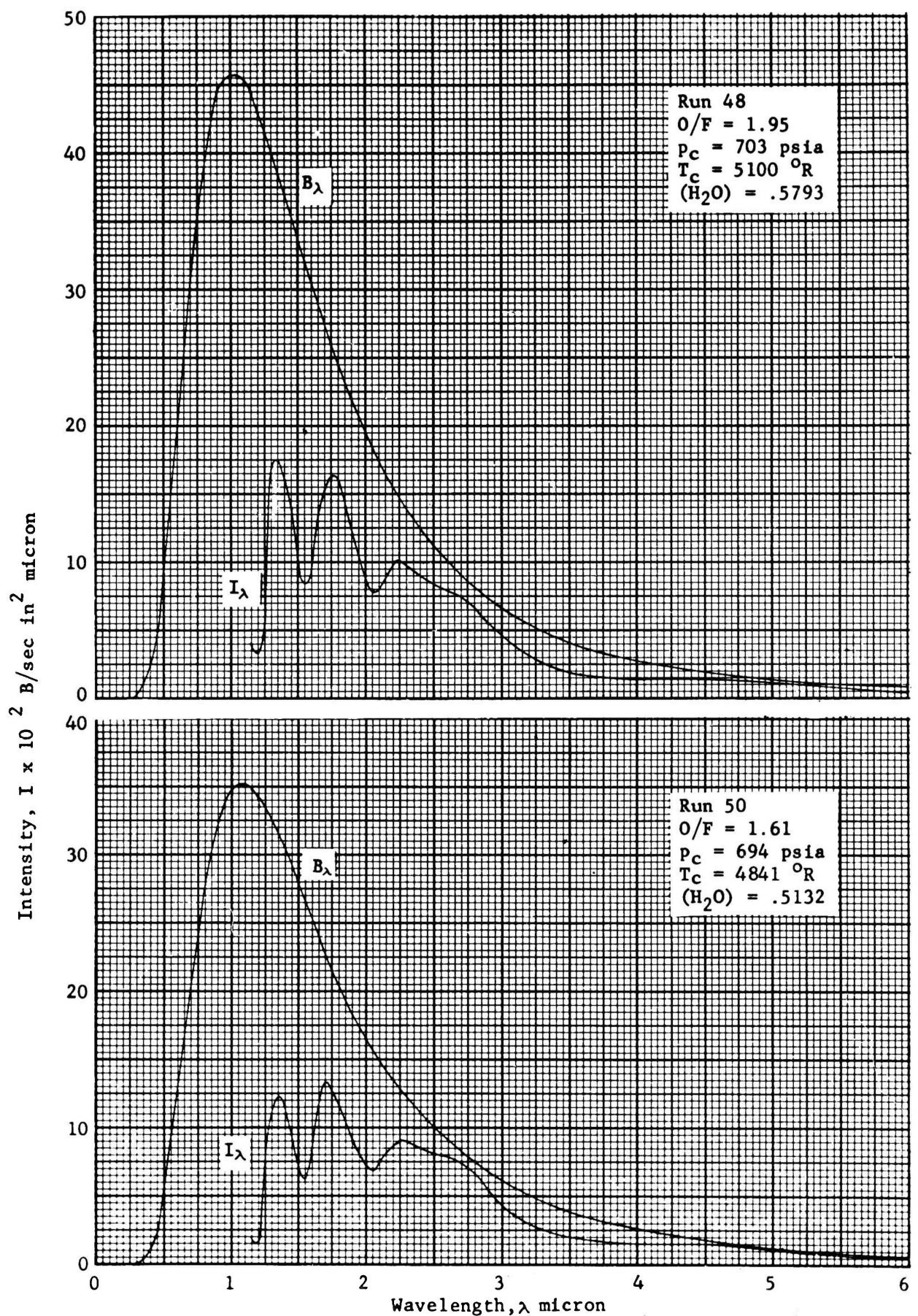


Fig. 3. Spectral Intensity for Combustion Products  
of Nitrogen Tetroxide and Ammonia  
 $N_2O_4 + NH_3 + .9\% N_2 \rightarrow \text{Products}$

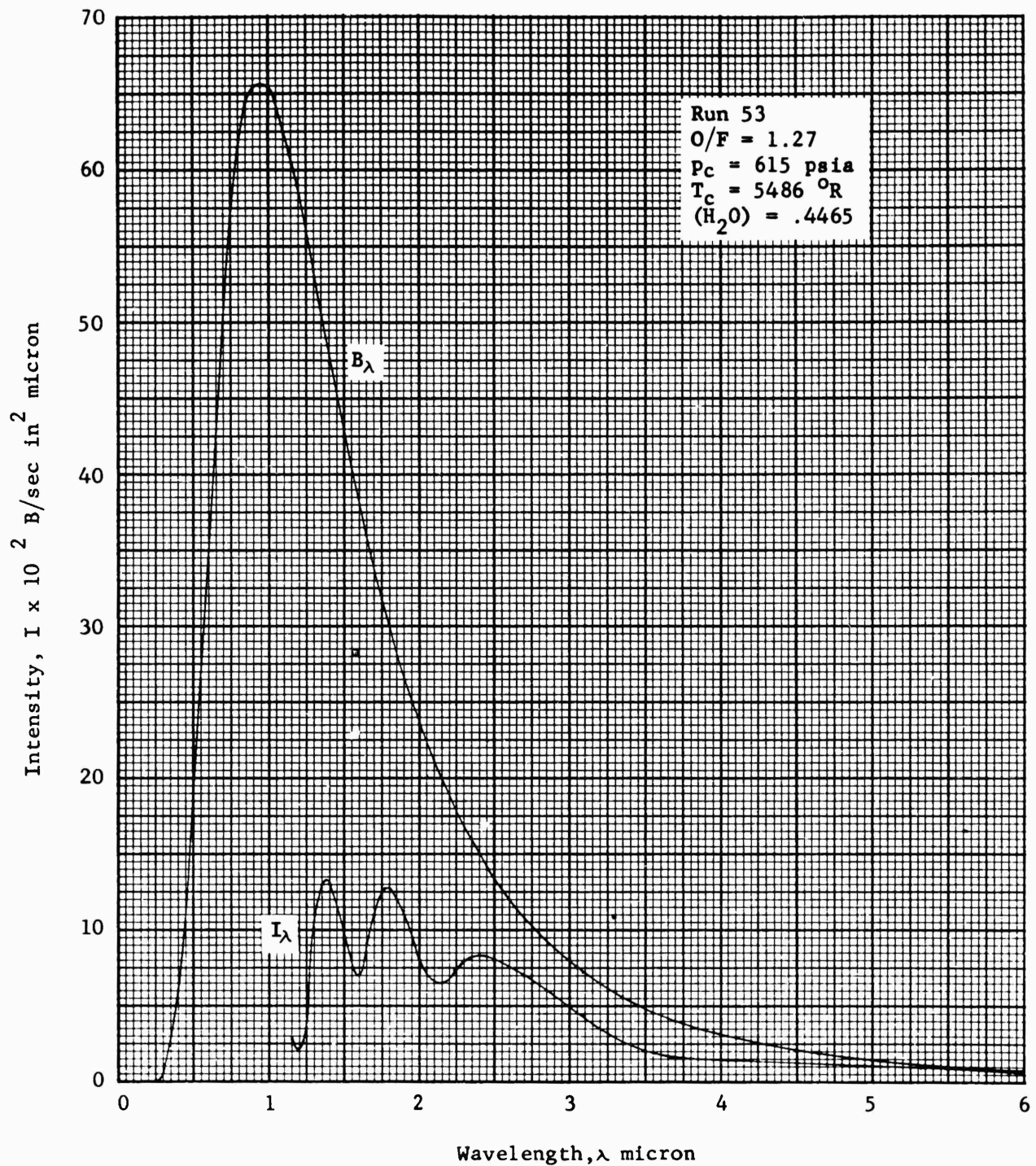


Fig. 4. Spectral Intensity for Combustion Products  
of Nitrogen Tetroxide and Hydrazine, Run 53.  
 $N_2O_4 + (N_2H_4 + 1.7\% H_2O) + 1\% N_2 \rightarrow \text{Products}$

shown in Fig. 2. The hydrazine combination does not exhibit the sharp peak at  $2.25\mu$  that appeared in the spectral curve for the nitrogen tetroxide and ammonia products. Spectral measurements were made for a second hydrazine test (Run 54) using the Na Cl monochrometer and a smaller slit width. The spectral trace had much the same general characteristics as Run 53, except that the intensities were higher in the  $2\mu$  to  $3\mu$  region. However, the accuracy of the spectral distribution is questionable for this run. An unusually high amount of random noise was present in the trace for Run 54, and the wavelength calibration appeared to be incorrect.

The wavelengths at which the maximum and minimum points occur for each of the spectral traces discussed above are listed in Table 2.

Table 2

Wavelengths of Maximum and Minimum Intensities (Microns)

Run No.	Maximum Intensity				Maximum Emissivity					Minimum Intensity			
43	1.41	1.85	2.4	4.6	1.38	1.86	2.91	5.3		1.21	1.62	2.16	4.24
45	1.35	1.83	2.4	4.6	1.38	1.82	2.90	5.0		1.21	1.59	2.14	3.95
46	1.33	1.74	2.3	4.3	1.39	1.74	2.76	----		1.15	1.55	2.06	4.25
48	1.35	1.76	2.24	4.4	1.35	1.80	2.7	5.0		1.20	1.55	2.06	3.97
50	1.35	1.70	2.25	4.4	1.35	1.71	2.76	5.0		1.19	1.55	2.06	4.25
53	1.38	1.78	2.4	---	1.39	1.86	2.83	5.4		1.19	1.59	2.15	----

The data indicate a maximum intensity near  $4.5\mu$  for each run and, except for Run 43, show a shift of the peak intensity for the  $2.7\mu$  band to lower wavelengths. On the other hand, the maximum emissivity for this band occurs much closer to the reported value of  $2.7\mu$ .

Total Emissivity. Two methods were used for obtaining the total emissivity of the gas. One method makes use of the electrical output of the thermopile to obtain a direct measurement of the total intensity of the gas. In the other method, the emissivity was obtained by numerical integration of the spectral intensity over all wavelengths. The total emissivities obtained by each of these methods are displayed in Fig. 5 as a function of temperature. It will be seen that the total emissivity given by the thermopile (solid points) are consistently higher, in fact 20 to 30 per cent higher than the integrated values (circles) obtained from the spectral data. Yet, both sets of data show substantially the same decreasing trend with temperature. The reason for the difference between the measurements is not completely clear. There are several possible causes, but unfortunately there was not sufficient time to conduct the experiments needed to definitely resolve this question.

If we suppose that the spectrometer data are too low, the most obvious conclusion is that the window may have clouded during the run. This must be ruled out because calibration of the instrument before and after the run showed no consistent difference in transmission properties. However, there are three other possible causes that cannot be ruled out. First, there is the possibility that the wavelength scale for the spectrometer was calibrated incorrectly or through use became misaligned with respect to the prism. This seems unlikely though because two of the observed band centers appear in the spectrum at wavelengths that agree reasonably well with the reported locations. Secondly, appreciable radiation may have occurred at wavelengths smaller than the lower spectrometer limit of  $1.14\mu$ . Since all gas radiation below this value was ignored, the integrated emissivity would be too low if significant emission occurred in this region.

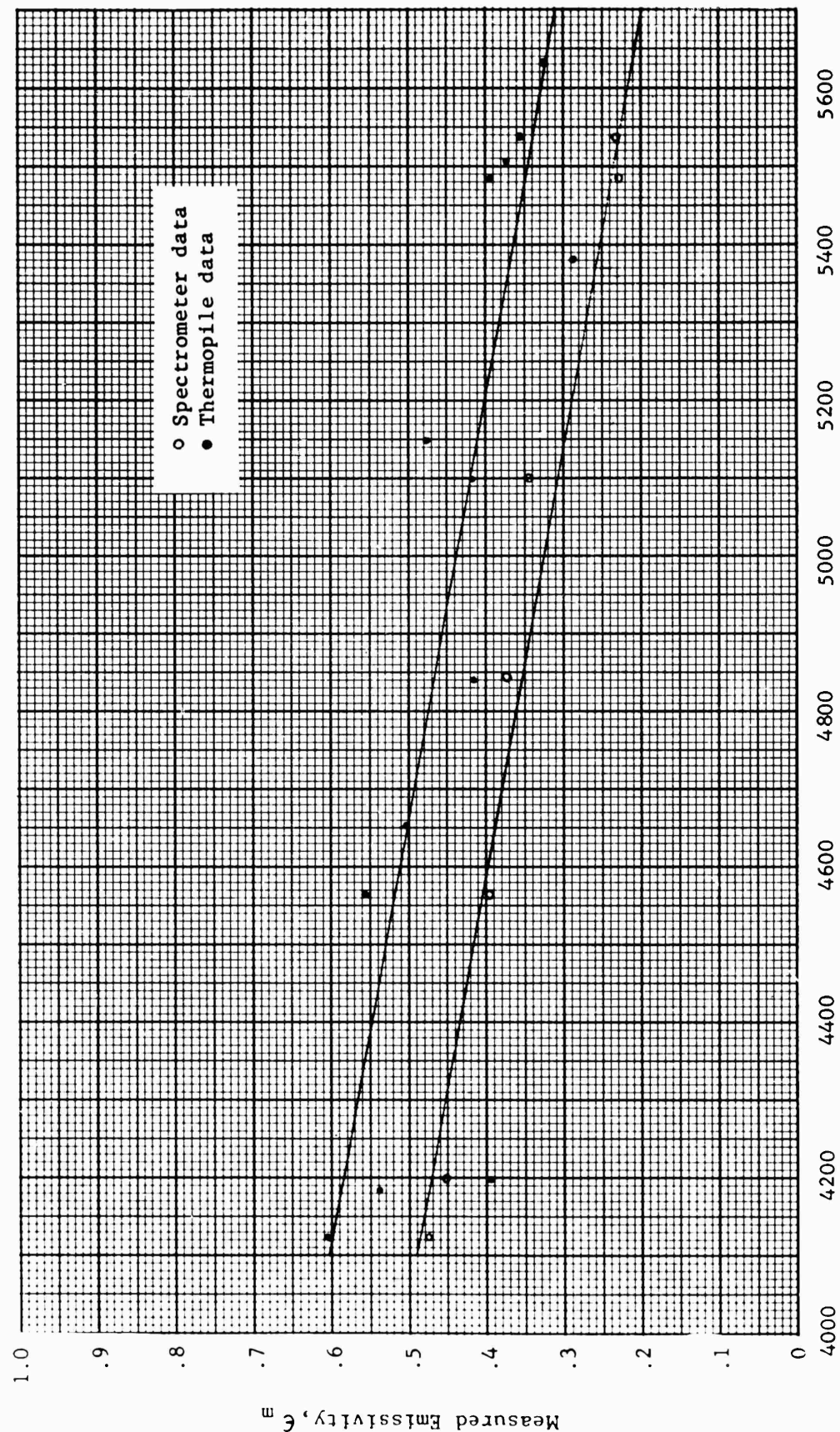


Fig. 5. Measured Emissivities

The band at  $1.1\mu$  is known to exist, of course, and reference (7) shows only a weak band at approximately  $0.94\mu$ . The contribution of these bands are considered to be relatively small, however, and could not account for differences as large as those that were observed. Moreover, it is unlikely that a significant amount of radiation was emitted in the visible region. Although the  $\text{HNO}_3$  exhaust flame showed a slight amount of incandescences, the  $\text{N}_2\text{O}_4$  exhaust flames were almost transparent to the naked eye.

The third and most probable cause of the error, if the spectrometer data are actually too small, may be due to a change of the location of the observation aperture relative to the spectrometer during the test run. A small movement of the aperture could have resulted from unaccounted-for thrust forces, unsymmetrical thermal expansion, and pressurizing stresses. However, every precaution was taken in the design of the apparatus and in the calibration procedures to either compensate for or minimize these effects, and it seems unlikely that consistent emissivity differences as large as those observed could have been derived from these causes alone.

The fact that the error is so consistent leads one to believe that the thermopile data might be incorrect rather than the spectrometer data. The only way that the thermopile values could be too high is if the thermopile system (the curved sapphire rod and the hot junction) happens to be insensitive to radiation at wavelengths where the gas does not emit. The thermopile compares only the energy that is actually absorbed by the receiver. The emissivity calculations assume that the response of the thermopile depends only on the total energy received regardless of where the energy appears in the spectrum. On this basis, the thermopile would give the same reading for the irregular gas emission as it would for black emission of equal total intensity. This would not be true,

of course, if the transmission and absorption characteristics of the thermopile system were irregular. There is some evidence, meager though it is, that this might be the case. A comparison of the two sets of data show that the discrepancy can be accounted for without any change of trend by assuming that the curved sapphire rod transmits no energy at wavelengths smaller than  $1.14\mu$ , or if it does that the thermopile is insensitive in this region. Whether or not this is true is difficult to prove without an extensive evaluation of the monochromatic behavior of the thermopile system. Neither the absorption properties of the thermopile element nor the spectral transmissivity of the curved sapphire rod is known. According to reference (5), the transmissivity of sapphire is not truly flat but approaches a maximum at about  $3\mu$ . The variation is not large though. The transmissivity diminishes no more than 8 per cent from  $3\mu$  to  $0.4\mu$ . This decrease takes place rather abruptly between  $1\mu$  and  $2\mu$ , however. The transmissivity drops off rapidly below  $0.4\mu$  and above  $4\mu$ . However, these data apply only to plane parallel plates that are less than 0.26 cm thick. The range of the transmission tends to decrease with the thickness. Since the sapphire rod was approximately 25 times as thick, a sizable decrease in transmissivity can be expected near both the high and low cut off point even if there were no losses due to the bend in the rod. Actually, it is doubtful that published transmissivity apply accurately to the curved rod since sapphire is anisotropic and the bending undoubtedly effects its transmission and refraction properties. In order to resolve this question, rough experiments were conducted to determine the relatively transmissivity of the curved rod. The results obtained were inconclusive, however.

If we assume that the thermopile did not detect any energy at wavelengths

smaller than  $1.14\mu$  and adjust all the total emissivities to an optical density of 10 ft atm, we obtain the corrected values  $\epsilon_{cs}$  and  $\epsilon_{ct}$  listed in Table 1. The variation of emissivity with optical density was obtained from a cross plot of Hottel's chart for water vapor. The correction accounts for the energy reflected from the back wall of chamber, and for the fraction of energy  $(1-B_{vb})$  cut off by the sapphire at high wavelengths as well as the fraction  $B_{va}$  of black energy that lies below  $1.14\mu$ . The upper cut off point for sapphire was taken to be  $5.5\mu$ . It will be seen in Table 1 that up to 40% of the energy in the black spectrum lies below  $1.14\mu$ , while less than 5% of the energy lies above  $5.5\mu$ . The term  $\bar{\epsilon}$  represents an average value of the gas emissivity for that range  $5.5\mu$  to  $10\mu$ , and  $(1-B_{vc})$  is the fraction of energy that lies above  $10\mu$ .

The corrected values of the emissivity are plotted against the calculated combustion temperature in Fig. 6. The curve  $\epsilon'$  shown in the figure is an extrapolation of the data presented by Hottel<sup>(4)</sup> for pure water vapor at 1 atm pressure and  $p_L = 10$  ft atm. Multiples of  $\epsilon'$ , representing correction factors for total pressure, are also shown for comparison purposes.

Despite the scatter, the data show a definite correlation with temperature. The emissivity decreases as the temperature increases, as one would expect, but the slope of the correlation curve is considerably steeper than the curves shown for pure water vapor. The corrected emissivities decrease from more than twice the ideal value,  $\epsilon'$  at  $4000^{\circ}\text{R}$  to about  $1.5\epsilon'$  at  $5600^{\circ}\text{R}$ . If the indicated trend is true, the value of the pressure correction factor must depend on the temperature as well as on the total pressure.

The dashed curve presented in Fig. 6 is a "best" fit of the measured thermopile data, adjusted to an optical density of 10 ft atm. If the emissivities derived from the thermopile were taken to be the correct values, we must presume

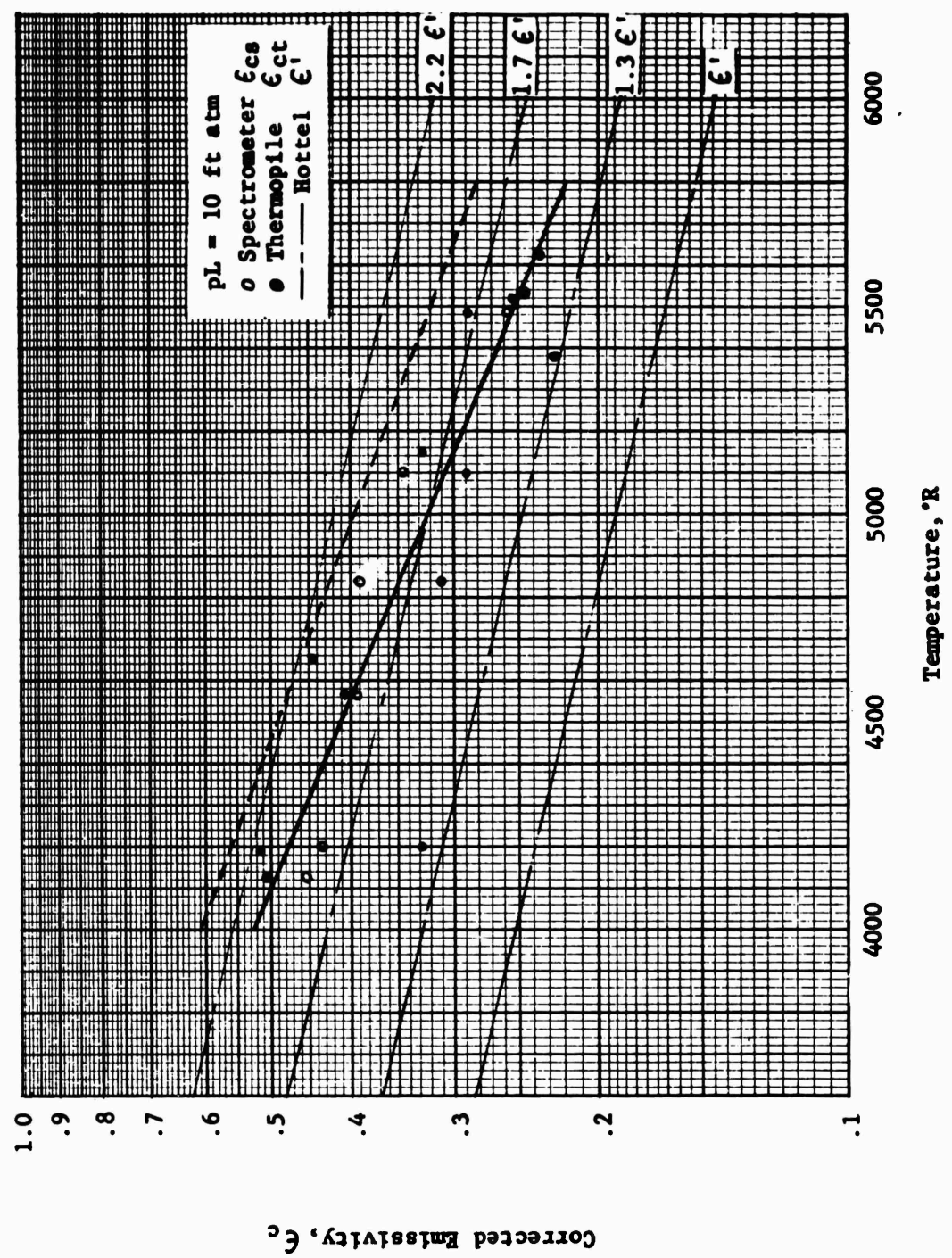


Fig. 6. Corrected Emissivity

that the emissivity of the gas is 16% to 27% higher than that shown for the corrected data. However, as we have already pointed out, there is no conclusive reason for giving preference to either set of data. Thus, we are forced to accept an uncertainty of up to 30% in correlating the emissivity data.

The correlation curve shown in Fig. 6 is given as a function of the combustion temperature by the empirical equation

$$\epsilon = a_1 e^{-b_1 T_c} \quad (1)$$

where  $a_1 = 3.663$  and  $b_1 = 4.857 \times 10^{-4}$ .

Pressure Correction Factor. There is considerable evidence (see Ref. 1) that the radiation from polar molecules such as  $H_2O$  is strongly dependent on the total pressure. Hence, it is not surprising that the measured emissivities for  $p_c = 700$  psia are considerably higher than those predicted for low pressures. However, there are some indications in the literature (See Ref. 7) that the radiation from  $H_2O$  is sensitive to the presence of certain inert molecules, for example  $N_2$ , as well as to the total pressure. The combustion products studied in the present experiments contained as much as 35% to 53%  $N_2$  and up to 13%  $H_2$  in addition to the  $H_2O$ . Small concentrations of the dissociation species, principally  $OH$ , were also present. It was impossible to control these variables, and the ranges of pressures and concentrations were not broad enough to permit isolating the independent effects of the concentration. There is some doubt, therefore, that the increase in intensity is due strictly to the increase in pressure.

On the other hand, if we presume that the total pressure exerts the dominant effect, it is interesting to compare the observed correction factors with the pressure correction data given by Hottel. The correction factors for an optical density of 10 ft-atm are plotted in Fig. 7 against the pressure term  $(p + p_c)/2$ .

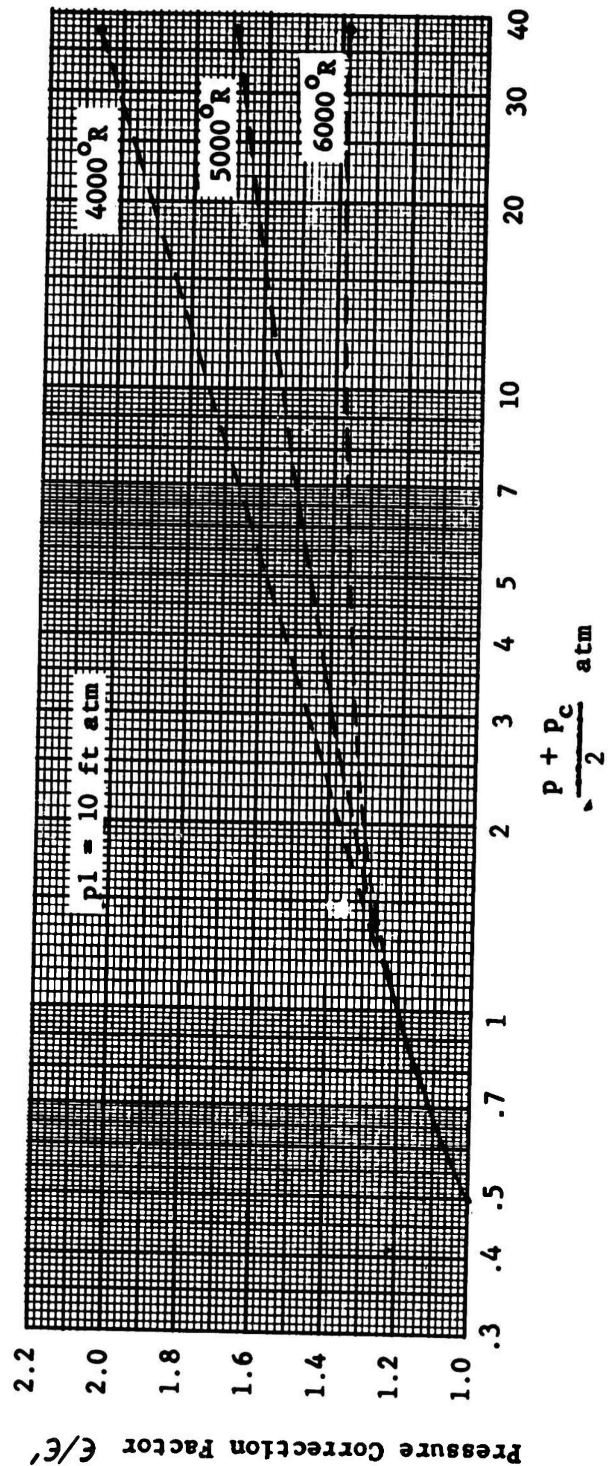


Fig. 7 Extrapolation of Pressure Correction Factor

The symbols  $p$  and  $p_c$  denote respectively the partial pressure of the water vapor and the combustion pressure. The correction factor required to determine the correlated emissivities from the 1 atm curve designated in Fig. 6 by  $\epsilon'$  are plotted at  $(p + p_c)/2 = 38$  atm for three different temperatures. The correction factor predicted by Hottel<sup>(4)</sup> for  $pL = 10$  ft atm is shown as the solid portion of the curves. The points at 38 atm have been joined to Hottel's curve by smooth curve as a matter of interest. It should be emphasized that there is no rigorous foundation for making these extrapolations. The curves are presented merely to illustrate the magnitude of the correction necessary to obtain agreement with the observed data.

Absorption Coefficient. It is shown in Eq. (2.71) that an effective absorption coefficient  $\bar{\mu}$  can be defined in terms of the gas emissivity according to the expression

$$\epsilon = 1 - e^{-\bar{\mu}d_e} \quad (2)$$

where  $e$  is the base for the natural logarithm, and  $d_e$  is the effective beam length for the experimental combustion chamber. If  $\bar{\mu}$  is known and is independent of  $d_e$ , Eq. (2) provides a convenient way for applying the observed emissivities to combustion chambers of different sizes. The values of  $\bar{\mu}$  for the propellant products considered in this report can be derived readily by eliminating  $\epsilon$  from Eqs. (1) and (2) and solving for  $\mu$ . The result is

$$\bar{\mu} = -\frac{1}{d_e} \ln(1 - a_1 e^{-b_1 T_c}) \quad (3)$$

The values of  $\bar{\mu}$  for  $d_e = 4.29$  in. are plotted in Fig. 8 as a function of the calculated combustion temperature. It must be recognized that Fig. 8 applies

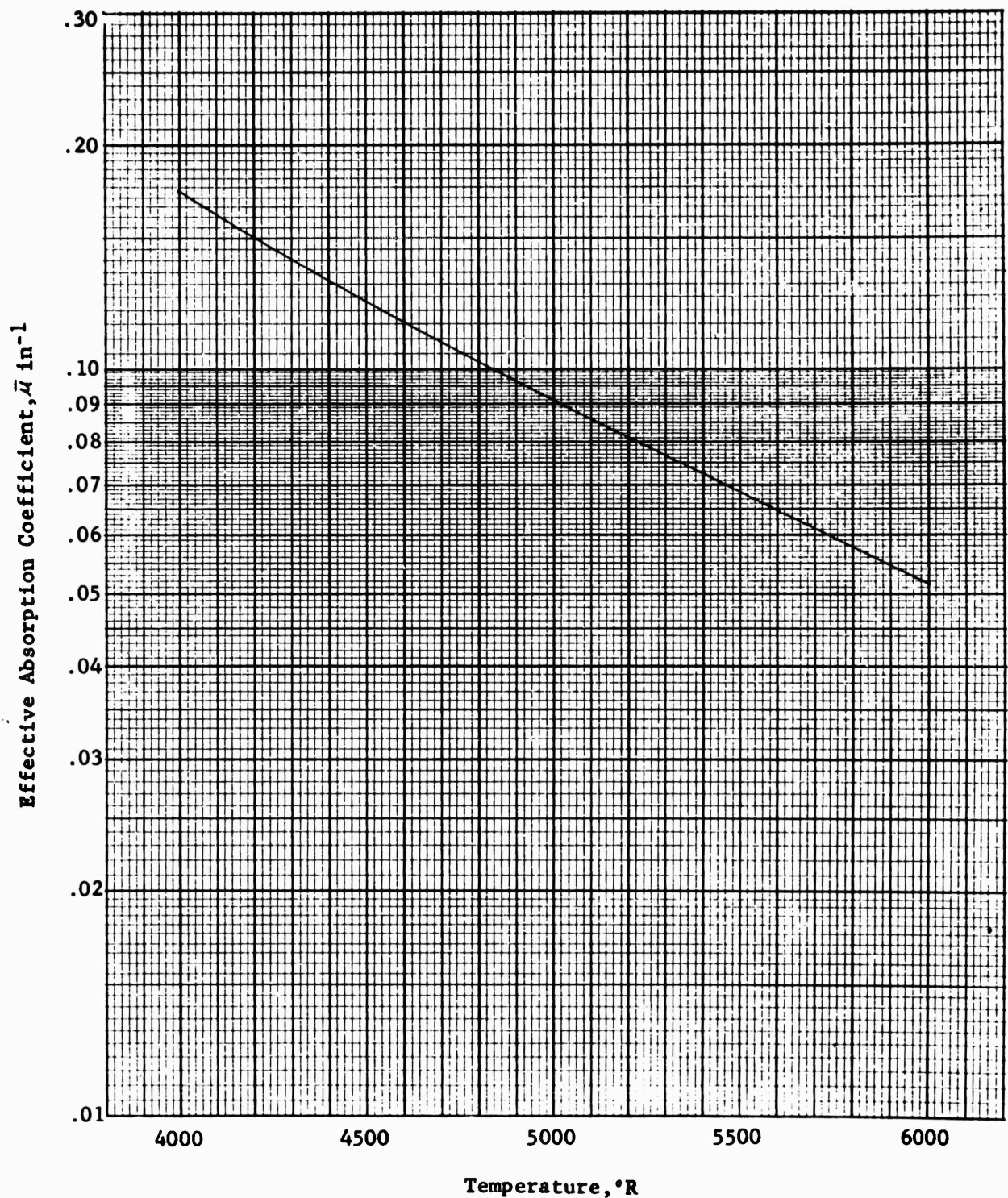


Fig. 8. Effective Absorption Coefficient

only for pressures near 700 psia and holds only to degree of certainty of the emissivity correlation defined by Eq. (1).

The spectral absorption coefficient is frequently useful in theoretical work for comparative studies of band emissivities and effective band widths. The relationship between the spectral absorption coefficient  $\mu_\lambda$  and the measured spectral "emissivity"  $\epsilon_{m\lambda}$  is given approximately by Eq. (2.71). This equation can be solved explicitly for  $\mu_\lambda$  by first carrying out the indicated multiplication and then applying the quadratic formula to the resulting experimental variables. The result is

$$\mu_\lambda = \frac{1}{d_e} \ln \frac{2f_\lambda}{\sqrt{(1-f_\lambda)^2 + 4(1-C\epsilon_{m\lambda})}} - (1-f_\lambda) \quad (4)$$

where  $f_\lambda$  denotes the monochromatic reflectivity of the copper background surface used in the experimental chamber. A factor C has been introduced into the solution to account for the fact that the laboratory blackbody does not provide perfectly black radiation. A value of .998 was taken for C in accordance with data presented in Ref. 10 for cylindrical cavities.

The spectral absorption coefficients derived from the measured spectrometer data are presented in Table 3 for wavelengths ranging from 1.14 to of the order of 10. At each wavelength, the table also shows the values of the measured emissivity ( $\epsilon_{m\lambda}$ ), the measured reflectivity of the background plate ( $f_\lambda$ ), the true observed emissivity ( $\epsilon_\lambda$ ), and the absolute spectral intensity ( $I_\lambda$ ) of the combustion products. The absorptivities were calculated from Eq. 4 taking  $d_e = 4.29$  in. and  $C = .998$  and the values of  $f_\lambda$  listed in the table. The emissivity  $\epsilon_\lambda$  is calculated from Eq. (2.66), using  $d = d_e = 4.29$  in. The effective diameter was

considered to be a closer approximation of the depth of the observed radiating column than the true diameter (4.42 in.). This assumption in effect allows for a non-emitting boundary zone of 0.12 in. The values of  $I_\lambda$  shown in Table 3 are the values plotted in Figs. 2, 3, and 4.

Table 3. Measured ultraviolet properties  
RUN NO. 43 [H<sub>2</sub>O] 0.65% T<sub>c</sub> = 10°C T<sub>0</sub> = 5.803-01

$\lambda$ micron	$\epsilon_{\text{in}\lambda}$	$I_{\lambda}$	$\mu_{\lambda}$	$\epsilon_{\lambda}$	$I_{\lambda}$
1.140+00	6.516-02	3.170-02	1.521-02	6.315-02	1.659-02
1.163+00	5.867-02	3.249-02	1.363-02	5.681-02	1.491-02
1.186+00	5.309-02	3.328-02	1.229-02	5.136-02	1.345-02
1.209+00	4.492-02	3.405-02	1.035-02	4.342-02	1.132-02
1.231+00	5.040-02	3.481-02	1.164-02	4.869-02	1.262-02
1.256+00	1.045-01	3.563-02	2.484-02	1.011-01	2.600-02
1.286+00	2.300-01	3.661-02	5.889-02	2.232-01	5.677-02
1.316+00	3.871-01	3.757-02	1.105-01	3.775-01	9.472-02
1.346+00	4.661-01	3.852-02	1.417-01	4.556-01	1.126-01
1.376+00	5.027-01	3.945-02	1.578-01	4.919-01	1.195-01
1.414+00	4.802-01	4.059-02	1.476-01	4.692-01	1.114-01
1.458+00	4.398-01	4.189-02	1.305-01	4.287-01	9.881-02
1.501+00	3.791-01	4.316-02	1.071-01	3.683-01	8.223-02
1.545+00	2.806-01	4.439-02	7.377-02	2.713-01	5.855-02
1.588+00	2.337-01	4.560-02	5.949-02	2.252-01	4.691-02
1.616+00	2.318-01	4.634-02	5.890-02	2.233-01	4.544-02
1.646+00	2.554-01	4.714-02	6.586-02	2.461-01	4.882-02
1.675+00	3.208-01	4.792-02	8.645-02	3.099-01	5.987-02
1.705+00	4.016-01	4.868-02	1.149-01	3.892-01	7.321-02
1.735+00	5.167-01	4.943-02	1.631-01	5.033-01	9.212-02
1.765+00	5.959-01	5.017-02	2.036-01	5.825-01	1.037-01
1.795+00	6.585-01	5.089-02	2.418-01	6.455-01	1.118-01
1.824+00	7.061-01	5.160-02	2.758-01	6.937-01	1.167-01
1.854+00	7.071-01	5.230-02	2.764-01	6.946-01	1.136-01
1.888+00	6.956-01	5.307-02	2.676-01	6.827-01	1.081-01
1.930+00	6.758-01	5.401-02	2.531-01	6.624-01	1.006-01
1.972+00	6.367-01	5.493-02	2.271-01	6.225-01	9.070-02
2.014+00	5.816-01	5.582-02	1.950-01	5.667-01	7.918-02
2.057+00	5.008-01	5.669-02	1.550-01	4.856-01	6.505-02
2.099+00	4.464-01	5.753-02	1.316-01	4.314-01	5.540-02
2.141+00	4.287-01	5.834-02	1.245-01	4.137-01	5.092-02
2.183+00	4.388-01	5.913-02	1.284-01	4.235-01	4.996-02
2.226+00	4.905-01	5.989-02	1.500-01	4.746-01	5.366-02
2.268+00	5.544-01	6.063-02	1.801-01	5.382-01	5.833-02
2.337+00	6.464-01	6.178-02	2.322-01	6.307-01	6.378-02
2.408+00	7.062-01	6.289-02	2.741-01	6.914-01	6.516-02
2.478+00	7.787-01	6.393-02	3.382-01	7.657-01	6.728-02
2.549+00	8.228-01	6.490-02	3.886-01	8.112-01	6.649-02
2.619+00	8.648-01	6.581-02	4.500-01	8.549-01	6.539-02
2.690+00	8.705-01	6.666-02	4.596-01	8.608-01	6.148-02
2.761+00	8.951-01	6.744-02	5.072-01	8.865-01	5.916-02
2.831+00	9.223-01	6.816-02	5.750-01	9.151-01	5.710-02
2.902+00	9.234-01	6.882-02	5.780-01	9.162-01	5.348-02
2.988+00	8.995-01	6.954-02	5.165-01	8.909-01	4.800-02
3.084+00	8.519-01	7.025-02	4.283-01	8.407-01	4.145-02
3.181+00	7.796-01	7.085-02	3.379-01	7.653-01	3.457-02
3.277+00	7.180-01	7.134-02	2.819-01	7.017-01	2.909-02
3.374+00	6.492-01	7.174-02	2.325-01	6.312-01	2.404-02
3.470+00	5.621-01	7.203-02	1.826-01	5.431-01	1.904-02
3.567+00	5.205-01	7.223-02	1.622-01	5.014-01	1.619-02

\*The characteristics +01, -00, -01, etc., represent respectively  $(10^1)$ ,  $(10^0)$ ,  $(10^{-1})$ , etc.

Table 3. (Continued)  
 RUN NO. 43 [H<sub>2</sub>O] 0.6536 T<sub>C</sub> 1000 803-01

$\lambda$ micron	$\epsilon_{m\lambda}$	$f_\lambda$	$\mu_\lambda$	$\epsilon_\lambda$	$I_\lambda$
3.664+00	4.843-01	7.233-02	1.459-01	4.653-01	1.386-02
3.760+00	4.724-01	7.234-02	1.409-01	4.535-01	1.248-02
3.857+00	4.652-01	7.227-02	1.378-01	4.464-01	1.136-02
3.953+00	4.849-01	7.210-02	1.362-01	4.660-01	1.099-02
4.243+00	5.979-01	7.113-02	2.019-01	5.793-01	1.093-02
4.532+00	7.406-01	6.948-02	3.012-01	7.253-01	1.107-02
4.809+00	8.944-01	6.733-02	5.057-01	8.858-01	1.113-02
5.059+00	9.369-01	6.497-02	6.227-01	9.308-01	9.889-03
5.309+00	9.388-01	6.226-02	6.300-01	9.330-01	8.431-03
5.559+00	8.211-01	5.925-02	3.875-01	8.103-01	6.266-03
5.809+00	8.500-01	5.597-02	4.283-01	8.408-01	5.594-03
6.058+00	8.342-01	5.248-02	4.062-01	8.249-01	4.747-03
6.307+00	8.577-01	4.885-02	4.419-01	8.498-01	4.253-03
6.524+00	8.106-01	4.558-02	3.772-01	8.018-01	3.566-03
6.740+00	8.045-01	4.226-02	3.706-01	7.960-01	3.158-03
7.317+00	6.850-01	3.334-02	2.630-01	6.763-01	2.006-03
7.845+00	8.673-01	2.546-02	4.627-01	8.626-01	1.993-03
8.298+00	9.530-01	1.929-02	6.991-01	9.502-01	1.793-03
8.748+00	8.388-01	1.397-02	4.203-01	8.352-01	1.301-03
9.150+00	8.016-01	1.011-02	3.733-01	7.984-01	1.056-03
9.552+00	7.978-01	7.313-03	3.694-01	7.950-01	8.980-04
9.940+00	9.999-01	5.793-03	1.436+00	9.979-01	9.732-04
1.032+01	3.377-01	2.786-02	9.363-02	3.308-01	2.806-04
1.069+01	4.041-01	2.920-02	1.176-01	3.963-01	2.952-04
1.103+01	4.588-01	3.041-02	1.395-01	4.503-01	2.986-04
1.137+01	6.037-01	3.161-02	2.106-01	5.948-01	3.522-04
1.170+01	7.755-01	3.273-02	3.407-01	7.682-01	4.095-04

Table 3. (Continued)  
 RUN NO. 45 [H<sub>2</sub>O] 0.5875 T<sub>c</sub> 4123°R t 4.531-01

micron	$\epsilon_{\lambda}$	$f_{\lambda}$	$\epsilon_{\lambda}$	$\epsilon_{\lambda}$	$I_{\lambda}$
1.140+00	6.297-02	3.170-02	1.468-02	6.103-02	9.401-03
1.163+00	5.267-02	3.250-02	1.220-02	5.099-02	7.929-03
1.186+00	4.374-02	3.329-02	1.008-02	4.230-02	6.626-03
1.209+00	3.909-02	3.406-02	8.976-03	3.777-02	5.948-03
1.220+00	4.463-02	3.443-02	1.027-02	4.312-02	6.802-03
1.231+00	5.707-02	3.480-02	1.322-02	5.514-02	8.712-03
1.243+00	8.548-02	3.519-02	2.011-02	8.264-02	1.307-02
1.256+00	1.271-01	3.562-02	3.059-02	1.230-01	1.946-02
1.271+00	2.119-01	3.611-02	5.365-02	2.056-01	3.253-02
1.286+00	2.962-01	3.660-02	7.921-02	2.881-01	4.556-02
1.301+00	3.601-01	3.708-02	1.008-01	3.509-01	5.543-02
1.316+00	4.623-01	3.756-02	1.402-01	4.521-01	7.127-02
1.331+00	4.845-01	3.803-02	1.498-01	4.740-01	7.455-02
1.346+00	5.274-01	3.850-02	1.695-01	5.167-01	8.102-02
1.361+00	5.215-01	3.897-02	1.666-01	5.107-01	7.980-02
1.376+00	5.246-01	3.943-02	1.680-01	5.137-01	7.994-02
1.392+00	5.145-01	3.992-02	1.632-01	5.035-01	7.798-02
1.414+00	5.121-01	4.059-02	1.620-01	5.009-01	7.702-02
1.458+00	4.612-01	4.190-02	1.393-01	4.499-01	6.799-02
1.479+00	4.186-01	4.252-02	1.220-01	4.075-01	6.097-02
1.501+00	3.601-01	4.315-02	1.003-01	3.496-01	5.176-02
1.523+00	3.088-01	4.378-02	8.281-02	2.990-01	4.377-02
1.545+00	2.654-01	4.440-02	6.906-02	2.564-01	3.709-02
1.567+00	2.344-01	4.501-02	5.973-02	2.261-01	3.230-02
1.588+00	2.253-01	4.559-02	5.705-02	2.171-01	3.062-02
1.616+00	2.328-01	4.635-02	5.920-02	2.243-01	3.109-02
1.646+00	3.087-01	4.715-02	8.255-02	2.982-01	4.054-02
1.675+00	3.822-01	4.790-02	1.078-01	3.703-01	4.933-02
1.705+00	4.624-01	4.868-02	1.391-01	4.494-01	5.863-02
1.735+00	5.569-01	4.943-02	1.828-01	5.435-01	6.938-02
1.764+00	6.481-01	5.015-02	2.350-01	6.352-01	7.930-02
1.795+00	6.849-01	5.090-02	2.601-01	6.723-01	8.204-02
1.824+00	7.041-01	5.160-02	2.743-01	6.917-01	8.245-02
1.854+00	7.004-01	5.230-02	2.713-01	6.878-01	8.006-02
1.888+00	6.756-01	5.308-02	2.531-01	6.624-01	7.503-02
1.930+00	6.366-01	5.402-02	2.272-01	6.226-01	6.810-02
1.972+00	5.830-01	5.493-02	1.958-01	5.684-01	5.998-02
2.014+00	5.237-01	5.581-02	1.657-01	5.087-01	5.178-02
2.057+00	4.750-01	5.669-02	1.436-01	4.600-01	4.513-02
2.099+00	4.436-01	5.753-02	1.305-01	4.286-01	4.053-02
2.141+00	4.453-01	5.834-02	1.311-01	4.301-01	3.917-02
2.183+00	4.711-01	5.912-02	1.417-01	4.555-01	3.995-02
2.226+00	5.159-01	5.989-02	1.615-01	4.999-01	4.222-02
2.268+00	6.272-01	6.063-02	2.204-01	6.115-01	4.972-02
2.337+00	6.808-01	6.178-02	2.554-01	6.657-01	5.084-02
2.408+00	7.284-01	6.289-02	2.919-01	7.141-01	5.115-02
2.478+00	7.640-01	6.393-02	3.236-01	7.505-01	5.043-02
2.549+00	8.140-01	6.491-02	3.776-01	8.021-01	5.055-02
2.619+00	8.437-01	6.581-02	4.170-01	8.329-01	4.925-02
2.690+00	8.679-01	6.666-02	4.551-01	8.580-01	4.761-02

Table 3. (Continued)  
 RUN NO. 45 [H20] 0.5875 T<sub>c</sub> 4123 °R E 4.531-01

$\lambda$ micron	$\epsilon_{m\lambda}$	$\epsilon_\lambda$	$\epsilon'_\lambda$	$\epsilon_\lambda$	$I_\lambda$
2.761+00	8.866-01	6.745-02	4.896-01	8.776-01	4.572-02
2.831+00	8.996-01	6.816-02	5.171-01	8.912-01	4.360-02
2.902+00	9.121-01	6.882-02	5.470-01	9.043-01	4.156-02
2.988+00	8.941-01	6.955-02	5.047-01	8.852-01	3.773-02
3.084+00	8.400-01	7.025-02	4.108-01	8.283-01	3.247-02
3.181+00	7.638-01	7.085-02	3.222-01	7.490-01	2.703-02
3.277+00	6.809-01	7.134-02	2.540-01	6.636-01	2.207-02
3.374+00	6.219-01	7.174-02	2.156-01	6.035-01	1.852-02
3.470+00	5.561-01	7.203-02	1.795-01	5.371-01	1.522-02
3.567+00	4.872-01	7.223-02	1.472-01	4.682-01	1.227-02
3.663+00	4.711-01	7.233-02	1.403-01	4.522-01	1.097-02
3.760+00	4.586-01	7.234-02	1.351-01	4.399-01	9.889-03
3.856+00	4.725-01	7.227-02	1.409-01	4.536-01	9.462-03
3.953+00	5.033-01	7.210-02	1.544-01	4.843-01	9.382-03
4.049+00	5.497-01	7.186-02	1.763-01	5.307-01	9.560-03
4.243+00	6.496-01	7.113-02	2.329-01	6.318-01	9.869-03
4.436+00	7.473-01	7.010-02	3.070-01	7.321-01	9.960-03
4.629+00	8.531-01	6.879-02	4.305-01	8.423-01	1.002-02
4.809+00	9.398-01	6.733-02	6.327-01	9.338-01	9.831-03
4.976+00	9.998-01	6.580-02	1.411+00	9.976-01	9.412-03
5.142+00	9.272-01	6.411-02	5.907-01	9.207-01	7.803-03
5.309+00	9.487-01	6.226-02	6.697-01	9.435-01	7.202-03
5.475+00	9.307-01	6.029-02	6.027-01	9.246-01	6.373-03
5.642+00	8.120-01	5.818-02	3.765-01	8.011-01	4.997-03
5.809+00	9.125-01	5.597-02	5.509-01	9.059-01	5.125-03
5.975+00	9.417-01	5.367-02	6.431-01	9.366-01	4.817-03
6.142+00	9.685-01	5.128-02	7.803-01	9.648-01	4.520-03
6.307+00	8.890-01	4.885-02	4.984-01	8.821-01	3.774-03
6.451+00	8.081-01	4.669-02	3.740-01	7.990-01	3.163-03
7.028+00	8.825-01	3.779-02	4.878-01	8.766-01	2.580-03
7.605+00	8.662-01	2.898-02	4.600-01	8.610-01	1.921-03
8.068+00	9.999-01	2.234-02	1.432+00	9.979-01	1.806-03
8.517+00	9.481-01	1.658-02	6.776-01	9.453-01	1.410-03
8.943+00	9.999-01	1.197-02	1.435+00	9.979-01	1.249-03
9.348+00	9.999-01	8.588-03	1.435+00	9.979-01	1.064-03
9.748+00	9.999-01	6.389-03	1.436+00	9.979-01	9.134-04
1.013+01	9.999-01	5.527-03	1.436+00	9.979-01	7.950-04
1.050+01	9.999-01	6.005-03	1.436+00	9.979-01	6.952-04
1.085+01	9.999-01	7.782-03	1.435+00	9.979-01	6.161-04

Table 3. (Continued)  
 RUN NO. 46 [H<sub>2</sub>O] 0.6105 T<sub>c</sub> 4198 °R ε 4.349-01

$\lambda$ micron	$E_{m\lambda}$	$F_{\lambda}$	$\mu_{\lambda}$	$E_{\lambda}$	$I_{\lambda}$
1.140+00	4.483-02	3.170-02	1.035-02	4.342-02	7.376-03
1.151+00	3.823-02	3.209-02	8.791-03	3.701-02	6.313-03
1.163+00	3.936-02	3.250-02	9.052-03	3.809-02	6.520-03
1.174+00	4.373-02	3.288-02	1.008-02	4.231-02	7.264-03
1.186+00	4.698-02	3.329-02	1.084-02	4.544-02	7.821-03
1.197+00	5.458-02	3.366-02	1.264-02	5.279-02	9.103-03
1.209+00	7.982-02	3.406-02	1.874-02	7.723-02	1.334-02
1.220+00	1.369-01	3.443-02	3.318-02	1.327-01	2.294-02
1.232+00	1.906-01	3.483-02	4.768-02	1.850-01	3.200-02
1.243+00	2.142-01	3.519-02	5.435-02	2.080-01	3.598-02
1.257+00	2.651-01	3.565-02	6.948-02	2.577-01	4.458-02
1.272+00	3.253-01	3.614-02	8.881-02	3.168-01	5.475-02
1.287+00	3.376-01	3.663-02	9.295-02	3.288-01	5.673-02
1.302+00	3.512-01	3.711-02	9.762-02	3.421-01	5.889-02
1.317+00	3.701-01	3.759-02	1.043-01	3.607-01	6.191-02
1.332+00	4.211-01	3.806-02	1.234-01	4.110-01	7.031-02
1.347+00	3.907-01	3.853-02	1.117-01	3.808-01	6.489-02
1.362+00	3.839-01	3.900-02	1.092-01	3.740-01	6.344-02
1.377+00	3.764-01	3.946-02	1.064-01	3.665-01	6.186-02
1.393+00	3.921-01	3.995-02	1.121-01	3.819-01	6.409-02
1.415+00	3.731-01	4.062-02	1.051-01	3.630-01	6.040-02
1.437+00	3.176-01	4.128-02	8.588-02	3.082-01	5.080-02
1.459+00	2.687-01	4.193-02	7.022-02	2.601-01	4.244-02
1.480+00	2.234-01	4.254-02	5.665-02	2.158-01	3.482-02
1.502+00	2.088-01	4.318-02	5.243-02	2.014-01	3.213-02
1.524+00	2.063-01	4.381-02	5.170-02	1.989-01	3.134-02
1.546+00	2.088-01	4.443-02	5.238-02	2.012-01	3.130-02
1.568+00	2.422-01	4.504-02	6.203-02	2.337-01	3.586-02
1.590+00	3.190-01	4.564-02	8.603-02	3.086-01	4.671-02
1.617+00	4.230-01	4.637-02	1.234-01	4.109-01	6.105-02
1.647+00	5.118-01	4.717-02	1.611-01	4.990-01	7.261-02
1.677+00	5.717-01	4.796-02	1.907-01	5.587-01	7.958-02
1.707+00	5.800-01	4.873-02	1.950-01	5.669-01	7.898-02
1.736+00	6.542-01	4.946-02	2.391-01	6.415-01	8.736-02
1.766+00	6.387-01	5.020-02	2.290-01	6.257-01	8.324-02
1.796+00	6.066-01	5.093-02	2.096-01	5.931-01	7.705-02
1.826+00	5.807-01	5.164-02	1.950-01	5.669-01	7.187-02
1.856+00	5.446-01	5.234-02	1.762-01	5.305-01	6.562-02
1.890+00	4.974-01	5.312-02	1.538-01	4.831-01	5.807-02
1.932+00	4.688-01	5.406-02	1.413-01	4.545-01	5.269-02
1.974+00	4.407-01	5.497-02	1.296-01	4.264-01	4.766-02
2.016+00	4.506-01	5.586-02	1.335-01	4.360-01	4.696-02
2.058+00	4.622-01	5.671-02	1.382-01	4.473-01	4.640-02
2.100+00	5.140-01	5.755-02	1.609-01	4.986-01	4.980-02
2.142+00	5.895-01	5.835-02	1.989-01	5.741-01	5.520-02
2.184+00	6.564-01	5.914-02	2.391-01	6.415-01	5.936-02
2.226+00	7.029-01	5.989-02	2.720-01	6.887-01	6.132-02
2.268+00	7.387-01	6.063-02	3.010-01	7.251-01	6.212-02
2.337+00	7.791-01	6.178-02	3.390-01	7.665-01	6.162-02
2.407+00	8.223-01	6.288-02	3.884-01	8.110-01	6.111-02

Table 3 (Continued)  
 RUN NO. 46 [H<sub>2</sub>O] 0.6105 T<sub>c</sub> 4198°R E 4.349-01

$\lambda$ micron	$\epsilon_{m\lambda}$	$f_\lambda$	$\mu_\lambda$	$\epsilon_\lambda$	$I_\lambda$
2.477+00	8.654-01	6.391-02	4.514-01	8.558-01	6.044-02
2.547+00	8.369-01	6.488-02	4.075-01	8.259-01	5.467-02
2.618+00	9.004-01	6.580-02	5.194-01	8.923-01	5.538-02
2.688+00	8.787-01	6.664-02	4.745-01	8.694-01	5.061-02
2.758+00	9.096-01	6.741-02	5.410-01	9.018-01	4.925-02
2.828+00	8.358-01	6.813-02	4.053-01	8.243-01	4.226-02
2.898+00	7.580-01	6.879-02	3.170-01	7.434-01	3.579-02
2.983+00	6.787-01	6.951-02	2.527-01	6.618-01	2.955-02
3.080+00	7.988-01	7.022-02	3.587-01	7.854-01	3.220-02
3.177+00	5.035-01	7.083-02	1.546-01	4.848-01	1.828-02
3.274+00	4.285-01	7.133-02	1.231-01	4.104-01	1.424-02
3.372+00	4.128-01	7.173-02	1.171-01	3.948-01	1.262-02
3.468+00	4.197-01	7.202-02	1.197-01	4.016-01	1.185-02
3.566+00	3.875-01	7.223-02	1.077-01	3.699-01	1.008-02
3.663+00	3.983-01	7.233-02	1.116-01	3.805-01	9.586-03
3.760+00	3.901-01	7.234-02	1.086-01	3.724-01	8.687-03
3.857+00	4.233-01	7.227-02	1.210-01	4.050-01	8.757-03
3.954+00	4.380-01	7.210-02	1.268-01	4.196-01	8.417-03
4.051+00	4.527-01	7.185-02	1.327-01	4.341-01	8.091-03
4.148+00	4.670-01	7.153-02	1.387-01	4.484-01	7.771-03
4.245+00	4.766-01	7.112-02	1.428-01	4.580-01	7.390-03
4.342+00	9.999-01	7.063-02	1.420+00	9.977-01	1.501-02
4.439+00	9.999-01	7.008-02	1.420+00	9.977-01	1.400-02
4.536+00	9.999-01	6.945-02	1.421+00	9.977-01	1.308-02
4.633+00	9.999-01	6.876-02	1.421+00	9.977-01	1.222-02
4.813+00	9.999-01	6.730-02	1.421+00	9.977-01	1.081-02
4.980+00	9.999-01	6.576-02	1.421+00	9.978-01	9.685-03
5.146+00	9.999-01	6.407-02	1.422+00	9.978-01	8.697-03
5.313+00	9.999-01	6.221-02	1.422+00	9.978-01	7.830-03
5.480+00	9.999-01	6.023-02	1.423+00	9.978-01	7.067-03
5.646+00	9.999-01	5.813-02	1.423+00	9.978-01	6.394-03
5.813+00	9.999-01	5.591-02	1.424+00	9.978-01	5.797-03
5.979+00	9.999-01	5.361-02	1.424+00	9.978-01	5.268-03
6.599+00	9.999-01	4.443-02	1.427+00	9.978-01	3.756-03
7.176+00	9.999-01	3.550-02	1.429+00	9.978-01	2.805-03
7.735+00	9.999-01	2.706-02	1.431+00	9.978-01	2.153-03
8.186+00	9.999-01	2.075-02	1.432+00	9.979-01	1.759-03
8.637+00	9.999-01	1.519-02	1.434+00	9.979-01	1.451-03
1.103+01	9.999-01	9.241-03	1.435+00	9.979-01	0.

Tab. 3 (Continued)  
RUN NO. 48 [H<sub>2</sub>O] 0.5793 T<sub>c</sub> 5100° E 3.433-01

$\lambda$ micron	$\epsilon_{m\lambda}$	$f_\lambda$	$M_\lambda$	$\epsilon_\lambda$	$I_\lambda$
1.140+00	9.380-02	3.170-02	2.224-02	9.099-02	4.056-02
1.151+00	8.827-02	3.209-02	2.086-02	8.558-02	3.796-02
1.162+00	8.297-02	3.247-02	1.954-02	8.040-02	3.547-02
1.173+00	8.071-02	3.284-02	1.898-02	7.818-02	3.430-02
1.184+00	8.057-02	3.322-02	1.893-02	7.802-02	3.402-02
1.196+00	8.066-02	3.362-02	1.895-02	7.808-02	3.383-02
1.207+00	9.348-02	3.400-02	2.211-02	9.050-02	3.895-02
1.218+00	1.140-01	3.436-02	2.727-02	1.104-01	4.719-02
1.229+00	1.486-01	3.473-02	3.625-02	1.440-01	6.113-02
1.240+00	2.112-01	3.510-02	5.349-02	2.051-01	8.639-02
1.254+00	2.673-01	3.556-02	7.016-02	2.599-01	1.085-01
1.269+00	3.289-01	3.605-02	9.003-02	3.204-01	1.323-01
1.285+00	3.519-01	3.657-02	9.790-02	3.430-01	1.400-01
1.300+00	3.926-01	3.705-02	1.126-01	3.831-01	1.545-01
1.315+00	4.197-01	3.753-02	1.229-01	4.098-01	1.633-01
1.331+00	4.394-01	3.803-02	1.305-01	4.310-01	1.692-01
1.346+00	4.595-01	3.850-02	1.390-01	4.491-01	1.744-01
1.362+00	4.544-01	3.900-02	1.368-01	4.439-01	1.702-01
1.377+00	4.493-01	3.946-02	1.346-01	4.387-01	1.659-01
1.393+00	4.410-01	3.995-02	1.312-01	4.303-01	1.604-01
1.415+00	4.331-01	4.062-02	1.279-01	4.223-01	1.543-01
1.437+00	4.237-01	4.128-02	1.241-01	4.128-01	1.478-01
1.459+00	4.074-01	4.193-02	1.177-01	3.966-01	1.390-01
1.481+00	3.590-01	4.257-02	9.992-02	3.486-01	1.196-01
1.503+00	3.136-01	4.321-02	8.442-02	3.038-01	1.020-01
1.525+00	2.839-01	4.384-02	7.483-02	2.746-01	9.017-02
1.547+00	2.754-01	4.445-02	7.214-02	2.662-01	8.546-02
1.569+00	2.848-01	4.507-02	7.504-02	2.752-01	8.640-02
1.591+00	3.398-01	4.567-02	9.302-02	3.290-01	1.009-01
1.619+00	4.159-01	4.643-02	1.206-01	4.039-01	1.202-01
1.649+00	4.894-01	4.722-02	1.509-01	4.766-01	1.374-01
1.679+00	5.563-01	4.801-02	1.827-01	5.433-01	1.517-01
1.709+00	6.068-01	4.878-02	2.100-01	5.938-01	1.604-01
1.739+00	6.381-01	4.953-02	2.288-01	6.252-01	1.635-01
1.769+00	6.576-01	5.027-02	2.413-01	6.448-01	1.631-01
1.799+00	6.680-01	5.100-02	2.482-01	6.551-01	1.603-01
1.828+00	6.587-01	5.169-02	2.418-01	6.456-01	1.528-01
1.858+00	6.287-01	5.239-02	2.225-01	6.150-01	1.408-01
1.894+00	5.805-01	5.321-02	1.947-01	5.663-01	1.246-01
1.936+00	5.202-01	5.415-02	1.642-01	5.056-01	1.061-01
1.978+00	4.762-01	5.506-02	1.443-01	4.616-01	9.241-02
2.020+00	4.566-01	5.594-02	1.359-01	4.419-01	8.439-02
2.062+00	4.523-01	5.679-02	1.341-01	4.374-01	7.970-02
2.104+00	4.882-01	5.763-02	1.493-01	4.729-01	8.220-02
2.146+00	5.360-01	5.843-02	1.713-01	5.203-01	8.631-02
2.188+00	6.032-01	5.921-02	2.065-01	5.876-01	9.303-02
2.230+00	6.841-01	5.997-02	2.581-01	6.695-01	1.012-01
2.273+00	7.002-01	6.071-02	2.698-01	6.857-01	9.878-02
2.344+00	7.231-01	6.189-02	2.877-01	7.089-01	9.456-02
2.414+00	7.434-01	6.298-02	3.048-01	7.295-01	9.018-02

Table 3. (Continued)  
 RUN NO. 48 [H2O] 0.5793 T<sub>c</sub> 5100°R ε 3.433-01

$\lambda_{\text{micron}}$	$\epsilon_{m\lambda}$	$f_{\lambda}$	$\mu_{\lambda}$	$\epsilon_{\lambda}$	$I_{\lambda}$
2.484+00	7.637-01	6.401-02	3.233-01	7.502-01	8.600-02
2.554+00	7.915-01	6.497-02	3.516-01	7.787-01	8.286-02
2.625+00	8.165-01	6.588-02	3.805-01	8.045-01	7.952-02
2.695+00	8.329-01	6.672-02	4.016-01	8.214-01	7.549-02
2.765+00	8.324-01	6.749-02	4.008-01	8.208-01	7.020-02
2.835+00	8.036-01	6.820-02	3.646-01	7.907-01	6.299-02
2.905+00	7.648-01	6.885-02	3.235-01	7.504-01	5.572-02
2.993+00	7.145-01	6.958-02	2.794-01	6.984-01	4.757-02
3.091+00	6.521-01	7.030-02	2.346-01	6.345-01	3.933-02
3.188+00	5.884-01	7.089-02	1.966-01	5.698-01	3.221-02
3.285+00	5.425-01	7.138-02	1.728-01	5.236-01	2.703-02
3.382+00	5.092-01	7.177-02	1.571-01	4.902-01	2.315-02
3.480+00	4.784-01	7.205-02	1.434-01	4.595-01	1.988-02
3.577+00	4.704-01	7.224-02	1.400-01	4.516-01	1.793-02
3.674+00	4.805-01	7.234-02	1.443-01	4.616-01	1.684-02
3.772+00	5.042-01	7.234-02	1.547-01	4.851-01	1.630-02
3.869+00	5.243-01	7.225-02	1.640-01	5.052-01	1.564-02
3.966+00	5.117-01	7.208-02	1.582-01	4.927-01	1.409-02
4.063+00	5.832-01	7.182-02	1.937-01	5.644-01	1.492-02
4.161+00	6.091-01	7.148-02	2.082-01	5.906-01	1.445-02
4.258+00	6.430-01	7.106-02	2.287-01	6.251-01	1.418-02
4.453+00	7.221-01	6.999-02	2.855-01	7.061-01	1.382-02
4.647+00	8.041-01	6.865-02	3.651-01	7.911-01	1.342-02
4.825+00	8.761-01	6.719-02	4.695-01	8.666-01	1.295-02
4.991+00	8.383-01	6.565-02	4.093-01	8.272-01	1.103-02
5.157+00	8.611-01	6.395-02	4.442-01	8.513-01	1.015-02
5.322+00	8.092-01	6.211-02	3.723-01	7.976-01	8.527-03
5.488+00	7.950-01	6.013-02	3.564-01	7.832-01	7.531-03
5.654+00	7.944-01	5.803-02	3.561-01	7.830-01	6.789-03
5.819+00	7.861-01	5.583-02	3.475-01	7.748-01	6.074-03
5.985+00	8.371-01	5.353-02	4.100-01	8.278-01	5.881-03
6.151+00	8.604-01	5.115-02	4.457-01	8.522-01	5.499-03
6.314+00	7.717-01	4.874-02	3.339-01	7.613-01	4.477-03
6.458+00	7.415-01	4.658-02	3.059-01	7.309-01	3.967-03
6.602+00	7.315-01	4.438-02	2.977-01	7.211-01	3.619-03
6.746+00	7.123-01	4.217-02	2.822-01	7.021-01	3.262-03
7.321+00	7.384-01	3.327-02	3.055-01	7.304-01	2.529-03
7.848+00	8.001-01	2.542-02	3.687-01	7.943-01	2.138-03
8.299+00	9.575-01	1.928-02	7.216-01	9.548-01	2.095-03
8.747+00	9.626-01	1.397-02	7.511-01	9.601-01	1.736-03
9.150+00	6.190-01	1.011-02	2.227-01	6.154-01	9.427-04

Table 3 (Continued)  
 RUN NO. 50 [H2O] 0.5132  $T_c$  4841 or  $\leq 3.718 \cdot 10^{-1}$

$\lambda$ micron	$f_{\lambda}$	$\epsilon_{\lambda}$	$I_{\lambda}$
1.140+00	5.718-02	3.170-02	1.329-02
1.163+00	4.929-02	3.250-02	1.140-02
1.187+00	4.516-02	3.332-02	1.041-02
1.210+00	8.896-02	3.410-02	2.099-02
1.233+00	1.749-01	3.486-02	4.333-02
1.245+00	2.285-01	3.526-02	5.850-02
1.258+00	2.716-01	3.569-02	7.149-02
1.273+00	2.903-01	3.618-02	7.735-02
1.288+00	3.374-01	3.666-02	9.288-02
1.303+00	3.702-01	3.714-02	1.044-01
1.317+00	3.904-01	3.759-02	1.117-01
1.332+00	3.944-01	3.806-02	1.132-01
1.347+00	3.987-01	3.853-02	1.147-01
1.362+00	3.971-01	3.900-02	1.141-01
1.377+00	3.903-01	3.946-02	1.115-01
1.392+00	3.769-01	3.992-02	1.065-01
1.414+00	3.568-01	4.059-02	9.930-02
1.436+00	3.324-01	4.125-02	9.083-02
1.458+00	3.023-01	4.190-02	8.083-02
1.480+00	2.718-01	4.254-02	7.114-02
1.502+00	2.509-01	4.318-02	6.473-02
1.524+00	2.404-01	4.381-02	6.156-02
1.546+00	2.430-01	4.443-02	6.230-02
1.568+00	2.736-01	4.504-02	7.154-02
1.591+00	3.358-01	4.567-02	9.166-02
1.619+00	4.322-01	4.643-02	1.270-01
1.649+00	4.861-01	4.722-02	1.495-01
1.679+00	5.309-01	4.801-02	1.700-01
1.709+00	5.989-01	4.878-02	2.055-01
1.739+00	5.944-01	4.953-02	2.029-01
1.770+00	5.894-01	5.030-02	2.000-01
1.800+00	5.806-01	5.102-02	1.951-01
1.830+00	5.672-01	5.174-02	1.878-01
1.860+00	5.344-01	5.244-02	1.712-01
1.896+00	4.982-01	5.326-02	1.542-01
1.938+00	4.588-01	5.419-02	1.370-01
1.980+00	4.436-01	5.510-02	1.307-01
2.022+00	4.418-01	5.598-02	1.299-01
2.063+00	4.557-01	5.681-02	1.355-01
2.105+00	5.125-01	5.764-02	1.602-01
2.147+00	5.841-01	5.845-02	1.960-01
2.189+00	6.269-01	5.923-02	2.204-01
2.231+00	6.862-01	5.998-02	2.596-01
2.275+00	7.433-01	6.075-02	3.051-01
2.348+00	7.638-01	6.195-02	3.238-01
2.415+00	7.968-01	6.300-02	3.578-01
2.485+00	8.309-01	6.403-02	3.994-01
2.555+00	8.698-01	6.499-02	4.587-01
2.625+00	8.949-01	6.588-02	5.072-01
2.695+00	9.267-01	6.672-02	5.886-01

Table 3. (Continued)  
 RUN NO. 50 [H<sub>2</sub>O] 0.5132 T<sub>c</sub> 4841 °R C 3.718-01

micron	m <sub>λ</sub>	f <sub>λ</sub>	μ <sub>λ</sub>	ε <sub>λ</sub>	I <sub>λ</sub>
2.765+00	9.356-01	6.749-02	6.175-01	9.293-01	7.079-02
2.835+00	8.877-01	6.820-02	4.916-01	8.787-01	6.248-02
2.905+00	8.316-01	6.885-02	3.994-01	8.198-01	5.445-02
2.992+00	7.547-01	6.958-02	3.138-01	7.398-01	4.520-02
3.088+00	6.826-01	7.028-02	2.553-01	6.656-01	3.711-02
3.185+00	7.243-01	7.087-02	2.871-01	7.082-01	3.610-02
3.281+00	5.673-01	7.136-02	1.854-01	5.485-01	2.560-02
3.378+00	5.418-01	7.175-02	1.725-01	5.228-01	2.237-02
3.475+00	5.228-01	7.204-02	1.633-01	5.037-01	1.979-02
3.571+00	5.211-01	7.223-02	1.625-01	5.020-01	1.814-02
3.668+00	5.492-01	7.233-02	1.760-01	5.301-01	1.764-02
3.764+00	5.732-01	7.234-02	1.883-01	5.542-01	1.701-02
3.861+00	6.107-01	7.226-02	2.090-01	5.920-01	1.678-02
3.957+00	6.431-01	7.210-02	2.286-01	6.249-01	1.638-02
4.054+00	6.743-01	7.185-02	2.493-01	6.568-01	1.594-02
4.151+00	7.083-01	7.151-02	2.742-01	6.916-01	1.557-02
4.247+00	7.605-01	7.111-02	3.190-01	7.455-01	1.558-02
4.344+00	8.188-01	7.062-02	3.824-01	8.061-01	1.566-02
4.440+00	8.612-01	7.007-02	4.431-01	8.506-01	1.538-02
4.537+00	9.047-01	6.944-02	5.286-01	8.964-01	1.510-02
4.633+00	9.688-01	6.876-02	7.782-01	9.645-01	1.515-02
4.730+00	9.998-01	6.800-02	1.410+00	9.976-01	1.463-02
4.814+00	9.998-01	6.729-02	1.410+00	9.976-01	1.380-02
4.898+00	9.998-01	6.653-02	1.410+00	9.976-01	1.302-02
4.982+00	9.998-01	6.574-02	1.411+00	9.976-01	1.230-02
5.066+00	9.998-01	6.490-02	1.411+00	9.976-01	1.163-02
5.150+00	9.998-01	6.402-02	1.411+00	9.977-01	1.100-02
5.234+00	9.998-01	6.311-02	1.411+00	9.977-01	1.041-02
5.318+00	9.740-01	6.216-02	8.194-01	9.703-01	9.588-03
5.402+00	9.838-01	6.117-02	9.199-01	9.807-01	9.185-03
5.486+00	9.778-01	6.015-02	8.538-01	9.743-01	8.656-03
5.570+00	9.382-01	5.910-02	6.287-01	9.326-01	7.863-03
5.654+00	9.177-01	5.803-02	5.643-01	9.112-01	7.296-03
5.737+00	9.336-01	5.693-02	6.131-01	9.279-01	7.061-03
5.821+00	9.113-01	5.580-02	5.479-01	9.047-01	6.546-03
5.905+00	9.522-01	5.465-02	6.873-01	9.476-01	6.524-03
5.989+00	9.246-01	5.347-02	5.852-01	9.188-01	6.022-03
6.752+00	8.066-01	4.207-02	3.731-01	7.982-01	3.431-03
7.469+00	8.930-01	3.102-02	5.106-01	8.881-01	2.660-03
8.074+00	8.902-01	2.226-02	5.065-01	8.862-01	2.003-03
8.635+00	5.667-01	1.521-02	1.923-01	5.618-01	9.942-04
9.152+00	9.704-01	1.009-02	8.034-01	9.681-01	1.384-03

Table 3. (Continued)  
 RUN NO. 53 [H2O] 0.4465  $T_c$  54.6 °R  $\epsilon$  2.268-01

micron	$\tau_{\text{min}}$	$f_{\lambda}$	$\mu_{\lambda}$	$\xi_{\lambda}$	$I_{\lambda}$
1.140+00	4.807-02	3.170-02	1.112-02	4.657-02	2.853-02
1.163+00	4.479-02	3.250-02	1.033-02	4.335-02	2.611-02
1.187+00	3.787-02	3.332-02	8.696-03	3.662-02	2.166-02
1.210+00	4.121-02	3.410-02	9.473-03	3.982-02	2.311-02
1.233+00	6.095-02	3.486-02	1.415-02	5.890-02	3.350-02
1.245+00	7.105-02	3.526-02	1.658-02	6.865-02	3.865-02
1.258+00	9.722-02	3.569-02	2.301-02	9.399-02	5.227-02
1.273+00	1.313-01	3.618-02	3.167-02	1.270-01	6.968-02
1.288+00	1.635-01	3.666-02	4.017-02	1.583-01	8.561-02
1.303+00	1.854-01	3.714-02	4.613-02	1.796-01	9.573-02
1.317+00	2.149-01	3.759-02	5.444-02	2.083-01	1.094-01
1.332+00	2.378-01	3.806-02	6.110-02	2.306-01	1.193-01
1.347+00	2.493-01	3.853-02	6.450-02	2.417-01	1.232-01
1.362+00	2.672-01	3.900-02	6.993-02	2.592-01	1.301-01
1.377+00	2.781-01	3.946-02	7.329-02	2.698-01	1.333-01
1.392+00	2.816-01	3.992-02	7.435-02	2.731-01	1.328-01
1.414+00	2.796-01	4.059-02	7.369-02	2.710-01	1.287-01
1.436+00	2.694-01	4.125-02	7.047-02	2.609-01	1.209-01
1.458+00	2.627-01	4.190-02	6.838-02	2.542-01	1.149-01
1.480+00	2.462-01	4.254-02	6.336-02	2.380-01	1.050-01
1.502+00	2.288-01	4.318-02	5.819-02	2.209-01	9.503-02
1.524+00	2.138-01	4.381-02	5.383-02	2.062-01	8.648-02
1.547+00	1.972-01	4.445-02	4.911-02	1.900-01	7.766-02
1.569+00	1.899-01	4.507-02	4.705-02	1.828-01	7.283-02
1.591+00	1.876-01	4.567-02	4.639-02	1.805-01	7.007-02
1.619+00	2.136-01	4.643-02	5.365-02	2.056-01	7.719-02
1.649+00	2.632-01	4.722-02	6.822-02	2.537-01	9.191-02
1.679+00	3.236-01	4.801-02	8.739-02	3.126-01	1.093-01
1.709+00	3.755-01	4.878-02	1.053-01	3.635-01	1.225-01
1.739+00	4.038-01	4.953-02	1.157-01	3.912-01	1.272-01
1.770+00	4.196-01	5.030-02	1.217-01	4.066-01	1.275-01
1.800+00	4.321-01	5.102-02	1.265-01	4.188-01	1.266-01
1.830+00	4.416-01	5.174-02	1.302-01	4.281-01	1.248-01
1.860+00	4.440-01	5.244-02	1.311-01	4.303-01	1.209-01
1.896+00	4.354-01	5.326-02	1.276-01	4.215-01	1.135-01
1.937+00	4.196-01	5.417-02	1.213-01	4.057-01	1.039-01
1.979+00	3.910-01	5.508-02	1.104-01	3.773-01	9.187-02
2.021+00	3.541-01	5.596-02	9.715-02	3.408-01	7.895-02
2.063+00	3.267-01	5.681-02	8.779-02	3.138-01	6.917-02
2.104+00	3.254-01	5.763-02	8.730-02	3.124-01	6.553-02
2.146+00	3.377-01	5.843-02	9.135-02	3.242-01	6.475-02
2.188+00	3.857-01	5.921-02	1.081-01	3.711-01	7.057-02
2.229+00	4.238-01	5.995-02	1.224-01	4.085-01	7.399-02
2.272+00	4.883-01	6.070-02	1.490-01	4.722-01	8.143-02
2.341+00	5.363-01	6.184-02	1.710-01	5.198-01	8.274-02
2.411+00	5.811-01	6.294-02	1.937-01	5.645-01	8.302-02
2.481+00	6.034-01	6.397-02	2.060-01	5.867-01	7.981-02
2.550+00	6.291-01	6.492-02	2.209-01	6.124-01	7.713-02
2.620+00	6.513-01	6.582-02	2.348-01	6.347-01	7.408-02
2.690+00	6.682-01	6.666-02	2.459-01	6.517-01	7.056-02

Table 3. (Continued)  
 RUN NO. 53 [H<sub>2</sub>O] 0.4465 T<sub>c</sub> 5486 °R E 2.268-01

$\lambda$ micron	$\epsilon_{m\lambda}$	$f_\lambda$	$\mu_\lambda$	$\epsilon_\lambda$	$I_\lambda$
2.759+00	6.897-01	6.743-02	2.609-01	6.735-01	6.771-02
2.829+00	7.064-01	6.814-02	2.733-01	6.904-01	6.453-02
2.899+00	6.882-01	6.880-02	2.596-01	6.717-01	5.842-02
2.983+00	6.570-01	6.951-02	2.379-01	6.397-01	5.103-02
3.081+00	6.261-01	7.023-02	2.184-01	6.081-01	4.402-02
3.178+00	5.718-01	7.083-02	1.878-01	5.531-01	3.641-02
3.274+00	5.199-01	7.133-02	1.621-01	5.010-01	3.004-02
3.373+00	4.780-01	7.173-02	1.433-01	4.592-01	2.512-02
3.470+00	4.384-01	7.203-02	1.270-01	4.200-01	2.100-02
3.567+00	4.221-01	7.223-02	1.206-01	4.039-01	1.849-02
3.665+00	4.093-01	7.233-02	1.157-01	3.913-01	1.643-02
3.762+00	4.279-01	7.234-02	1.228-01	4.096-01	1.581-02
3.859+00	4.460-01	7.226-02	1.300-01	4.274-01	1.518-02
3.956+00	4.710-01	7.210-02	1.403-01	4.522-01	1.480-02
4.054+00	5.051-01	7.185-02	1.552-01	4.861-01	1.469-02
4.151+00	5.314-01	7.151-02	1.675-01	5.125-01	1.431-02
4.248+00	5.672-01	7.110-02	1.853-01	5.485-01	1.418-02
4.346+00	5.898-01	7.061-02	1.974-01	5.713-01	1.369-02
4.443+00	6.194-01	7.005-02	2.144-01	6.014-01	1.337-02
4.540+00	6.465-01	6.942-02	2.311-01	6.290-01	1.300-02
4.637+00	6.707-01	6.873-02	2.473-01	6.538-01	1.257-02
4.734+00	6.858-01	6.796-02	2.580-01	6.694-01	1.200-02
4.818+00	7.205-01	6.725-02	2.846-01	7.051-01	1.190-02
4.902+00	7.500-01	6.650-02	3.101-01	7.356-01	1.170-02
4.985+00	7.392-01	6.571-02	3.006-01	7.246-01	1.087-02
5.069+00	7.543-01	6.487-02	3.143-01	7.403-01	1.049-02
5.153+00	7.603-01	6.399-02	3.201-01	7.467-01	9.992-03
5.237+00	7.773-01	6.307-02	3.370-01	7.644-01	9.671-03
5.320+00	7.776-01	6.213-02	3.374-01	7.649-01	9.156-03
5.404+00	8.162-01	6.115-02	3.810-01	8.050-01	9.124-03
5.488+00	7.703-01	6.013-02	3.305-01	7.577-01	8.138-03
5.571+00	7.273-01	5.909-02	2.916-01	7.138-01	7.269-03
5.655+00	7.348-01	5.801-02	2.981-01	7.217-01	6.973-03
5.739+00	7.611-01	5.691-02	3.221-01	7.489-01	6.870-03
5.823+00	7.675-01	5.578-02	3.285-01	7.557-01	6.586-03
5.906+00	7.512-01	5.463-02	3.133-01	7.392-01	6.125-03
5.990+00	7.148-01	5.346-02	2.824-01	7.022-01	5.535-03
6.753+00	8.866-01	4.206-02	4.950-01	8.804-01	4.516-03
7.472+00	9.165-01	3.097-02	5.670-01	9.122-01	3.240-03
8.084+00	9.999-01	2.212-02	1.432+00	9.979-01	2.656-03
8.656+00	9.966-01	1.497-02	1.214+00	9.945-01	2.057-03
9.164+00	9.999-01	9.994-03	1.435+00	9.979-01	1.670-03

## EXPERIMENTAL METHOD

The principal elements of the experimental set-up are represented schematically in Fig. 1.1. The combustion system may be regarded basically as small liquid propellant rocket motor with a gas pressurized feed system. The motor consists of an impinging stream injector, a combustion chamber, a radiation window assembly, and a converging nozzle. Each component was water cooled. Cooling was necessary to obtain steady state conditions for run duration of 90 sec at combustion temperatures up to 6000°F. The propellants and the coolant were supplied from high-pressure tanks. Nitrogen gas was used for pressurizing the propellant and the cooling water tanks. Tank pressures of 1500 psi were found to be sufficient to maintain a steady combustion pressure of the order of 700 psi for the present experiments. The numerous pressurizing and control valves and electrical circuits have been omitted from Fig.1.1 and will not be discussed in detail. Apart from the instrumentation utilized for measuring the radiation, the over-all flow control and instrumentation systems were little different from those conventionally employed for rocket combustion research. Photographs of the instrument and the remote control consoles are shown in Figs. 1.2 and 1.3.

All liquid flow rates were measured with Potter turbine-type flowmeters. The flow of the N<sub>2</sub> gas that was admitted through the aperture was measured with a sonic orifice. Wianko transducers were used for measuring all static and differential pressures, such as coolant, injector, tank, and combustion pressures. The output of each primary element was recorded with a single-trace high-speed recording potentiometer.

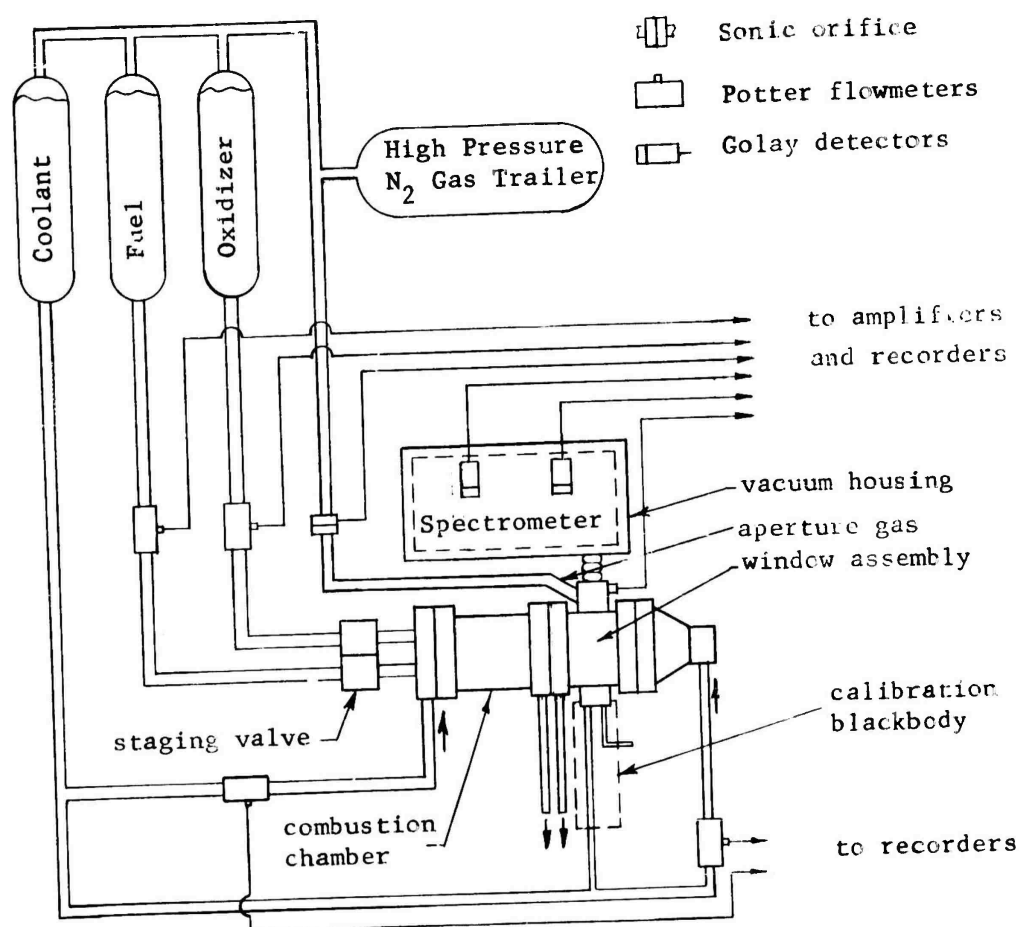


Fig. 1.1 Experimental Flow Systems

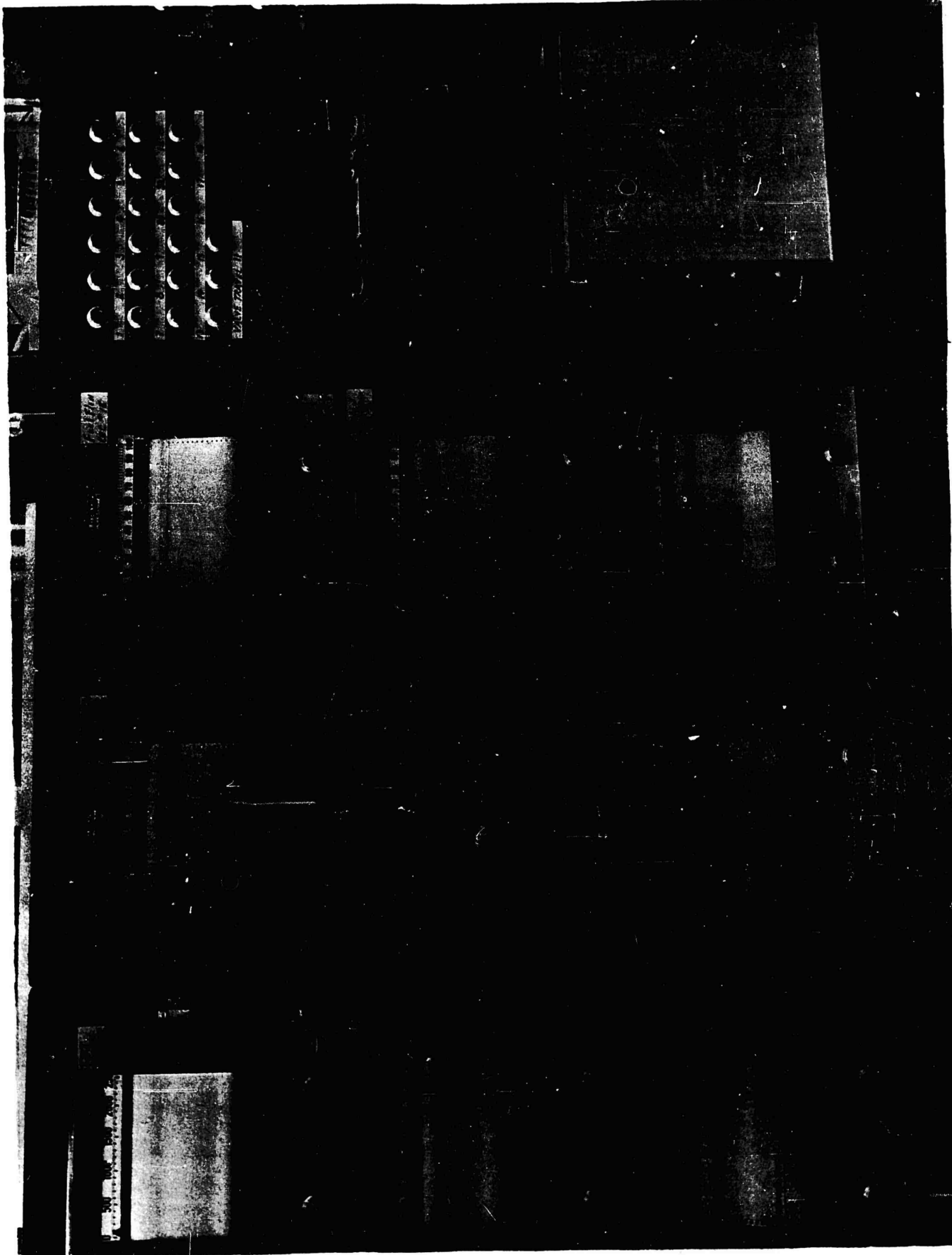


Fig. 1.2 Instrument Console

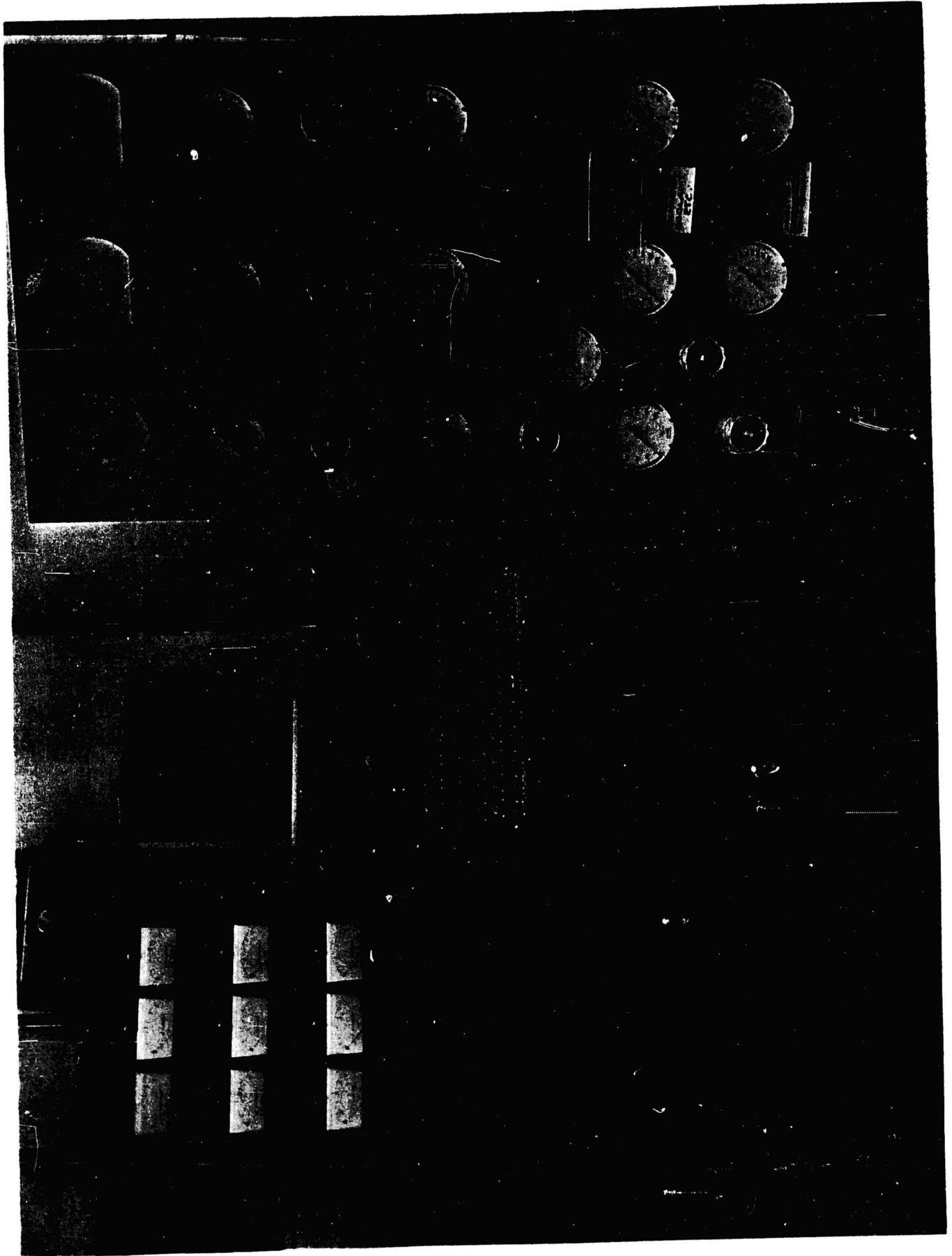


FIG. 1.3 Control Console

As a rule, each recording channel from the primary sensing element to the recorder was calibrated immediately before each run. High-precision Heise gages were employed as a secondary standard for calibrating the pressure recording instruments. In the case of the flow measuring systems, only the recorder circuits were calibrated before each run. However, the flowmeters were calibrated periodically with water by the customary weighing method.

The detail design of the combustion chamber is illustrated in Fig. 1.4. The combustion gas was observed through a multiple disk collimator situated over a small (0.09 in. dia.) aperture in the wall of the combustion chamber. Back-flow of the hot combustion was excluded from the aperture chamber by the small but steady flow of  $N_2$  gas through the aperture. The aperture gas, as we will call it, was admitted into the aperture chamber through the shutter control housing. The gas then flowed through the collimator disks and finally through the aperture and into the combustion chamber. The aperture and collimator technique was employed instead of a transparent window in order to avoid the transmission problems that usually arise from window clouding caused by combustion gas deposits.

Actually, there were two holes in the chamber wall, but light was emitted through only one of them. In order to minimize the dilution effects of aperture flow on the combustion gas stream, part of the aperture gas was by-passed through a second hole in order to turn the aperture gas flow downstream along the inner wall of the combustion chamber. The details of the diversion aperture are shown in the insert of Fig.1.4. It will be noted that the cross section of the diversion aperture was annular. The outlet was blocked by an approximately  $45^\circ$  turn in the channel. The angular impingement of the secondary flow forced the main aperture flow downstream and out of the optical path across the combustion chamber.

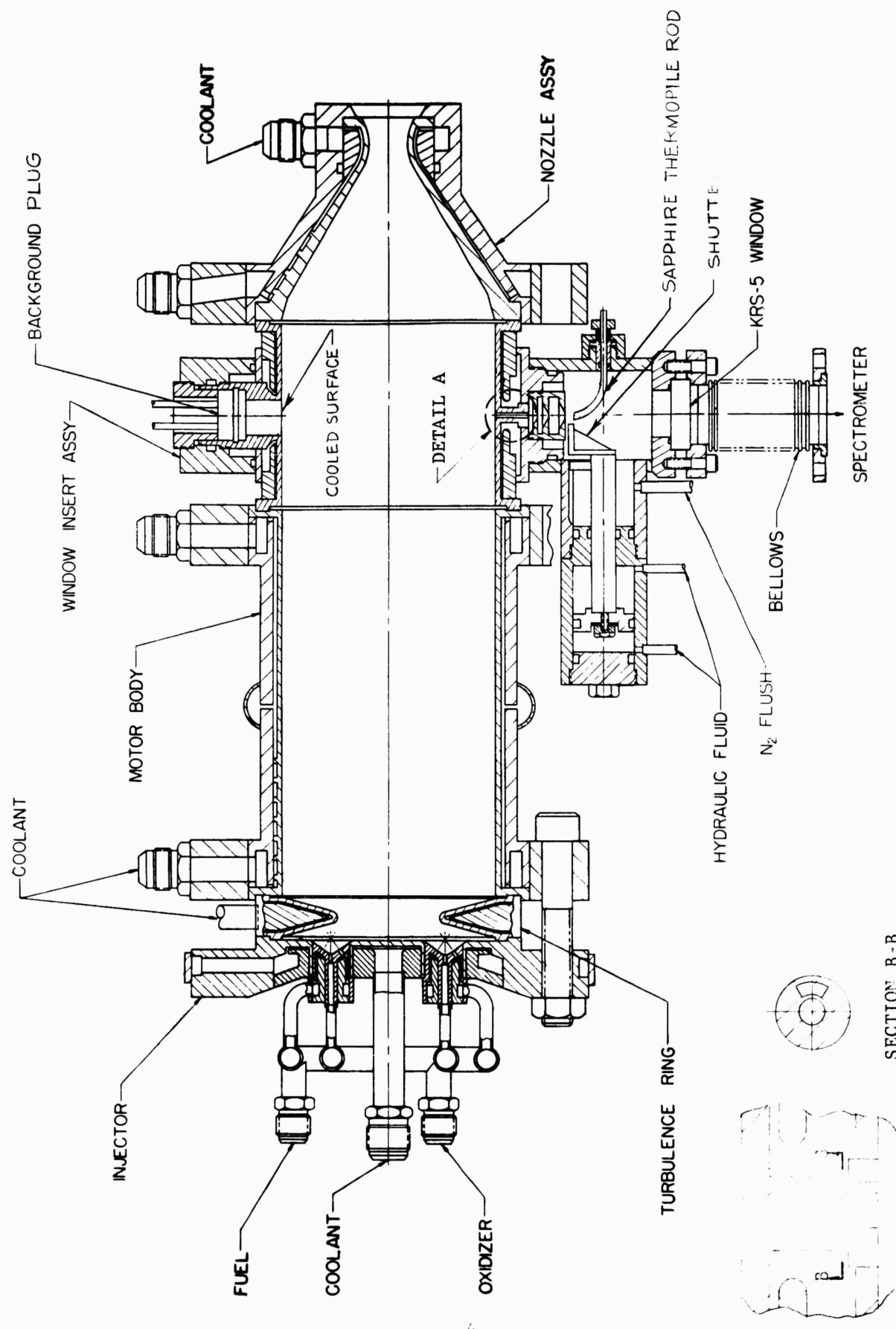


FIG. 1.4 THRUST CHAMBER ASSEMBLY

DETAIL A

The total radiant energy was detected with a 10-junction thermopile. The thermopile housing (not shown) was attached to the end of the sapphire rod shown in the figure so that the thermopile element saw essentially only the end of the rod. The use of a semi-transparent rod and locating the thermopile outside the aperture housing was found to be necessary in order to prevent unpredictable cold-junction effects. Although the flow of  $N_2$  gas through the aperture housing was small, the sensitiveness of the thermopile to small temperature changes was so acute that direct observation of the gas proved to be impossible.

The spectral intensity of the radiation emitted through the aperture was measured with a custom-built recording spectrometer. This instrument was equipped with two Beckman IR-4 monochrometers, each of which was equipped with a Golay-cell detector. One monochrometer was designed to scan from  $.5\mu$  to  $15\mu$ ; the other from  $1\mu$  to  $25\mu$ . The short wavelength monochrometer was equipped with a NaCl prism, while the long wavelength monochrometer was equipped with a prism. Both detectors had CsBr windows.

The light from the aperture was directed first to one monochrometer and then to the other by means of the chopper and mirror scheme\* shown in Fig.1.5. The rotating chopper disk is essentially a semi-circular plate with a mirror on the side facing the incoming radiation. During one-half of the rotation cycle, the mirror reflects the radiation to one optical system, during the other half of the cycle the radiation passes through the chopper opening to the other optical system. The monochrometers, detectors with their pre-amplifiers, and the chopper and mirror systems were all housed in a single vacuum chamber. The

---

\*The scheme shown in Fig.5 represents only the final arrangement. In the first design, the incoming beam of light was split in half by a  $45^\circ$  triangular mirror. This method was abandoned because the intensity was too low for satisfactory measurement.

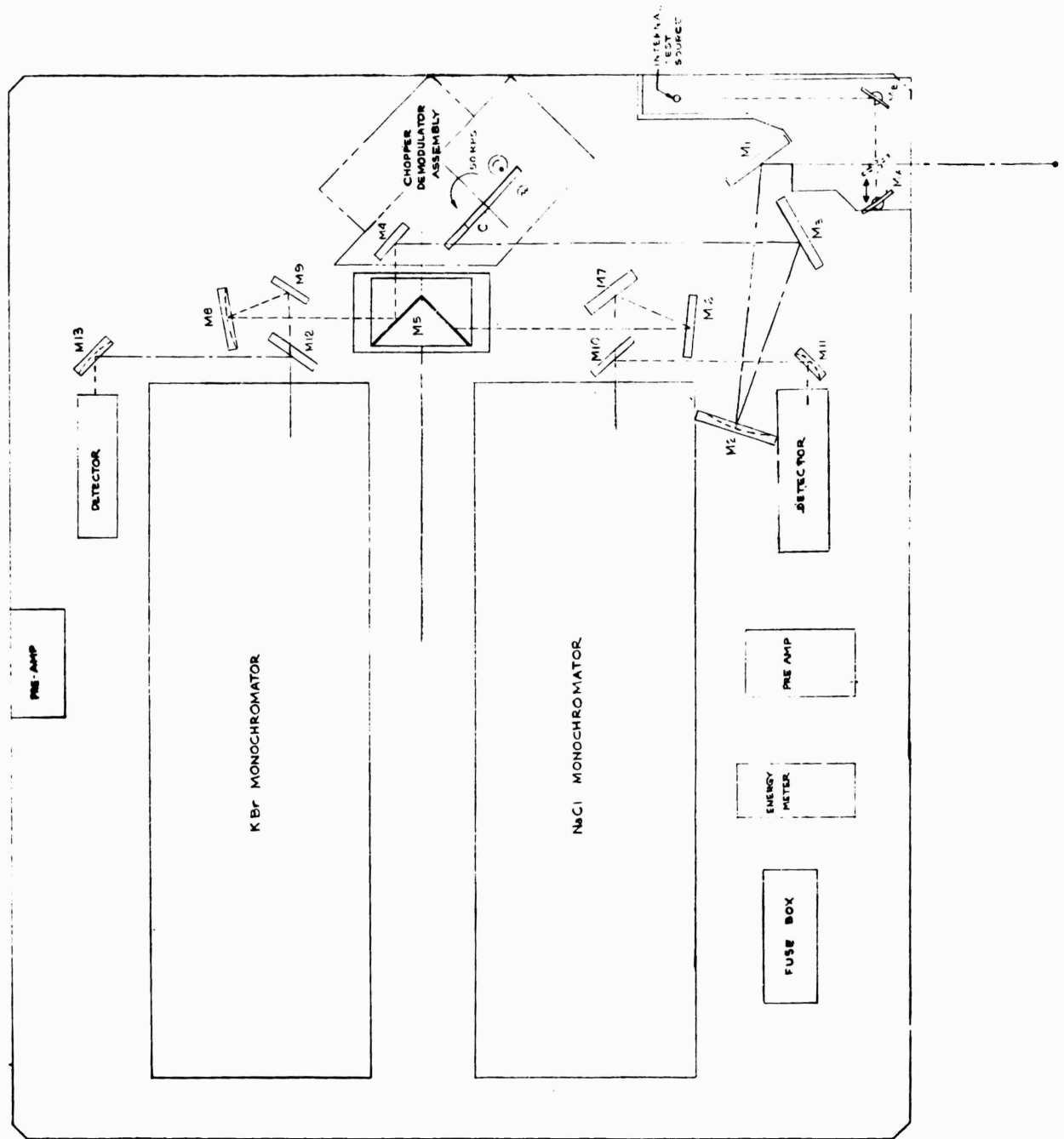


Fig. 1.5 Spectrometer System



0111402

Fig. 1.6 Spectrometer Amplifying and Recording System

light from the aperture was admitted through a hole in the wall of the vacuum chamber which was coupled to the window assembly by means of a flexible bellows.

Obtaining a measurement of both the total emission and the spectral distribution in one run required about 90 sec of steady state operation. The motor was first ignited using an excess flow of nitrogen gas through the aperture to prevent any possible surge of combustion gas from entering the aperture chamber. As the combustion pressure increased, the aperture gas flow decreased automatically to a prescribed steady state value, which was usually less than 1 percent of the total propellant flow rate. After steady combustion had been reached, a trace of about 10-sec duration of the thermopile output was traced on the recorder. The thermopile rod was then rotated out of the light path and a continuous trace of the spectral intensity was obtained with the spectrometer. The radiation from the aperture and collimator was "piped" to the thermopile element through the 1/8 in. curved sapphire rod. The spectrometer collecting mirror observed the aperture through the KRS-5 (potassium thallium iodide) window situated at the end of the aperture chamber.

Neither radiation instrument provides absolute intensity measurements since the response of the detector and complete optical system of each instrument is calibrated against a source of known intensity. Emitters of the glow-bar type are useful only for temperatures below 2500° F. Emission at higher temperatures is available from other sources such as the carbon arc or tungsten lamp. But unfortunately they do not emit truly black radiation over the complete spectrum. Nor, in fact, is the emission even grey. For the present problem, however, the chief disadvantage of the arc devices is the small field of view provided. Collecting and focusing lenses were found necessary in order to develop a detectable signal through the chamber aperture. Since the transmission properties

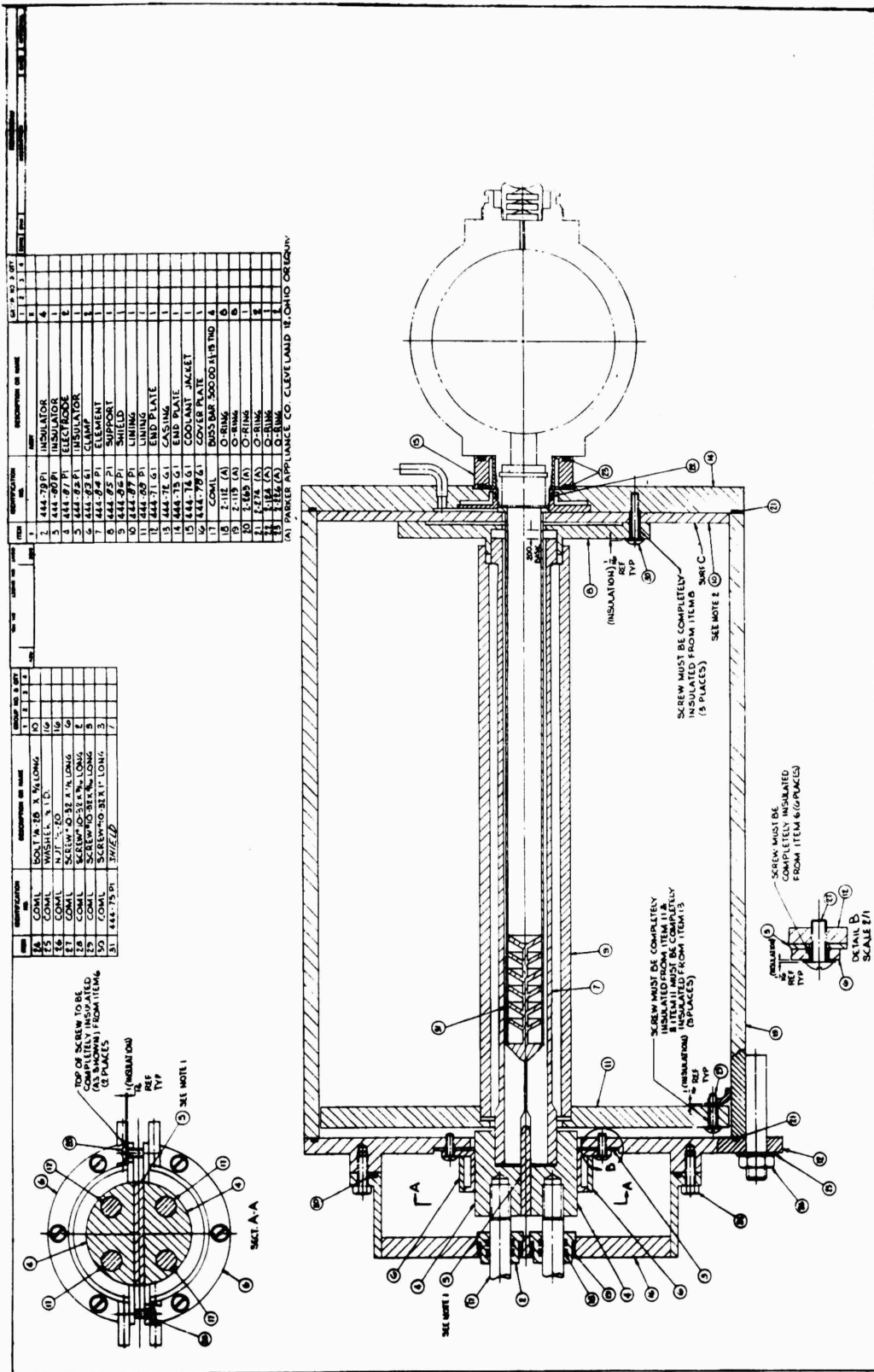
of the lenses were unknown or unpredictable, this method had to be abandoned.

Instead, an electrically heated graphite cavity that required no lenses was developed for calibration purposes. A cross section of the blackbody is shown in Fig. 1.7. The current conductor is formed by the outer graphite cylinder which is split axially to provide a greater total electrical resistance. Only the outer cylinder is heated electrically. The black cavity is formed by the thin graphite inner liner which is heated by radiation from the current carrying element. Temperatures of  $6000^{\circ}\text{R}$  were obtained on the inner surface of the cavity by forcing a small flow of argon gas through the blackbody and combustion chamber to prevent oxidation. The flow of argon also provided a transparent medium for purging the air from the chamber during the calibration procedures.

The relative size and arrangement of the experimental apparatus is pictured better in the photograph presented in Fig. 1.8. The blackbody is shown to the left of the motor in position for calibration. A heavy vacuum housing covers the spectrometer which is located on a massive concrete block to minimize vibration effects. The thermopile system is located between the motor and the vacuum housing. The blackbody is shown to the left of the motor in place for calibration.

Prior to each run, the blackbody was attached to the motor and the thermopile and spectrometer systems were calibrated. The blackbody was then removed and was replaced by a water-cooled copper plug. The plug serves as an essentially non-radiating background for observing the emission from the gas. The chamber with the background plug in position for a test run is shown in Fig. 1.9.

Fig.1.7. Cross Section of Laboratory Blackbody.



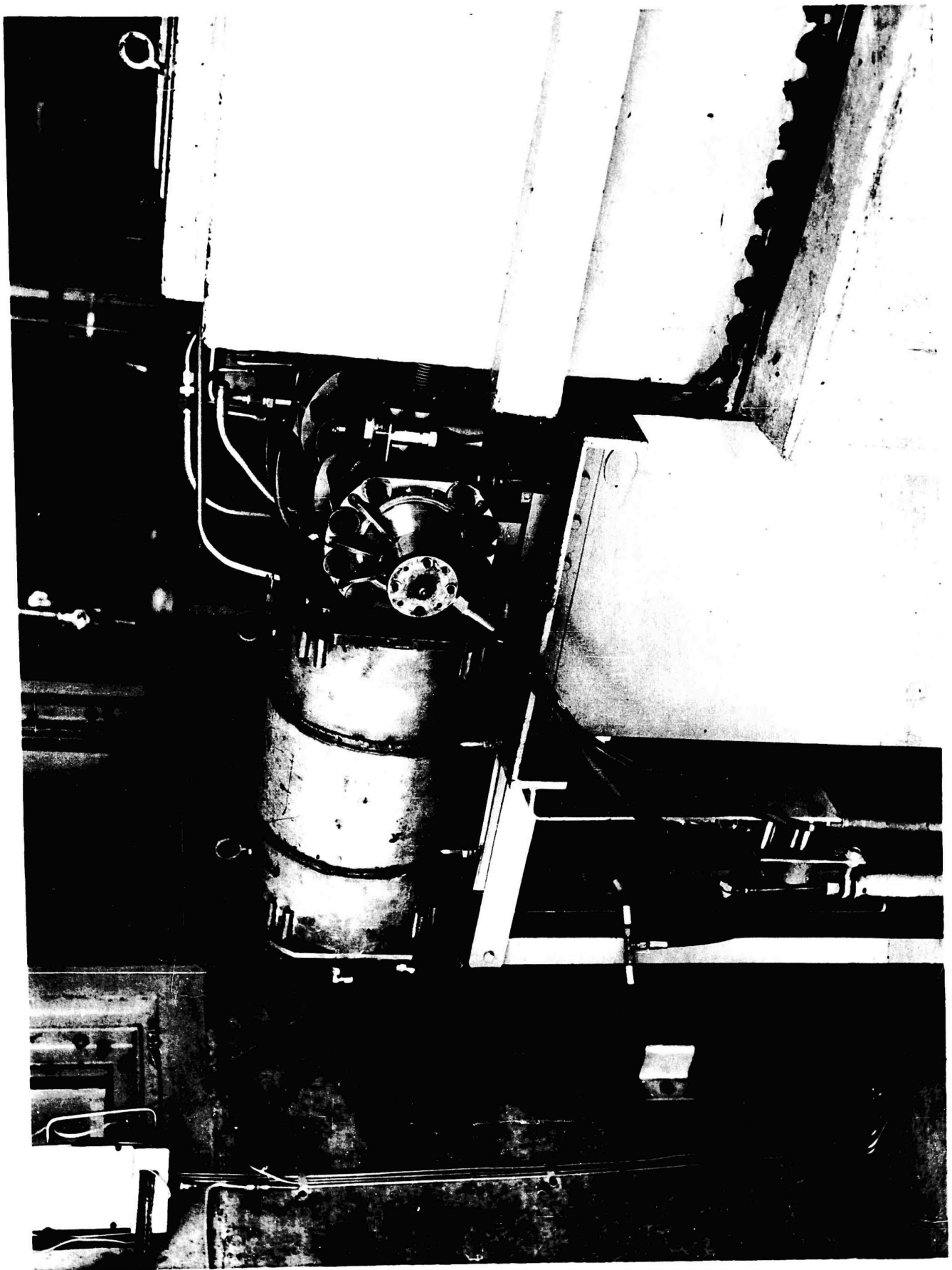
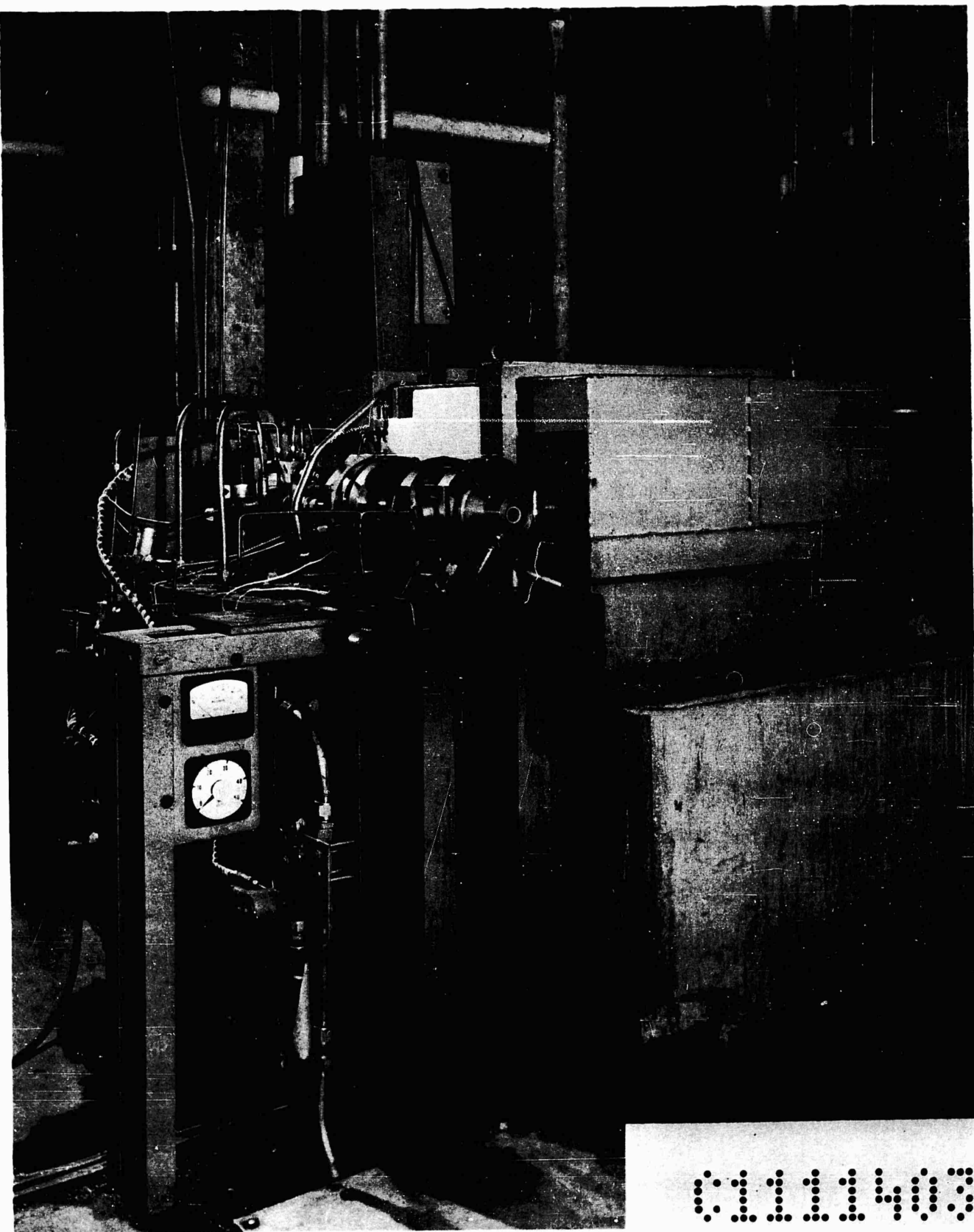


Fig. 1.8 Experimental Apparatus with Blackbody Attached for Calibration



0111403

Fig. 1.9 Experimental Apparatus Ready for Test

## THEORETICAL CONSIDERATIONS

Measured emissivities. The optical system used to measure the infrared radiation from the combustion gas is shown in Fig. 2.1 below, along with the important dimensions of the combustion chamber. The detector receives energy

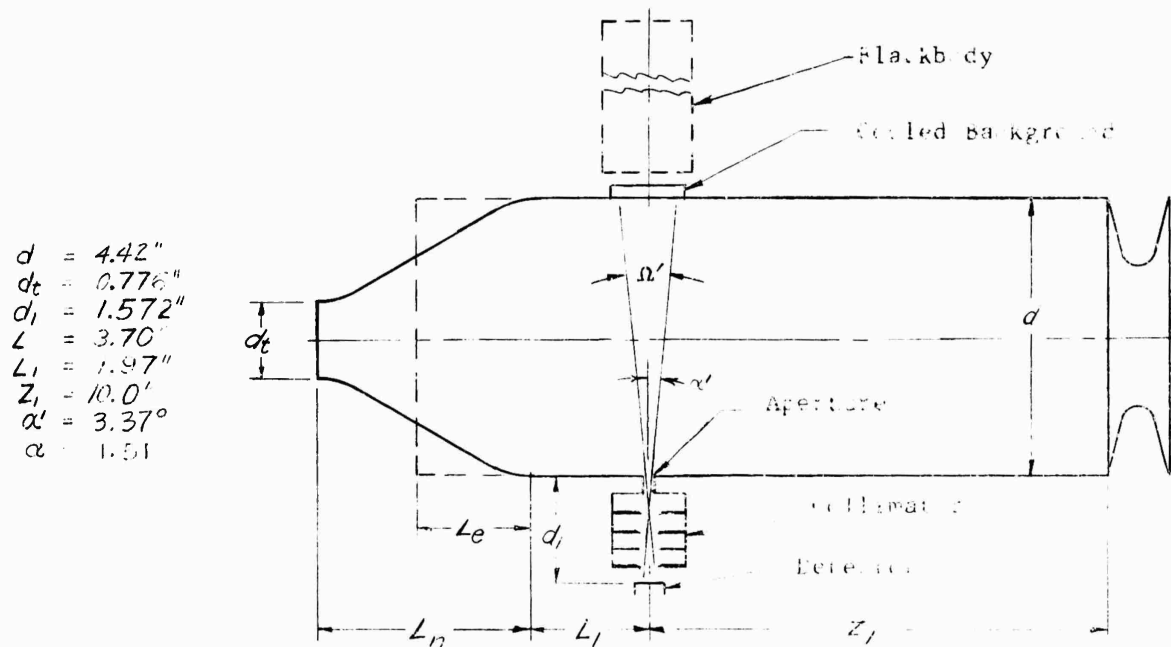


Fig. 2.1 Chamber Geometry

from the chamber through a small aperture in the wall. The field of view is restricted by means of a pitchole collimator equipped with three collimating lenses. Inserted in the wall of the chamber opposite the aperture is a cooled background plate that forms a plane surface. The background plate was designed so that it could be removed and replaced by a high-temperature blackbody or "hohlraum" for calibration purposes.

The experimental measurements obtained with the above apparatus provide curves of the total and the spectral intensity of the radiation emitted from the interior of the chamber, along with curves of the total and spectral emission from the calibration blackbody. The character of the measured spectral intensities is illustrated in Fig. 2.2. The smooth curve denoted by  $B_{m\lambda}$  represents the distribution received from a blackbody radiating at a temperature equal to the temperature of the combustion gas. The irregular curve denoted by  $I_{m\lambda}$  represents the relative spectral intensity of the radiation received from the combustion gas.

Although all the radiation observed by the detector stems initially from the combustion gas, only part of this is due to direct emission from the gas. The field of view permitted by the aperture and collimator is denoted by the solid angle  $\Omega'$  in Fig. 2.1. Looking through the angle  $\alpha'$ , the detector sees the direct emission from the gas bounded by  $\Omega'$  plus the radiation emanating from the back wall surface subtending  $\Omega'$ . The radiation from the back wall is due in part to thermal emission that originates in the wall and in part to reflection. Since the temperature of the background surface was never more than  $250^{\circ}\text{F}$ , the direct emission from this surface is small and can be neglected. The reflected radiation is not negligible, however. The background surface receives radiation from the whole interior of the combustion chamber, and with ordinary materials approximately one-half of this is reflected into the space about each unit area seen by the detector. A significant fraction of reflected radiation falls within  $\Omega'$  and will reach the detector. Consequently, the observed radiant intensity

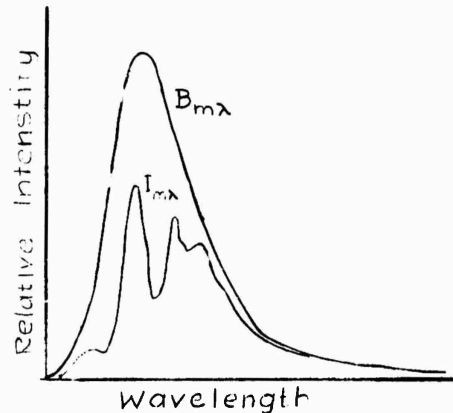


Fig. 2.2 Typical Spectral Distribution

must be considered to be an apparent intensity rather than the true intensity of radiation emitted by the gas.

With this in mind, let us define an apparent or measured spectral emissivity by the ratio

$$\epsilon_{m\lambda} = \frac{I_{m\lambda}}{B_{m\lambda}} \quad (2.1)$$

where  $I_{m\lambda}$  and  $B_{m\lambda}$  refer respectively to the observed intensities received from the combustion chamber and the blackbody cavity as illustrated in Fig. 2.2. Similarly we can also determine an apparent total emissivity as

$$\epsilon_m = \frac{\int_0^{\infty} I_{m\lambda} d\lambda}{\int_0^{\infty} B_{m\lambda} d\lambda} \quad (2.2)$$

Expressed in this form only the measured emissivities are of little general use. In order to apply the data to a combustion system of unarbitrary size and shape or to different operating conditions, it will be necessary to express the measured emissivities in terms of the optical depth and other radiating properties of gases.

Calculation of the radiant intensity from theory involves the integration of several transcendental functions over the interior volume and surface of the chamber. These integrals cannot be reduced in closed form for the true geometry of the chamber (Fig. 2.1). A solution to the general problem requires the use of numerical or graphical integration which will not be attempted here. It will be seen, however, that the major portion of the combustion envelope essentially forms a right circular cylinder. Thus, little error will be introduced if we replace the conical nozzle by a cylindrical section that has the proper effective length.

The most satisfactory approximation of this length is the effective or hemispherical beam length which is given<sup>(4)\*</sup> approximately by

$$L_1 \simeq \frac{4V}{A} \quad (2.3)$$

where  $V$  is the volume and  $A$  is the surface area of the gaseous envelope. The length of a cylinder of diameter  $d$  having the same beam length as the conical nozzle can be obtained by equating the volume-to-area ratios of each configuration. If these ratios are then expressed in terms of the chamber and throat diameters, and the result is solved for the length  $L_1$ , we get for the effective length

$$L_1 = \frac{\beta d}{2(1-\beta)} \quad (2.4)$$

where

$$\beta = \frac{\frac{4L_n}{3d}[(d+d_t)^2 - dd_t]}{(d+d_t)\sqrt{L_n^2 + (d-d_t)^2 + d^2 + d_t^2}}$$

For the dimensions prescribed in Fig. 2.1, the above equations give an effective length of  $L_1 = 2.767$  in. Adding this length to the chamber section downstream from the aperture results in an effective cylindrical volume having a diameter of  $d = 4.42$  in., a length of  $Z_1 = 10.00$  in. upstream, and a length of  $Z_2 = 4.74$  in. downstream from the aperture (see Fig. 2.3). Hereafter, any reference to the combustion envelope will mean the effective envelope prescribed by the above dimensions.

We turn now to the problem of calculating the radiation received by the detector. The geometry of the radiating system is illustrated in Fig. 2.3. The element  $dA$  represents a unit area of the detector receiver. This element is exposed to the

---

\*Raised numbers in parentheses refer to the references given in appendix .

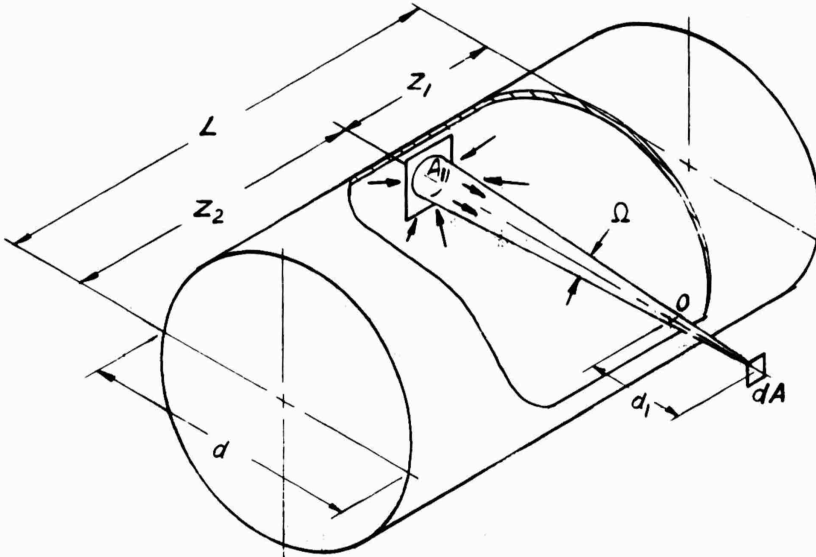


Fig. 2.3 Effective Cylindrical Volume

energy emitted through the aperture from the field of view denoted by the solid angle  $\Omega$ . The surface of the backplate is denoted by  $A_1$ , and an element of this surface by  $dA_1$ .

In order to correct the measured emissivities for reflection we must first express the flux of radiation that impinges on the element  $dA$  in terms of the emission properties of the gas. For the sake of brevity, we will omit the basic derivations and proofs connected with the transfer of radiation. The fundamentals are well established and can be found in any comprehensive text on the subject, for instance, see references 1, 4, 7, or 12. However, in the following treatment, we will begin with the one-dimensional transfer equation for emitting gases, which is not as widely used, and it will be helpful at this point to discuss briefly several of the important terms that enter radiation theory.

In any radiating medium, the quantity of energy per unit time in the wavelength interval  $(\lambda, \lambda + d\lambda)$  that flows through an element of area  $dA$  and the solid angle  $d\omega$  which makes an angle  $\psi$  with respect to the normal to  $dA$  is

$$d\mathfrak{F}_\lambda = I_\lambda \cos \psi dA d\omega d\lambda \quad (2.5)$$

where  $I_\lambda$  is called the specific intensity (or frequently the areal intensity) of radiation. Equation 2.5\* is sometimes regarded as the definition of  $I_\lambda$ .

In the discussion that follows, consider each of the following variables to be functions of the location of the point  $r$  ( $x, y, z$ ) in a radiation field, where  $r$  is the position vector measured from an arbitrary origin, and we define

$\rho$  = density of the radiating medium

$\kappa_\lambda$  = monochromatic mass absorption coefficient =  $(r, \lambda)$

$\epsilon_\lambda$  = monochromatic emission coefficient =  $(r, \kappa_\lambda, \lambda)$

$B_\lambda$  = Planck's function for black radiation =  $B(T, \lambda)$

and finally the source function which, after Refs. 8 and 12, is defined as

$$\mathfrak{J} = \frac{\epsilon_\lambda}{\kappa_\lambda} \quad (2.6)$$

The absorption coefficient  $\kappa_\lambda$  is the familiar factor of proportionality that appears in the fundamental law of linear absorption given by

$$dI_\lambda = -\kappa_\lambda \rho I_\lambda ds \quad (2.7)$$

Here  $ds$  represents the differential change of thickness measured along  $s$ .

The emission coefficient  $\epsilon_\lambda$  merely defines the quantity of energy per unit time emitted by a unit mass  $dm$  into the solid angle  $d\omega$  and over the wavelength

---

\*The flux differential  $d\mathfrak{F}$  is considered to be a third order differential.

interval  $(\lambda, \lambda + d\lambda)$ ; that is,

$$d\mathfrak{I}_{e\lambda} = \mathcal{E}_\lambda dm d\omega d\lambda \quad (2.8)$$

With the above definitions, the transfer equation for an emitting gas can be written

$$\frac{dI_\lambda}{ds} = \kappa_\lambda \rho (\mathfrak{I} - I_\lambda) \quad (2.9)$$

This equation follows almost directly from the definitions of  $\kappa_\lambda$  and  $\mathcal{E}_\lambda$  and the definition of the derivative (see Ref. 12).

If the temperature gradient at every point  $r(x, y, z)$  in a radiating field is small, the medium is said to be in local equilibrium. In this instance the laws established by Kirchoff for an isothermal enclosure hold closely in the vicinity of the point, and the emission coefficient is given accordingly by

$$\mathcal{E}_\lambda = \kappa B_\lambda \quad (2.10)$$

where  $B_\lambda$  is Planck's function for black radiation. This restriction makes it possible to eliminate the source function and express the transfer equation in terms of  $B_\lambda$ . Thus, on making use of Kirchoff's law (2.10) and the definition of the source function (2.6) the transfer equation becomes

$$\frac{dI_\lambda}{ds} = \kappa_\lambda \rho (B_\lambda - I_\lambda) \quad (2.11)$$

where we have replaced  $\rho\mu$  by a new absorption coefficient  $\mu_\lambda$ .

It should be mentioned that (2.11) breaks down if the temperature of the radiating field is not essentially uniform.

We now assume that the above condition of local thermodynamic equilibrium is satisfied throughout the total volume pictured in Fig. 2.3. The combustion products in the experimental chamber can be considered essentially isothermal except near the throat of the nozzle and near the injector and in the narrow boundary regions adjacent to the walls. It is possible to derive an approximate temperature distribution and solve (2.11) for the non-isothermal regions, but the effort seems hardly worthwhile in view of the uncertainty surrounding the use of the transfer equation where strong temperature gradients are present. Actually, the boundary zones make up a relatively small fraction of the total volume, and the error introduced by assuming an isothermal state should not be critical. The same remarks apply to the pressure and composition of the combustion gas.

With these assumptions, Planck's function  $B_\lambda$ , the mass absorption coefficient  $\kappa_\lambda$ , and the density  $\rho$  become independent of the position  $s$ , and thus  $\mu_\lambda$  may be regarded as a constant in (2.11). The transfer equation can be written conveniently in the following form

$$\frac{d(I_\lambda - B_\lambda)}{I_\lambda - B_\lambda} = -\mu_\lambda ds \quad (2.12)$$

If we take  $I_\lambda = I_{o\lambda}$  when  $s = 0$ , integration of (2.12) yields\*

$$I_\lambda = B_\lambda(1 - e^{-\mu s}) + I_{o\lambda} e^{-\mu s} \quad (2.13)$$

where the intensity  $I_{o\lambda}$  may be an external source. This is regarded as the basic law of emission for distributed radiators. Since  $B_\lambda$  is the same throughout the medium, (2.13) demonstrates the important characteristic that in traveling the distance  $s$  the intensity of the emitted radiation is attenuated by the factor  $e^{-\mu s}$  because of

---

\*For convenience, the  $\sim$  script will be omitted from  $\mu_\lambda$ .

absorption. The fraction of  $B_\lambda$  and  $I_{o\lambda}$  actually observed at  $s$  is

$$B_\lambda e^{-\mu s}, \text{ and } I_{o\lambda} e^{-\mu s} \quad (2.14)$$

Let us return now to the problem of determining the total radiation emitted from the observation aperture. It will be convenient for the present discussion to consider the cone of view separately as shown in Fig. 2.4. The element  $dA$  represents a spot in the center of the thermopile receiver, and the plane  $A_1$  represents the surface of the background plate.

The detector element receives emission from the volume element and indirect radiation due to reflection from the surface element  $dA_1$ . According to Equations (2.8)

and (2.10), the direct emission from the element of mass  $dm = \rho dV$  is

$$dF = \mu B_\lambda dV d\omega d\lambda \quad (2.15)$$

where

$$\mu = \rho \kappa_\lambda \quad (2.16)$$

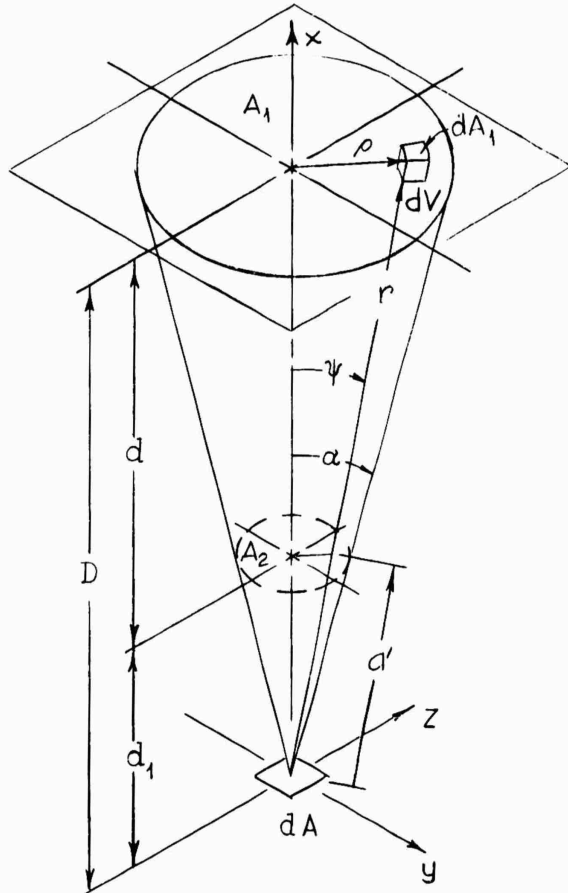


Fig. 2.4 Cone of View

The solid angle  $d\omega$  subtended by  $dA$  is

$$d\omega = \cos \psi \frac{dA}{r^2} \quad (2.17)$$

Thus, the energy that leaves  $dV$  toward  $dA$  is

$$d\mathfrak{F} = \mu B_\lambda \cos \psi \frac{dA}{r^2} dV d\lambda \quad (2.18)$$

According to (2.14) the emitted energy is diminished by the factor  $e^{-\mu(r-a')}$  in traveling the distance\*  $s = r-a'$ .

In order to simplify the notation, let  $q_\lambda$  denote the radiant energy per unit time per unit area, i.e.,

$$q_\lambda = \frac{d\mathfrak{F}}{dA} \quad (2.19)$$

Then the flux per unit wave length that reaches  $dA$  is

$$\frac{dq_\lambda}{d\lambda} = \mu B_\lambda \cos \psi \frac{e^{-\mu(r-a')}}{r^2} dV \quad (2.20)$$

To determine the contribution due to reflection, we assume now that  $A_1$  is a diffuse reflector and denote the specific intensity of radiation that is reflected from  $dA_1$  by  $I_{f\lambda}$ . Applying (2.5), the energy that leaves  $dA_1$  toward  $dA$  is

$$d\mathfrak{F}_{f\lambda} = I_{f\lambda} \cos \psi dA_1 d\omega d\lambda \quad (2.21)$$

---

\*The region described by the distance  $a'$  lies outside the chamber and was filled with a transparent gas.

Again, only part of this energy actually reaches  $dA$ . Thus, using 2.17 for  $d\omega$ , the reflected flux seen by  $dA$  is

$$\frac{dq_{f\lambda}}{d\lambda} = I_{f\lambda} \cos^2 \psi \frac{e^{-\mu(r_1 - \alpha')}}{r_1^2} dA_1 \quad (2.22)$$

where  $r_1$  represents the value of  $r$  on the surface  $A_1$ .

The combined flux per unit wave length received by  $dA$  from the volume element and the area element is the sum of the two contributions given by (2.18) and (2.22); i.e.,

$$\frac{dq_\lambda}{d\lambda} = I_{f\lambda} \cos^2 \psi \frac{e^{-\mu(r_1 - \alpha')}}{r_1^2} dA_1 + \mu B_\lambda \cos \psi \frac{e^{-\mu(r - \alpha')}}{r^2} dV \quad (2.23)$$

Integrating (2.23) over the volume  $V$  and the area  $A$  gives the total flux per unit wave length

$$\frac{dq_\lambda}{d\lambda} = \int_{A_1} I_{f\lambda} \cos^2 \psi \frac{e^{-\mu(r_1 - \alpha')}}{r_1^2} dA_1 + \mu B_\lambda \int_V \cos \psi \frac{e^{-\mu(r - \alpha')}}{r^2} dV \quad (2.24)$$

The spacial integrals can be reduced easily by transforming to spherical coordinates. Let us choose  $\phi$  and  $\psi$  as shown in Fig. 2.4 as the independent variables for the area integral, and  $\phi$ ,  $r$ , and  $\psi$  as the independent variables for the volume integral. Utilizing the Jacobian in order to transform from rectilinear to curvilinear coordinates gives

$$dA_1 = J\left(\frac{x,y}{\phi, \psi}\right) d\phi d\psi = D^2 \tan \psi \sec^2 \psi d\phi d\psi \quad (2.25)$$

and

$$dv = J\left(\frac{x,y,z}{\phi, r, \psi}\right) d\phi dr d\psi = r^2 \sin \psi d\phi dr d\psi \quad (2.26)$$

Thus, the flux represented by (2.24) can be expressed as

$$\frac{dq_\lambda}{d\lambda} = \int_0^\alpha \int_0^{2\pi} I_{f\lambda} e^{-\mu d \sec \psi} \sin \psi \cos \psi d\psi + \mu B_\lambda \int_0^\alpha \int_0^{2\pi} \int_\alpha^\infty e^{-\mu(r-a)} \sin \psi \cos \psi dr d\psi \quad (2.27)$$

Since the observed portion of the background surface is relatively small,  $I_{f\lambda}$  is substantially constant over A.

On this basis, integration of (2.27) first with respect to  $r$  and then with respect to  $\omega$  yields

$$\frac{dq_\lambda}{d\lambda} = 2\pi B_\lambda \int_0^\alpha \sin \psi d(\sin \psi) - 2\pi(B_\lambda - I_\lambda) \int_0^\alpha e^{-\mu d \sec \psi} \sin \psi \cos \psi d\psi \quad (2.28)$$

The first of the two integrals above is an elementary form. The second integral can be reduced by partial integration to a function of the exponential integral\*

if we let

$$u = \mu d \sec \psi$$

\*This integral can also be evaluated in terms of the logarithmic integral by taking  $\log u = -\mu d \sec \psi$ .

from which we find

$$\sin \psi \cos \psi d\psi = (\mu d)^2 \frac{du}{u^3}$$

Integration of the first term of (2.28) and substitution of the new variable from above into (2.28) results in

$$\frac{dq_\lambda}{d\lambda} = \pi B_\lambda \sin^2 \alpha - 2\pi (B_\lambda - I_{f\lambda}) (\mu d)^2 \int_{\mu d}^{\mu d \sec \alpha} \frac{e^{-u}}{u^3} du \quad (2.29)$$

which on integrating by parts reduces to

$$\frac{dq_\lambda}{d\lambda} = \pi B_\lambda \sin^2 \alpha - \pi (B_\lambda - I_{f\lambda}) \left[ (\mu d)^2 \int \frac{e^{-u}}{u} du + \left( \frac{1}{u} - \frac{1}{u^2} \right) (\mu d)^2 e^{-u} \right]_{\mu d}^{\mu d \sec \alpha}$$

It will be convenient now to denote the bracketed factor by  $\phi_1(\mu)$ . Inserting the limits as indicated and noting that the remaining integral term is the so-called exponential integral, we obtain

$$\phi_1(\mu) = (\mu d)^2 \left[ Ei(-\mu d \sec \alpha) - Ei(-\mu d) \right] + \frac{1 - \mu d}{e^{\mu d}} - \frac{(cosec \alpha - \mu d) cosec \alpha}{e^{\mu d \sec \alpha}} \quad (2.30)$$

The radiant flux per unit wave length can be written finally as

$$\frac{dq_\lambda}{d\lambda} = \pi B_\lambda \left[ \sin^2 \alpha - \left( 1 - \frac{I_{f\lambda}}{B_\lambda} \right) \phi_1(\mu) \right] \quad (2.31)$$

Equation (2.31) shows that the flux received by the detector over the wavelength interval  $d\lambda$  is a function of the optical depth  $\mu d$ . Since, as we will show later, the reflected intensity  $I_{f\lambda}$  can be expressed as an explicit function of  $\mu d$ , (2.31) provides an implicit equation in the single variable  $\mu$  (or if preferred in  $\kappa_\lambda$ ).

Before we take up the problem of determining  $I_{f\lambda}$  it will be worthwhile at this point to compare (2.31) with an approximate but somewhat simpler relationship for  $dq_\lambda / d\lambda$  that can be derived directly from (2.13). Let us suppose that the surfaces  $A_1$  and  $A_2$  shown in Fig. 2.4 are sectors of two concentric spheres, with corresponding radii of  $r = r_1$  and  $a' = d_1$ . Referring now to (2.13), let  $I_{o\lambda} = I_{f\lambda}$ , and assume that this is constant over  $A_1$ . Then

$$I_\lambda = B_\lambda - (B_\lambda - I_{f\lambda}) e^{-\mu d} \quad (2.32)$$

since  $s = (r_1 - d_1) = d$

Substituting this in (2.5) and integrating over the solid angle  $\Omega$  gives

$$\begin{aligned} \frac{dq_\lambda}{d\lambda} &= \int_{\Omega} I_\lambda \cos \psi d\omega \\ &= [B_\lambda(1 - e^{-\mu d}) + I_{f\lambda} e^{-\mu d}] \int_0^\alpha 2\pi \sin \psi \cos \psi d\psi \\ &= \pi B_\lambda \left[ \sin^2 \alpha - \left(1 - \frac{I_{f\lambda}}{B_\lambda}\right) e^{-\mu d} \sin^2 \alpha \right] \end{aligned} \quad (2.33)$$

This is identical to the result that we would obtain from (2.28) by taking

$s = r - d_1 = d$  instead of  $s = d \sin \psi$  in the exponential factor of the second integral. On comparing (2.33) with (2.31) it is evident that

$$\phi_1(\mu) \simeq e^{-\mu d} \sin^2 \alpha \quad (2.34)$$

Actually, (2.33) should provide a very close approximation for  $dq_\lambda/d\lambda$  since the angle  $\alpha$  employed in the present experimental work was less than  $2^\circ$ .

Reflected Intensity. We return now to the problem of determining the intensity of the radiation reflected from  $A_1$ . Unfortunately, a rigorous determination of  $I_{f\lambda}$  involves an integral equation in which  $I_{f\lambda}$  itself must be integrated over the total surface of the envelope. A solution of the integral for the cylindrical surface shown in Fig. 2.3 is possible only by tedious numerical integration and iteration procedures, which are out of the question for the present problem. However, we can obtain a close approximation for  $I_{f\lambda}$  by means of the following approach.

Consider a unit area  $dA_1$  at  $x = 0$  as shown in the cylindrical volume of Fig 2.5. Since  $dA_1$  sees the total gas volume, the gas emission incident on  $dA_1$ , is from (2.8).

$$\frac{dS_{e\lambda}}{d\lambda} = \mu B_\lambda \int_V \cos \psi \frac{e^{-\mu r}}{r^2} dv dA_1 \quad (2.35)$$

The total radiation emitted by the cylindrical gas volume is obviously the integral of  $dS_{e\lambda}/d\lambda$  over the entire surface of the enclosure. Thus,

$$\frac{dS_{t\lambda}}{d\lambda} = \mu B_\lambda \int_{A_1} \int_V \cos \psi \frac{e^{-\mu r}}{r^2} dv dA_1 \quad (2.36)$$

Part of this energy is absorbed and part is reflected. If we assume that diffuse reflection occurs and that the hemispherical reflectivity (denoted by  $f_\lambda$ )\* is constant over the surface, then on the average the reflected intensity is

$$I_{f\lambda} \simeq \frac{\mu f_\lambda B_\lambda}{\pi A_1} \int_{A_1} \int_V \cos \psi \frac{e^{-\mu r}}{r^2} dV dA_1$$

$$\simeq \frac{\mu f_\lambda B_\lambda}{\pi} \int_V \cos \psi \frac{e^{-\mu r}}{r^2} dV \quad (2.37)$$

In obtaining 2.37, we have assumed that the volume integral does not vary greatly from one point to another on  $A_1$ , or is otherwise a suitable mean value.

Reduction of this integral for a cylindrical enclosure can be accomplished now by transforming to polar coordinates. For this purpose, consider a volume element  $dV$  at any arbitrary point  $P$ , within the enclosure. In cylindrical coordinates

$$dV = dz d\sigma d\rho$$

$$\cos \psi = \frac{\rho \cos \sigma}{r}$$

and

$$r^2 = z^2 + \rho^2$$

The duplicate use of  $\rho$ , earlier for density and here as a variable of integration, should cause no confusion since the density is now

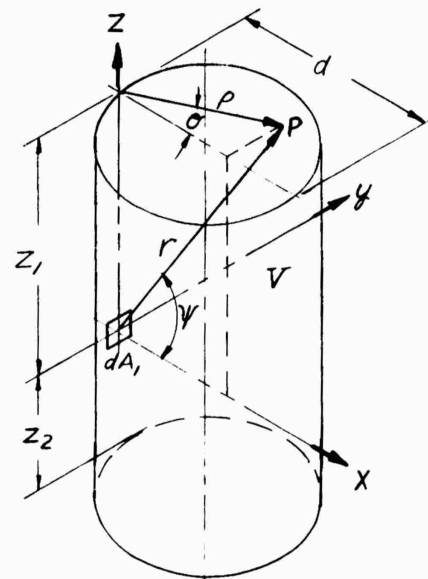


Fig. 2.5 Polar Coordinate System

contained in the factor  $\mu$ . Hence,

$$I_{f\lambda} = \frac{2f\mu B_\lambda}{\pi} \int_0^d \int_0^\sigma \int_{-z_2}^{z_1} \frac{\cos \sigma e^{-\mu r}}{r^3} \rho^2 dz d\sigma d\rho \quad (2.38)$$

The presence of the exponential factor makes it impossible to integrate (2.38) in closed form. The exponential factor can be expanded in an infinite series of irrational algebraic functions, either circular or hyperbolic functions, and the integration with respect to  $z$  and  $\sigma$  can be carried out term by term without difficulty. However, the resulting series cannot be integrated with respect to  $\rho$ , without introducing additional approximations which lead eventually to a triple summation of an extremely large number of terms.

To avoid this, we will adopt the easier approach of approximating  $e^{-\mu r}$  by means of a third degree\* function of the form

$$e^{-\mu r} \approx a r^3 + b r + c \quad (2.39)$$

The use of the cubic function does not result in a closed integral, but it does provide an answer in terms of elliptical integrals.

A good fit for (2.39) is obtained if the coefficients  $a$ ,  $b$ , and  $c$  are determined so that the expression is satisfied for the minimum and maximum values of  $r$  (viz., for  $r = 0$ , and  $r = r_m$ ), and for an intermediate value of  $r = r_m/2$

\*The subscript  $\lambda$  is omitted from  $I_\lambda$  hereafter for convenience.

\*A slightly better fit of  $e^{-\mu r}$  can be obtained with a second degree approximation but the presence of a second power term leads to an unintegrable function in (2.38).

The maximum value of  $r$ , for the cylindrical volume pictured in Fig. 2.5 is

$$r_m = \sqrt{d^2 + z_1^2} \quad (2.40)$$

Substituting  $r = 0$ , and  $r = r_m$ , in (2.39) and in the derivative of (2.39) provides three equations in  $r_m$  which can be solved simultaneously for the coefficients  $a$ ,  $b$ , and  $c$ . The result is

$$a = \frac{1 - (2 - e^{-\frac{\mu}{2}r_m})e^{-\frac{\mu}{2}r_m}}{\frac{3}{4}r_m^3} \quad (2.41)$$

$$b = -\frac{7 - (8 - e^{-\frac{\mu}{2}r_m})e^{-\frac{\mu}{2}r_m}}{3r_m} \quad (2.42)$$

$$c = 1 \quad (2.43)$$

The two functions are shown

in Fig. 2.6. If  $\mu$  is of the order of  $0.05 \text{ in.}^{-1}$ , the two functions differ by less than 1 per cent over the range  $0 \leq r \leq r_m$ . Departures from the true value no larger than this are quite satisfactory for the present analysis.

If we now use (2.39) to replace  $e^{-\mu r}$ , and consider for the present only the cylindrical volume designated by  $z_1$  in Fig. 2.5, the

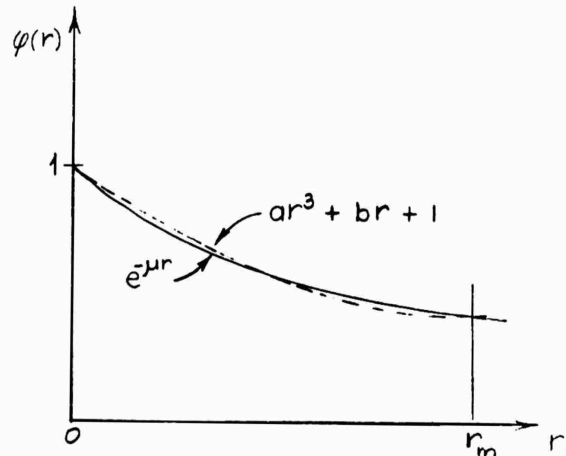


Fig. 2.6. Empirical Fit  
of  $e^{-\mu r}$

intensity of the reflected radiation becomes from (2.38)

$$\frac{\pi I_{f\lambda}}{2f\mu B_\lambda} = \int_0^d \int_0^\sigma \int_0^{z_1} \left[ a + \frac{b}{\rho^2 + z^2} + \frac{1}{(\rho^2 + z^2)^{3/2}} \right] \rho^2 \cos \sigma dz d\sigma d\rho \quad (2.44)$$

The integrand of (2.44) contains only elementary functions of  $z$  and  $\sigma$  and can be integrated readily with respect to these two variables. The first two integrations give

$$\frac{\pi I_{f\lambda}}{2f\mu B_\lambda} = \int_0^d \left( az_1 + \frac{b}{\rho} \operatorname{ctn} \frac{\rho}{z_1} + \frac{z_1}{\rho^2 \sqrt{z_1^2 + \rho^2}} \right) \rho^2 \sin \sigma d\rho \quad (2.45)$$

The final integration, that is with respect to  $\rho$ , is not so straightforward. First, we express  $\sin \sigma$  in terms of  $\rho$ . Referring to Fig. 2.5, it will be seen that on the cylindrical boundary

$$\rho = d \cos \sigma \quad (2.45)$$

or

$$d \sin \sigma = \sqrt{d^2 - \rho^2} \quad (2.47)$$

Hence, on replacing  $\sin \sigma$  in 2.45, we get

$$\frac{\pi d I_{f\lambda}}{2f\mu B_\lambda} = az_1 \int_0^d \rho^2 \sqrt{d^2 - \rho^2} d\rho + b \int_0^d \rho \sqrt{d^2 - \rho^2} \operatorname{ctn} \frac{\rho}{z_1} d\rho + z_1 \int_0^d \frac{\sqrt{d^2 - \rho^2}}{\sqrt{z_1^2 + \rho^2}} d\rho \quad (2.48)$$

$$= \mathcal{I}_1 + \mathcal{I}_2 + \mathcal{I}_3$$

The first integral of (2.48) is an elementary integral that can be reduced easily by trigonometric substitution or obtained directly from common integral tables. Accordingly,

$$\mathcal{J}_1 = \frac{\pi a z_1 d^4}{16} \quad (2.49)$$

The second term can be reduced to integrable functions by integrating by parts. The partial integration yields

$$\mathcal{J}_2 = \frac{\pi b d}{6} - \frac{b z_1}{3} \int_0^d \frac{(d^2 - \rho^2)^2 d\rho}{(z_1^2 + \rho^2) \sqrt{d^2 - \rho^2}} \quad (2.50)$$

The remaining integral in (2.50) can be expressed as three integrable terms by expanding the numerator of the integrand and dividing by  $z_1^2 + \rho^2$ . This results in

$$\mathcal{J}_2 = \frac{\pi b d^3}{6} + \frac{b z_1}{3} \left[ \int_0^d \sqrt{d^2 - \rho^2} d\rho + (z_1^2 + d^2) \int_0^d \frac{d\rho}{\sqrt{d^2 - \rho^2}} - (z_1^2 + d^2) \int_0^d \frac{d\rho}{(z_1^2 + \rho^2) \sqrt{d^2 - \rho^2}} \right] \quad (2.51)$$

Each integral in the bracketed member can be reduced readily now by trigonometric substitution\*. The final result for  $\mathcal{J}_2$  is

---

\*Let  $\rho = d \sin \sigma$ , and in the last integral multiply numerator and denominator by  $\sec^2 \sigma$ , and express the result in terms of  $\tan \sigma$ .

$$\mathcal{J}_2 = \frac{\pi b z_1^3}{5} \left[ 1 + \frac{3}{2} \left( \frac{d}{z_1} \right)^2 + \left( \frac{d}{z_1} \right)^3 - \left( 1 + \frac{d^2}{z_1^2} \right)^{3/2} \right] \quad (2.52)$$

The third and final integral of (2.48) reduces directly to a function of elliptic integrals by substituting  $\rho = d \cos \sigma$  and breaking the integral into two parts. Thus,

$$\begin{aligned} \mathcal{J}_3 &= \frac{z_1 d}{K} \left[ \int_0^{\pi/2} \frac{d\sigma}{\sqrt{1 - K^2 \sin^2 \sigma}} - \int_0^{\pi/2} \sqrt{1 - K^2 \sin^2 \sigma} d\sigma \right] \\ &= \frac{z_1 d}{K} \left[ F\left(\frac{\pi}{2}, K\right) - E\left(\frac{\pi}{2}, K\right) \right] = \frac{z_1 d}{K} \phi_e(K) \end{aligned} \quad (2.53)$$

where

$$K^2 = \frac{d^2}{d^2 + z_1^2} \quad (2.54)$$

$F\left(\frac{\pi}{2}, K\right)$  and  $E\left(\frac{\pi}{2}, K\right)$  represent the complete elliptic integrals of the first and second kind, and  $\phi_e(K)$  denotes the difference between the two elliptic functions.

Taking the separate integrals given in (2.49), (2.52), and (2.53), Equation (2.48) can be written now as

$$\frac{\pi I_{f\lambda}}{2f\mu B} = \frac{\pi a z_1 d^3}{16} + \frac{\pi b z_1^3}{6d} \left[ 1 + \frac{3}{2} \left( \frac{d}{z_1} \right)^2 + \left( \frac{d}{z_1} \right)^3 - \left( 1 + \frac{d^2}{z_1^2} \right)^{3/2} \right] + \frac{z_1}{K} \phi_e(K) \quad (2.55)$$

This describes the reflected intensity of the spectral emission from the cylindrical volume above the xy plane in Fig. 2.5. Integration over the volume below the xy plane gives an expression identical to (2.55) if we replace  $z_1$  by  $z_2$ . The total intensity is the sum of the two volume integrals. In writing the final expression for  $I_{f\lambda}$ , it will be convenient to introduce the parameters  $\xi = z_1/L$  and  $\delta = d/L$ , where  $L$  denotes the total length of the cylinder. Introducing these parameters in (2.55) (note that  $z_2/L = 1 - \xi$ ), we get for the sum of the two volume integrals

$$\frac{I_{f\lambda}}{B_\lambda} = 2f\mu \left[ \frac{ad^3L}{16} + \frac{bL^2}{6\delta} \left\{ 1 - 3\xi(1-\xi) + \delta^2 \left( \frac{3}{2} + 2\delta \right) - (\xi^2 + \delta^2)^{3/2} - [(1-\xi)^2 + \delta^2]^{3/2} \right\} \right. \\ \left. + \frac{1}{\pi} \left\{ \frac{\xi}{K_1} \phi_e(K_1) + \frac{1-\xi}{K_2} \phi(K_2) \right\} \right] \quad (2.56)$$

Since  $a$  and  $b$  as given by (2.41) and (2.42) depend only on  $\mu$  for a specified geometry, the bracketed member of (2.56) can be regarded as a function of  $\mu$ . Thus, if we denote the bracketed factor by  $\Phi_2(\mu)$ , (2.56) becomes

$$\frac{I_{f\lambda}}{B_\lambda} = 2f\mu\Phi_2(\mu) \quad (2.57)$$

With  $I_{f\lambda}$  established, we can now write the final expressions for the observed radiation and the measured emissivity. Using (2.67) in (2.31), the spectral radiation emanating from the chamber during the combustion process is

$$\frac{dq_\lambda}{d\lambda} = \pi B_\lambda \left[ \sin^2 \alpha - \{ 1 - 2f\mu\Phi_2(\mu) \} \phi_i(\mu) \right] \quad (2.58)$$

Now if the background surface is replaced by a blackbody, the detector will observe black radiation through a solid angle identical with that observed during the combustion process, i.e., through the solid angle  $\Omega$ . The spectral intensity observed in this angle is

$$\frac{dq_{b\lambda}}{d\lambda} = \pi B_\lambda \sin^2 \alpha \quad (2.59)$$

This follows directly from (2.27) or (2.31) by taking  $f = 0$  since no absorbing medium is present, and  $I_{f\lambda} = B_\lambda$  since the background source is black. When the temperature of the blackbody is equal to the temperature of the gas, the observed emissivity is the ratio of the gas emission given by (2.58) to the blackbody emission given by (2.59). Thus,

$$\epsilon_{m\lambda} = 1 - [1 - 2f\mu\phi_2(\mu)] \frac{\phi_1(\mu)}{\sin^2 \alpha} \quad (2.60)$$

Up to this point, we have considered only the flux that strikes the center of the receiver. Except for a narrow region near the outer edge of the cone of view, the radiant flux is essentially constant over  $A$ . Assuming the flux to be constant, the total energy per unit time received by the thermopile from the gas is the product of the receiver area and the integral of (2.58) over-all wavelengths; that is,

$$q_m = \pi A \int_0^\infty B_\lambda [\sin^2 \alpha - \{1 - 2f\mu\phi_2(\mu)\}\phi_1(\mu)] d\lambda \quad (2.61)$$

Similarly, the total emission from the blackbody is

$$q_{mb} = \pi A \int_0^\infty B_\lambda \sin^2 \alpha d\lambda \quad (2.62)$$

and the total measured emissivity is the ratio  $q_m/q_{mb}$ , or

$$\epsilon_m = 1 - \frac{\int_0^\infty [1 - 2f\mu\phi_2(\mu)]B_\lambda\phi_1(\mu)d\lambda}{\sin^2\alpha \int_0^\infty B_\lambda d\lambda} \quad (2.63)$$

True Emissivity. Most of the available emissivity data has been correlated in terms of the total rather than the spectral emissivity and as a rule applies only to the unidirectional radiation emitted by an unenclosed gas. Any emission or reflection that is present because of a boundary surface is treated as a separate problem. Thus, in order to compare the experimental data obtained here with published data, it will be necessary to determine the emissivity of the gas itself, that is, apart from the effects of the enclosure.

The true emissivity of the gas can be determined only if we know the value of the absorption coefficient  $\mu$  for each wavelength. The value of  $\mu$  can be obtained from Eq. (2.60) since  $\epsilon_{m\lambda}$  is a known function of  $\lambda$ , but unfortunately only by trial-and-error methods. However, once  $\mu$  is determined, the emissivity of the gas alone can be derived from (2.60) and (2.63) by setting  $f = 0$ . Thus, if we denote the spectral and total emissivities respectively by  $\epsilon_\lambda$  and  $\epsilon$ , we get

$$\epsilon_\lambda = 1 - \frac{\phi_1(\mu)}{\sin^2\alpha} \quad (2.64)$$

and

$$\epsilon = 1 - \frac{\int_0^\infty B_\lambda \phi_1(\mu) d\lambda}{\sin^2\alpha \int_0^\infty B_\lambda d\lambda} \quad (2.65)$$

If  $\alpha$  is small, negligible error will be introduced if we replace  $\phi_1(\mu)$  by the approximate value (2.34)

$$\phi_1(\mu) \simeq \sin^2 \alpha e^{-\mu d}$$

Thus,

$$\epsilon_\lambda \simeq 1 - e^{-\mu d} \quad (2.66)$$

and

$$\epsilon \simeq 1 - \frac{\int_0^\infty B_\lambda e^{-\mu d} d\lambda}{\int_0^\infty B_\lambda d\lambda} \quad (2.67)$$

Effective Beam Length. It is clear from the foregoing discussion that in order to calculate the radiation emitted from an arbitrary gas volume, we must know how the absorption coefficient  $\mu$  (often called the decrement of radiation) varies with wavelength. As pointed out earlier, Eq. (2.60) can be solved for  $\mu$  but only

by numerical methods. This is impractical when  $\mu$  is needed for a large number of wavelengths. An approximate relationship can be derived which will provide essentially the same results as those obtained from Eq. (2.60). To do this, we make use of a so-called effective optical depth.

For one-dimensional radiation, the optical depth is defined as the product of the decrement  $\mu$  and the depth  $d$  of the radiation mass. The product  $\mu d$  is dimensionless. The concept of the optical depth is also applied to three-dimensional radiation, but in this case the actual linear depth is replaced by a characteristic length. For gas mixtures, the characteristic length is customarily taken to be the radius of a hemispherical volume that radiates to a unit area at the center of the base with an intensity equal to the average value emitted at the surface of the actual gas body. The radius of the hemisphere is referred to as the effective beam length.

An effective beam length for the chamber used in present experiments is derived as follows: Let  $d_e$  denote the effective beam length, and consider a hemisphere of radius  $d_e$  centered over the unit area  $dA_1$ . The radiant flux received by  $dA_1$  from the gas in the enclosure, over the wavelength interval  $(\lambda, \lambda + d\lambda)$ , is

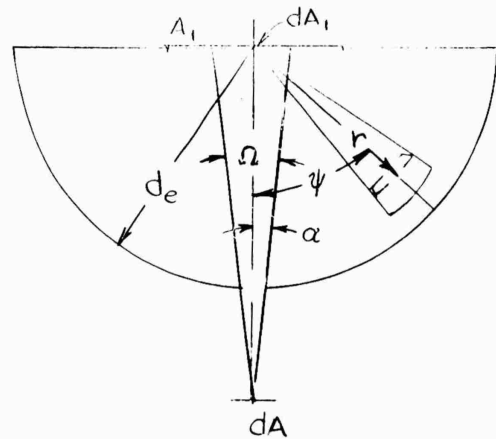


Fig. 2.7. Effective Beam Length

according to Eq. (2.13)

$$\begin{aligned}\frac{dq_{1\lambda}}{d\lambda} &= 2\pi\mu B_\lambda \int_0^{\pi/2} \int_0^{d_e} e^{-\mu r} \sin\psi \cos\psi dr d\psi \\ &= \pi B_\lambda (1 - e^{-\mu d_e})\end{aligned}\quad (2.68)$$

If the surface  $A_1$  is observed by the unit area  $dA$  through a small opening in the enclosure, the intensity of the radiation reflected from  $A_1$  is

$$I_{f\lambda} = f B_\lambda (1 - e^{-\mu d_e}) \quad (2.69)$$

The element  $dA$  will receive part of this radiation plus an additional contribution due to the emission from the gas in the solid angle  $\Omega$ . If we apply Eq. (2.33) now, and take  $d = d_e$ , the total flux received by  $dA$  can be expressed as

$$\frac{dd_\lambda}{d\lambda} = \pi B_\lambda \sin^2\alpha (1 - e^{-\mu d_e})(1 + f e^{-\mu d_e}) \quad (2.70)$$

According to Eq. (2.59),  $\pi E_\lambda \sin^2\alpha$  is the radiant flux received from the blackbody. Hence, the measured emissivity is

$$\epsilon_{m\lambda} = (1 - e^{-\mu d_e})(1 + f e^{-\mu d_e}) \quad (2.71)$$

The question now is whether or not a single value of  $d_e$  exists such that (2.71) will hold for all  $\mu$  and  $f$ . If this is true, (2.71) can be solved explicitly

for  $\mu$ , and thus will provide a much simpler relationship for determining than the more rigorous expression given by Eq. (2.60).

It will be noted now that Eq. (2.71) is identical to Eq. (2.60) when  $f = 0$ , and  $d_e = d$ . If  $f = 1$ , the value of  $d_e < d$ . To determine  $d_e$ , we will presume that if a suitable value for  $d_e$  can be determined for  $f = 1$ , the same value will also apply for  $f < 1$ . For  $f = 1$ , it is found that the two equations give substantially the same results if an effective beam length of  $d_e = 0.97d$  is used in (2.71). The discrepancy is less than 2.5% for  $.005 \leq \mu \leq .2$ . A comparison of  $\epsilon_{m\lambda}$  calculated from the two equations is presented in Table 4 below.

Table 4

Calculated Values of  $\epsilon_{m\lambda}$  from Eqs. (2.60) and (2.71)  
for  $f = 1$ , and  $d_e = 4.29$  in.,  $d = 4.42$  in.

$\mu$	$**2f\mu\phi_2(\mu)e^{-\mu d}$	$\epsilon_{m\lambda}$ Eq. (2.60)	$\epsilon_{m\lambda}$ Eq. (2.71)
.005	.0202	.0421	.0420
.01	.0391	.0823	.0823
.02	.0732	.1578	.1577
.04	.1285	.2905	.2905
.06	.1698	.4028	.4024
.08	.2004	.4982	.4966
.1	.2224	.5796	.5760
.2	.2579	.8448	.8202
.4	.1990	1.028 *	.9677
.6	.1219	1.051 *	.9942
.8	.0670	1.038 *	.9990
1.0	.0346	1.023 *	.9998
1.5	.0057	1.004 *	1.000
2.0	.0008	1.000 *	1.000

\*\* $\phi_1(\mu)/\sin^2\alpha$  differs from  $e^{-\mu d}$  by less than 0.5%.

\*Since  $\epsilon_{m\lambda}$  cannot exceed unity, the designated values are obviously incorrect. The reason for this is due to the fact that the approximation of  $e^{-\mu f}$  by a cubic function is poor when  $\mu$  is large. The values given by Eq. (2.71) are more reliable in this range.

Excellent agreement is obtained for values of  $.005 \leq \mu \leq .2$ . The values of  $\phi_2(\mu)$  are unreliable for  $\mu > 0.3$ . The reason for this is that the approximation of  $e^{-\mu r}$  by means of a cubic function (2.39) is poor when  $r$  is large. In view of the close agreement obtained for the small values of  $\mu$ , we can expect the values of  $\epsilon_m$  given by (2.71) to be equally satisfactory for the large values of  $\mu$ . Consequently, in determining the values of  $\mu$  from the measured emissivities we will utilize only Eq. (2.71).

The spectral absorption coefficient as a rule cannot be expressed as an integrable function of wavelength. As a result, approximate emissivity calculations from molecular theory or from spectroscopic data are commonly based on an integrated absorption coefficient that applies to a narrow wavelength interval. If the wavelength interval  $\Delta\lambda$  pertains to a single band of emission,  $\Delta\lambda$  is called the effective band width. The corresponding effective absorption coefficient ( $\bar{\mu}$ ) for this band is defined in terms of the integrated emission by

$$\epsilon_{\Delta\lambda} = (1 - e^{-\bar{\mu}\Delta\lambda}) \int_{\Delta\lambda} \frac{\pi B_\lambda d\lambda}{\sigma T^4} \quad (2.72)$$

This follows directly from Eq. (2.67) by integrating over  $\Delta\lambda$  rather than over all wavelengths in the numerator of the integral term. The denominator reduced directly to  $\sigma T^4/\pi$ , where  $\sigma$  is the Stefan-Boltzmann constant.

Now for practical purposes it is convenient also to define an effective absorption coefficient for the total radiation (i.e., for all wavelengths). In this case, Eq. (2.67) applies without modification. However, according to the results shown above in Table 4, little error will result if  $d$  is replaced by  $d_e$ . If the integration in Eq. (2.67) is carried out over all wavelengths now, the integral term reduces to unity, and the absorption coefficient can be expressed in terms of

the total emissivity as

$$\epsilon \approx 1 - e^{-\bar{\mu} d_e} \quad (2.73)$$

## COMBUSTION TEMPERATURE

Thermodynamic Temperature. A direct measurement of the combustion temperature was not possible with the present experimental apparatus. The temperatures used in this study for correlating the radiation data were obtained from measured performance variables by applying nozzle flow theory. The relationships necessary for this calculation are derived in the following discussion.

The measured variables consist of the chamber pressure,  $p_c$ , the mass flow rate,  $m$ , the nozzle dimensions, and the heat transferred to the coolant. The most convenient arrangement of these variables for calculating the temperature is the parameter called the characteristic velocity. This parameter, perhaps better known as  $C^*$ , is defined as

$$C^* = \frac{p_c A_t g}{m} \quad (3.1)$$

where  $A_t$  is the cross-sectional area of the throat. An important aspect of  $C^*$  is that it is not influenced strongly by the geometry of the nozzle. In fact, for one-dimensional, isentropic flow of a perfect gas,  $C^*$  depends on only the specific heat ratio, the molecular weight, and the temperature of the gas at the nozzle entrance. Thus, if the flow in the nozzle approaches that of an ideal fluid, the temperature can be calculated directly from the isentropic relationship for  $C^*$  (14).

Temperatures that were calculated on the basis of ideal flow theory proved to be unsatisfactory for the present experimental work. The flow achieved in the nozzle was far from isentropic. In fact, the measured values of  $C^*$  were rarely greater than 95 per cent of the theoretical values. The departure from isentropic expansion was due for the most part to the high heat transfer rates

in the nozzle. Total heat transfer rates of the order of 100 B/lb were necessary to provide adequate cooling for the walls. A heat loss of this magnitude amounts to only a small fraction of the total energy of the flowing gas, but it has a significant effect on  $C^*$  and cannot be ignored. As will be shown later, the use of isentropic theory can result in an error of as much as five per cent in calculating  $T_c$  from  $C^*$ .

To account for the effect of heat transfer on  $C^*$ , consider the basic flow arrangement illustrated in Fig. 3.1. Location C in the figure represents the line of sight through the radiation observation aperture. Each symbol shown in the figure represents a measured quantity.

$M_p$  denotes the mass flow rate of the primary propellants, which consists of the sum of oxidizer and fuel flow rates.

$M_g$  represents the small flow of cold gas that was forced through the aperture to prevent the combustion gases from flowing out. The total flow through the nozzle, designated by  $m$ , is the sum of propellant flow and the gas flow. Heat leaves the fluid in the chamber at the rate of  $Q_c$  B/sec, and in the nozzle at the rate of  $Q$  B/sec. The pressure of the gas in the chamber was measured at a point slightly upstream from C. This is not precisely the pressure at C, but the pressure drop between the pressure tap and the aperture should be insignificant. Thus, for all practical purposes the pressure at C can be taken as  $p_c$ .

The state of the combustion gas changes slightly as the flow passes station

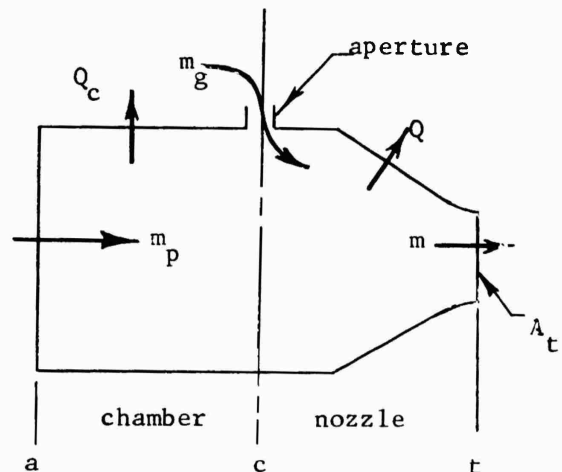


Fig. 3.1 Measured Variables

C. The cold gas that is injected through the aperture reduces the temperature and alters the composition of the products as it mixes with the main stream. The mixing and reaction processes that actually take place downstream from the aperture cannot be described accurately. However, the nozzle entrance section is considered to be long enough so that complete mixing probably occurs before the gas reaches the convergent section. Under these conditions, little error will appear in  $C^*$  if it is assumed that the composition of the combustion gas changes abruptly at station C, but remains constant from there to the nozzle throat. Although the temperature and the pressure of the gas both decrease as the gas expands through the convergent section, the change is not large enough to cause a significant effect on the composition and specific heat of the gas. Thus, for the following derivation, we will take the state of the products at station C to be the equilibrium state produced by the reaction of  $M_p$  lb of propellants with  $M_g$  lb of aperture gas. It will be assumed further that there are no pressure losses resulting from friction or from mixing during the expansion process, but that there is heat flow from the gas. In other words, the flow is internally reversible and diabatic, with a frozen composition.

To express  $C^*$  in terms of  $T_c$  and the heat transfer now, we start with the definition of  $C^*$  given in Eq. 3.1. The most convenient approach is first to express the factor  $A_t/m$  as a function of the throat temperature,  $T_t$ , and then to relate  $T_t$  to  $T_c$ . The relationship between  $C^*$  and the throat conditions is obtained readily from the continuity equation,

$$m = pAV \quad (3.2)$$

the perfect gas law,

$$p = \rho RT \quad (3.3)$$

and the fact that the velocity of the gas at the throat is equal to the sonic velocity, which for a perfect gas is given by

$$V_t^2 = A_t^2 = \rho g R T_t \quad (3.4)$$

The symbols  $\rho$ ,  $A$ ,  $V$ , and  $T$  denote respectively the local density, cross-sectional area, velocity, and temperature of the gas,  $R$  represents the specific gas constant, and  $k$  is specific heat ratio. If Eqs. 3.2, 3.3, and 3.4 are expressed in terms of the throat variables and are combined to eliminate  $\rho_t$  and  $V_t$ , there results

$$\frac{A_t}{m} = \frac{1}{\rho_t} \sqrt{\frac{R T_t}{k}} \quad (3.5)$$

Substituting this value of  $A_t/m$  into Eq. 3.1 gives for the characteristic velocity

$$C^* = \frac{p_c}{p_t} \sqrt{\frac{g R T_t}{k}} \quad (3.6)$$

or in terms of logarithms

$$\log C^* = \log \frac{p_c}{p_t} + \frac{1}{2} \log \frac{g R T_c}{k} \quad (3.7)$$

The next step is to express the pressure ratio  $p_c/p_t$  and  $T_t$  as a function of  $T_c$  and the heat transfer rate  $Q$ . This is accomplished by making use of the first law of thermodynamics as follows: Consider a differential length  $dx$  at any location  $x$  along the nozzle, as shown in

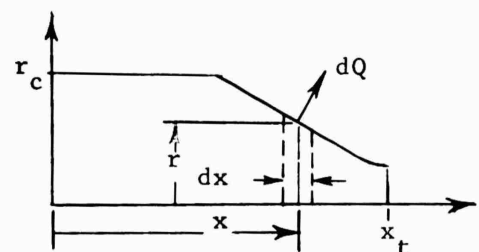


Fig. 3.2 Application of First Law

Fig. 3.2. The change of state that occurs across dx is defined according to the first law as

$$- dQ = dh - \frac{vdp}{J} \quad (3.8)$$

in which  $dQ$  represents the quantity of heat removed from a unit mass of the gas, and  $h$ ,  $v$ , and  $p$ , denote respectively the specific enthalpy, specific volume, and pressure of the gas at  $x$ . The negative sign in front of  $dQ$  is employed strictly as a matter of convenience so that the heat extracted from the gas can be regarded as a positive quantity.

Since the state of the gas is assumed to follow the perfect gas law, Eq. 3.8 can be arranged in the form

$$- \frac{dQ}{T} = C_p \frac{dT}{T} - \frac{R}{J} \frac{dp}{p} \quad (3.9)$$

Integration of this expression between the limits  $T_c$  to  $T_t$  yields

$$\frac{R}{J} \log \frac{p_c}{p_t} = - C_p \log \frac{T_t}{T_c} - \int_{T_c}^{T_t} \frac{dQ}{T} \quad (3.10)$$

which is the well-known relationship for the entropy change of a perfect gas.

The temperature ratio in Eq. 10 can be put in terms of  $T_c$  and  $Q$  now by applying the integral form of the energy equation. Thus

$$- \frac{Q}{m} = \Delta h + \Delta \frac{v^2}{2qJ} \quad (3.11)$$

If the kinetic energy of the gas at the nozzle entrance is neglected and  $h$  is expressed in terms of the temperature and the specific heat, it follows that

$$v_t^2 = 2gJ \left[ C_p (T_c - T_t) - \frac{Q}{m} \right] \quad (3.12)$$

An equation containing  $T_t$  as the only unknown variable can be obtained now by replacing  $v_t$  by its equivalent from Eq 3.4. If use is then made of the fact that

$$C_p = \frac{R}{J} \frac{k}{k-1} \quad (3.13)$$

the solution of Eq.3.12 for the temperature ratio is

$$\tau_r = \frac{T_t}{T_c} = \frac{2}{k+1} \left( 1 - \frac{k-1}{k} \frac{JQ}{mRT_c} \right) \quad (3.14)$$

The above results, combined with Eq.3.10, provide the necessary relationships for eliminating  $p_c/p_t$ ,  $C_p$ , and  $T_t$  from Eq. 7. On making these substitutions, the characteristic velocity becomes

$$\log C^* = \frac{1}{2} \log \left( \frac{gRT_c}{k} \right) \left( \frac{k+1}{2} \right)^{\frac{k+1}{k-1}} - \frac{k+1}{2(k-1)} \log \left( 1 - \frac{k-1}{k} \frac{JQ}{mRT_c} \right) - \frac{J}{R} \int_{T_c}^{T_t} \frac{dQ}{T} \quad (3.15)$$

A more compact form of this equation can be obtained by noting that when  $Q = 0$ , the last two terms of the right-hand number are zero, and the first term is the conventional isentropic value for  $C^*$ . Hence, Eq.3.15 can be rearranged conveniently in terms of the ratio of  $C^*$  to the isentropic value,  $C_i^*$ . If the integral term is denoted by  $\Delta S$ , the result is

$$\log \frac{C^*}{C_i^*} = - \frac{k+1}{2(k-1)} \log \left( 1 - \frac{k-1}{k} \frac{JQ}{mRT_c} \right) + \frac{J}{R} \Delta S \quad (3.16)$$

At this point, the only unknown factor is the entropy change  $\Delta S$  due to the external heat transfer. The value of  $\Delta S$  depends upon the behavior of the heat

transfer and the temperature functions along the length of the nozzle. According to Eq. 15, integration of the entropy function can be accomplished merely by expressing  $Q$  as a function of  $T$ . However,  $Q$  is not a unique function of  $T$  alone. In fact, the heat flow in rocket nozzles depends more on external factors, such as wall thicknesses and nozzle geometry, than it does on the temperature. A rigorous description of the heat flux distribution in rocket nozzles is extremely involved, and as a rule, does not provide  $Q$  as an explicit function of the nozzle variables. Moreover,  $T$  cannot even be defined explicitly in terms of the nozzle dimensions when heat transfer is present. A rigorous analysis is not essential, however, for determining  $\Delta S$ . As will be shown later, when  $Q$  is a small part of the total energy of the fluid stream, the entropy change is governed primarily by the total quantity of heat removed and is not excessively sensitive to the path followed as the gas changes state. Any reasonably close approximation to the actual state path will provide an acceptable evaluation of the integral term.

The general characteristics of the heat transfer and temperature functions can be illustrated from first principles. According to established theory, the heat flux from a gas flowing at high Mach numbers depends on the difference between the stagnation temperature of the gas and temperature of the wall. The local heat transfer coefficient can be approximated satisfactorily from the conventional Nusselt type correlation. If the Prandtl number is assumed to be constant, the Nusselt number becomes a function of the Reynolds number only, and the heat transfer coefficient can be written as

$$\frac{H}{H_c} = \left( \frac{r}{r_c} \right)^{1.8} \quad (17)$$

where  $r_c$  is the radius and  $H_c$  is the heat transfer coefficient at the nozzle inlet.

For flow at Mach numbers less than unity, the stagnation temperature is essentially equal to the total temperature. Moreover, with the usual nozzle design, the wall temperature does not vary significantly in the convergent region. Thus the temperature potential is essentially a constant, and the heat flux which is given by

$$q = H(T_s - T_w)$$

can be expressed as

$$\frac{q}{q_c} \approx \frac{H}{H_c} \quad (3.18)$$

Referring to Eq.3.17 now, it follows that

$$\frac{q}{q_c} \approx \left(\frac{r_c}{r}\right)^{1.8} \quad (3.19)$$

Application of Eq.3.19 and the definition of the heat flux leads to

$$\frac{dQ}{dx} = \frac{2\pi r q}{m} \approx \frac{2\pi r_c q_c}{m} \left(\frac{r_c}{r}\right)^{1.8} \quad (3.20)$$

The heat flux  $q_c$  at the nozzle entrance does not differ greatly from the average value in the chamber. Thus, we can assume that

$$2\pi r_c q_c \approx \frac{Q_c}{L} \quad (3.21)$$

For the purpose of this analysis, the nozzle employed in the experiments

can be considered to be a cylinder joined to a truncated cone as shown in Fig.3.3. The heat transfer rate per unit length in the cylindrical section is essentially constant, but  $dQ/dx$  will usually vary with  $x$  in the convergent section. The general form of  $dQ/dx$  can be derived by noting that the radius for any assigned  $x$  between  $e$  and  $t$  is equal to

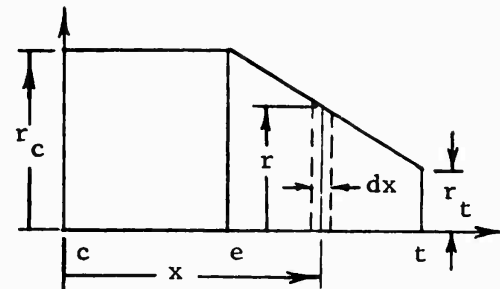


Fig. 3.3 Geometry Assumed for Heat Transfer

$$r = r_c (1 - a_1 x) \quad (3.22)$$

where  $a_1$  is a constant, and  $a_1 x$  is less than unity. Using this value of  $r$  in Eq.3.21 gives

$$\frac{dQ}{dx} \approx \frac{2\pi r_c q_c}{m(1-a_1 x) \cdot 8} \quad (3.23)$$

This equation cannot be used as it stands because it will not provide the correct total heat rate. However, it does indicate the general behavior of  $dQ/dx$ . The important characteristics evident from Eq.3.23 are that  $dQ/dx$  and the derivative of  $dQ/dx$  both increase as  $x$  increases.

A general form for the temperature function cannot be derived from fundamental principles. Integration of the well-known differential equations for isentropic flow (15) yields a relationship for the cross-sectional area of the nozzle (or the radius) in terms of the temperature, but it cannot be solved explicitly for the temperature. Nevertheless, isentropic theory does allow one to predict the general behavior of the temperature function. It is not

difficult to show that the derivative of the temperature  $dT/dx$  is negative and that it decreases continuously with  $x$  in the convergent portion of the nozzle.

Inasmuch as the heat flow and temperature functions cannot be integrated easily by a direct combination of  $dQ$  and  $T$ , it will be convenient to develop empirical relationships for  $dQ/dx$  and  $T$  which satisfy appropriate boundary conditions. The general characteristics of Eq.3.3 and the temperature functions are illustrated in Fig.3.4. Each of these curves can be approximated closely by exponential functions that will permit integration of the entropy term.

Since the heat transfer curve has a positive first and second derivative,  $dQ/dx$  can be approximated by a function of the form

$$\frac{dQ}{dx} = a + be^{cx} \quad (3.24)$$

where  $a$ ,  $b$ , and  $c$  are positive constants. In order to define the constants, Eq.3.24 must satisfy three independent conditions. Two of these conditions can be obtained by specifying the heat

transfer rates at two locations in the nozzle. The most convenient locations for this purpose are the entrance and the throat. The third

and most important condition is that the total heat transfer predicted by

Eq.3.24 must be equal to the measured value. Hence, if we first take  $x = 0$ , and then  $x = x_t$  we find that

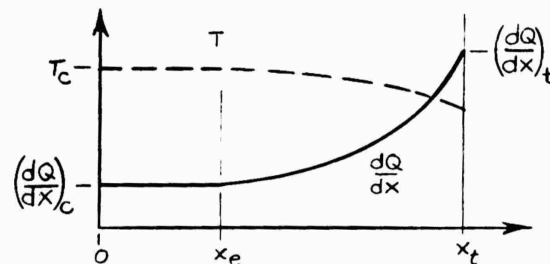


Fig.3.4 Heat Flow and Temperature Functions

$$\left(\frac{dQ}{dx}\right)_c = a + b = \frac{2\pi r q_c}{m} \quad (3.25)$$

and

$$\left( \frac{dQ}{dx} \right)_t = a + be^{\beta} = \frac{2\pi r_t q_t}{m} \quad (3.26)$$

where

$$\beta = cx_t \quad (3.27)$$

The third condition is obtained from Eq.3.24 by multiplying both members by  $dx$  and by integrating the result from 0 to  $x_t$ . Thus,

$$\begin{aligned} \frac{Q}{m} &= \int_0^{x_t} dQ = \int_0^{x_t} (a + be^{cx}) dx \\ &= ax_t + \frac{b}{c} (e^{\beta} - 1) \end{aligned} \quad (3.28)$$

These equations cannot be solved explicitly for the constants. Equation 3.25 gives  $b$  in terms of  $a$ ; the use of this in Eq.3.26 yields  $a$  as a function of  $c$ ; and the application of both results to Eq.3.28 yields a single equation in  $c$ .

The final result of these substitutions is

$$\frac{1}{\beta} - \frac{1}{e^{\beta} - 1} = \frac{Q_f}{R_f} \quad (3.29)$$

where

$$R_f = \left( \frac{r_c}{r_t} \right)^{.8} - 1 \quad (3.30)$$

and

$$Q_f = \frac{QL}{Q_c x_t} - 1 \quad (3.31)$$

The final equation for  $C^*$  will be written in terms of the single constant  $\beta$ .

Hence, it will not be necessary to define each of the constants  $a$ ,  $b$ , and  $c$  in terms of the independent variables.

Let us return now to the problem of fitting the temperature curve. Since the first and second derivatives of  $T$  with respect to  $x$  must be negative, the general form of  $T$  can be approximated by a function of the type

$$T = A - Be^{cx} \quad (3.32)$$

where  $A$  and  $B$  are to be determined from the initial and final temperatures and  $c$  is the same constant that appears in Eq. 3.24. The constant  $c$  is employed here merely to simplify the integration. To evaluate the constants, we take  $T = T_c$  when  $x = 0$  and  $T = T_t$  when  $x = x_t$ . This provides two equations which can be solved for  $A$  and  $B$ . Thus,

$$A = T_c + \frac{T_c - T_t}{e^\beta - 1} \quad (3.33)$$

$$B = A - T_c \quad (3.34)$$

With the constants defined now,  $dQ/T$  can be evaluated by means of Eqs 3.34 and 3.32, and the integral term becomes

$$\begin{aligned} \int_{T_c}^{T_t} \frac{dQ}{T} &= \int_0^{x_t} \frac{a + be^{cx}}{A - Be^{cx}} dx \\ &= \frac{ax_t}{A} - \frac{1}{c} \left( \frac{a}{A} + \frac{b}{B} \right) \log T_r \end{aligned} \quad (3.35)$$

If the constants  $a$ ,  $b$ ,  $c$ ,  $A$ , and  $B$  are eliminated by means of Eqs. 3.25, 3.26, 3.29, 3.33, and 3.34, the result is

$$\frac{J}{R} \int_{T_c}^{T_f} \frac{t \frac{dQ}{dT}}{T} = \frac{JQ}{mRT_c(1+Q_f)(1-T_r)} \left[ \frac{(R_f + 1 - T_r)(\beta - \log T_r)}{\beta + (1 - T_r)(1 - \beta \frac{Q_f}{R_f})} - R_f \right] \quad (3.37)$$

where  $T_r$ ,  $\beta$ ,  $R_f$ , and  $Q_f$  are obtained respectively from Eqs. 3.14, 3.29, 3.30 and 3.32.

The final relationship for  $C^*$  can now be written in terms of  $Q$  and  $T_c$  from Eq. 3.16 as

$$\log \frac{C^*}{C_i^*} = - \frac{k+1}{2(k-1)} \log \frac{k+1}{2} T_r - \frac{JQ}{mRT_c(1-T_r)(1+Q_f)} \left[ \frac{(1-T_r+R_f)(\beta - \log T_r)}{\beta + (1-T_r)(1-\beta \frac{Q_f}{R_f})} - R_f \right] \quad (3.38)$$

where

$$T_r = \frac{2}{k+1} \left( 1 - \frac{k-1}{k} \frac{JQ}{mRT_c} \right)$$

Approximate State Paths. It will be of interest now to compare the value of the entropy term given by Eq. (3.37) with that obtained from several less exact but much simpler approximations.

Example 1. Linear Path

As a first example, let us assume that the change of state between the chamber and the throat follows a linear path as shown by

the dashed line in Fig. 3.5 between

points 1 and 2. Since the area under the curve 1 - 2 must equal  $Q$ , and slight departures from the straight line path will have only a small effect on the total area under the curve, a linear path should provide a reasonably close approximation for evaluating  $\Delta S$ . Since

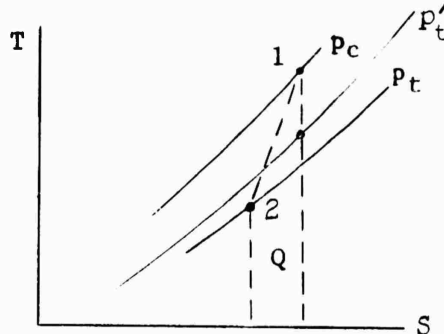


Fig. 3.5 Approximate Path

$$-\frac{Q}{m} = \frac{T_c + T_t}{2} \Delta S$$

$$-\frac{J}{R} \int_{T_c}^{T_t} \frac{dT}{T} dQ = \frac{J}{R} \Delta S = -\frac{2JQ}{mR(T_c + T_t)} = \frac{2JQ}{mRT_c(1 + T_r)} \quad (3.39)$$

Example 2.

As another example, suppose we assume that the heat transfer rate is constant in the nozzle, while the temperature of the gas varies linearly with  $x$  from  $T_c$  to  $T_t$ . On this basis

$$T = T_c \left[ 1 - (1 - T_r) \frac{x}{x_t} \right]$$

and

$$\frac{dQ}{dx} = A = \text{constant}$$

Since

$$-\frac{Q}{m} = \int_0^{x_t} dQ = \int_0^{x_t} Adx$$

$$A = \frac{-Q}{mx_t}$$

The entropy term can be integrated now in terms of  $x$ . Thus,

$$\frac{J}{R} \int_{T_c}^T \frac{t_dQ}{T} = \frac{J}{RT_c} \int_0^{x_t} \frac{Adx}{1 - (1-T_r) \frac{x}{x_t}} = -\frac{JQ}{mRT_c} \frac{\log T_r}{1 - T_r} \quad (3.40)$$

Example 3.

In order to examine the effect of a poor temperature fit, assume that the heat transfer rate is constant as in Example 2, but let the temperature vary with a negative but increasing slope according to

$$T = T_c e^{-ax}$$

where

$$ax_t = -\log T_r$$

With these assumptions

$$\begin{aligned}
 \frac{J}{R} \int_{T_c}^{T_t} \frac{dQ}{T} &= \frac{JQ}{Rmxt} \int_0^{x_t} \frac{dx}{T_c e^{-ax}} = \frac{JQ}{aRmT_c x_t} [e^{ax}]_0^{x_t} \\
 &= -\frac{JQ (1-T_r)}{mRT_c T_r \log T_r} \quad (3.41)
 \end{aligned}$$

**Example 4.**

As a final example, suppose that the change of state follows the path defined by

$$pv^n = \text{constant}, n \neq k$$

It is not difficult to show that

$$\begin{aligned}
 \frac{dp}{p} &= \frac{n}{n-1} \frac{dT}{T} \\
 -dQ &= \frac{R}{J} \left[ \frac{k}{k-1} - \frac{n}{n-1} \right] dT
 \end{aligned}$$

where

$$\frac{n}{n-1} = \frac{k}{k-1} - \frac{JQ}{mR(T_c - T_t)}$$

Thus,

$$\frac{J}{R} \int_{T_c}^{T_t} \frac{dQ}{T} = \frac{JQ}{mR(T_c - T_t)} \int_{T_c}^{T_t} \frac{dT}{T} = \frac{JQ \log T_r}{mRT_c (1-T_r)} \quad (42)$$

where

$$T_r = T_t/T_c$$

This is the same result obtained in Example 2, which assumed a constant heat flow per unit length and a linear temperature variation.

A comparison of the effect of the different paths is shown in the following table:

Table 5

Parameters for Calculating Combustion Temperature

$$\frac{J}{R} \int_{T_c}^T \frac{dt}{T} dQ \quad \text{for Different Values of } Q$$

Run	43	47	50	53
$Q \text{ B/sec}$	68.4	74.1	91.4	150.5
Eq.				
3.37	.1602	.1666	.1925	.2737
3.39	.1650	.1686	.1976	.2965
3.40	.1653	.1689	.1979	.2967
3.41	.1655	.1693	.1981	.2969
$T_c^o R$	.4560	.4652	.4855	.5491
$T_r$	.8750	.8540	.8854	.9121
O/F	2.11	1.63	1.66	1.28

Average Combustion Temperature. The combustion temperature can also be calculated from thermochemical theory. This approach provides the so-called equilibrium flame temperature. Since considerable heat is transferred from the gas to the combustion chamber wall, the temperature of the gas that reaches the aperture obviously must be less than the ideal value, but how much less is not easily predicted. A precise determination of the temperature distribution in the flow field, and the effect of the heat transfer on the average temperature at aperture cross section is virtually impossible for flow in rocket combustion chambers.

We can obtain an approximate value of the temperature at the aperture by assuming that the heat is extracted uniformly over the total cross section of the flow. Under these conditions, the gas temperature is given by

$$T_c = T'_c - \frac{Q}{m_p C_p} \quad (3.43)$$

where  $T'_c$  denotes the theoretical flame temperature.

Thus we have two methods for estimating the combustion, that is, by means of Eqs. (3.38) and (3.43). The combustion temperature was calculated by each method for each test run presented in Table 1. Excellent agreement was obtained for the  $\text{NH}_3$  propellant systems. In some instances the two methods predicted combustion temperatures that differed by no more than  $20^{\circ}\text{F}$ . The agreement was poor for the  $\text{N}_2\text{H}_4$  system. Equation (3.38) predicted values that appeared to be too high, while Eq. (3.43) gave values that seemed to be too low. Temperature differences of as much as  $400^{\circ}\text{F}$  occurred for some runs. The discrepancy was attributed to the very high heat transfer rates that occurred for the  $\text{N}_2\text{H}_4$  combination.

There was no apparent reason for assuming that one method is any more accurate than the other, average of the two values was taken to be the best approximation of the temperature of the gas in the vicinity of the aperture. The temperatures designated in Table 1 by  $T_c$  are average values that were obtained in this manner.

## CALIBRATION AND CORRECTIONS

Calibration. The spectrometer and the thermopile systems were calibrated with the laboratory blackbody at four different temperatures for each run. The calibration was made by attaching the blackbody to the opening in the chamber provided for the background surface (see Figs. 1.7 and 2.1). The temperature of the blackbody was measured by turning the blackbody away from the chamber opening and then viewing the interior cavity with a "precision" optical pyrometer. When a stable temperature was achieved, the temperature was first read with the pyrometer, next the blackbody was coupled immediately to the chamber opening, and a trace was then taken on the recorders for the thermopile and the spectrometer. The temperature of the black cavity was measured again. If the final temperature differed from the initial value by more than  $\pm 10^{\circ}\text{F}$  the calibration point was repeated.

Typical calibration curves for the spectrometer are presented in Fig. 4.1. The calibration shown applies to Run 50. The spectrometer trace produced by the combustion gas is also shown for the same run for comparison. It will be noted that the combustion temperature  $T_c$  falls almost precisely at the midpoint of the calibration temperature range ( $543^{\circ}\text{F}$ ), the maximum temperature being  $276^{\circ}\text{F}$  above and the minimum temperature being  $267^{\circ}\text{F}$  below  $T_c$ . A symmetrical calibration of this type was attempted for each run, but the attempts were not always successful. Nevertheless, the combustion temperature was always within the calibration range.

The calibration curve corresponding to the combustion temperature was obtained from the calibration curve by Lagrangian interpolation for chart-length intervals of 0.1 in. (this corresponds to each  $\lambda$  shown in Table 3). The measured intensity ratio (or measured "emissivity") at a specified wavelength is taken to be the

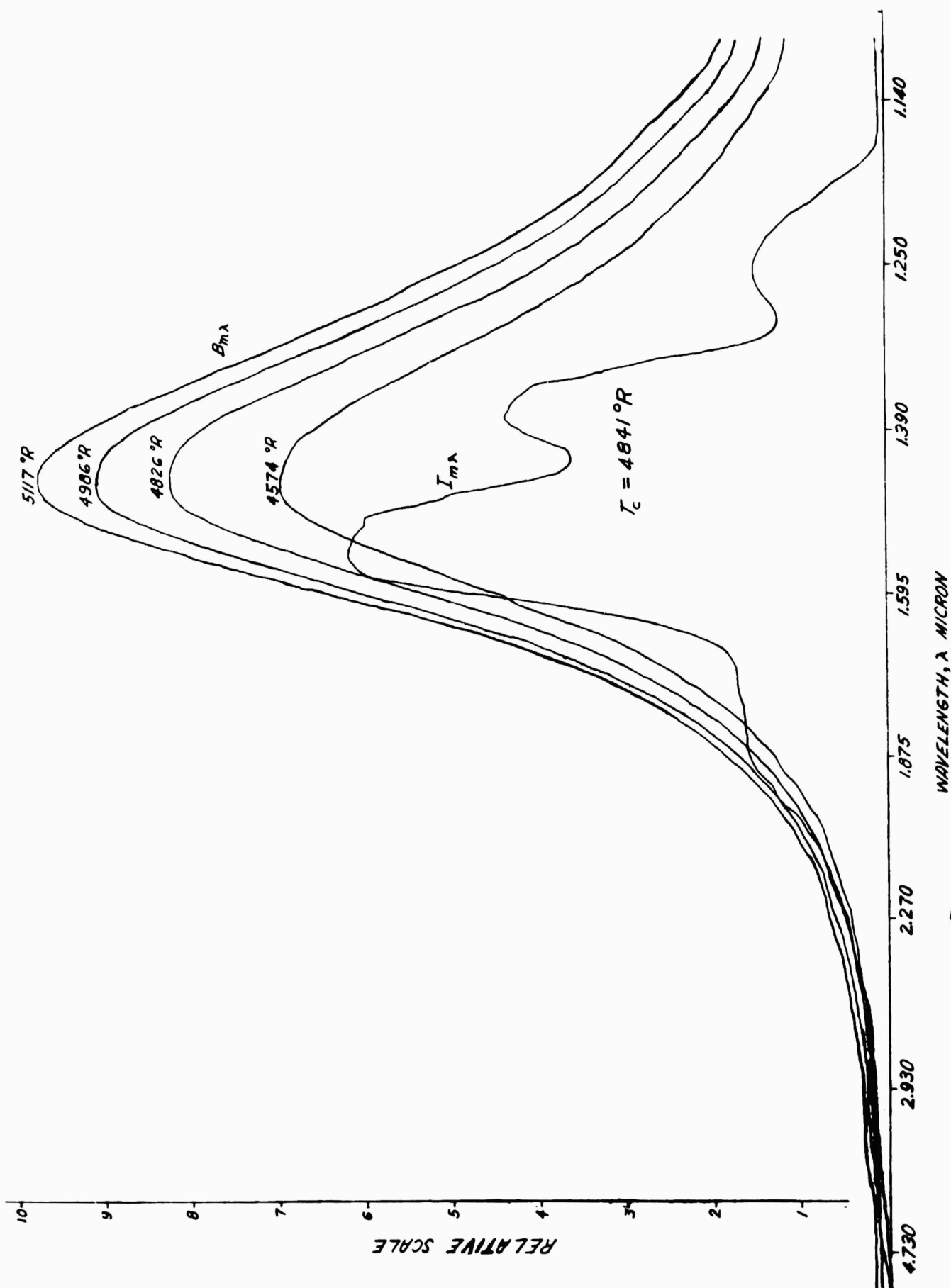


Fig. 4.1 Trace of Blackbody Calibration Curves and Gas Emission  
Obtained for Run 50

ratio of the ordinate of the gas emission trace in Fig. 4.1 to the ordinate of the interpolated calibration curve for  $T_c$ . It should be emphasized here that Fig. 4.1 shows only the relative intensity, and what appears to be maximum intensities on the trace may actually represent a comparatively low absolute intensity. The true absolute intensity is obtained by comparing the relative intensities with the theoretical absolute spectral intensity of black emission.

Calibration curves for the thermopile are shown in Fig. 4.2 for two runs. The radiant energy represented by  $_1 T^4$  is plotted against the chart reading. Since the curves are not truly linear, the thermopile output obviously is not precisely proportional to  $T^4$ .

The measured emissivity as observed by the thermopile was taken to be the ratio of the energy determined from the calibration curve at the chart reading produced by the gas emission to the energy  $T_c^4$  corresponding to black emission at the combustion temperature. The value of the constant  $\sigma$  is unimportant here since it cancels out in the ratio.

Special precautions were taken to determine the temperature of the blackbody as precisely as possible. Temperature readings were taken at several points in the interior of the cavity and the readings were not considered acceptable until the temperature of the back wall and the side wall of the cavity differed by no more than an indicated  $\pm 20^\circ F$ . The optical pyrometer was compared against a standard tungsten reference source (certified by U. S. Bureau of Standards) for temperatures up to  $4000^\circ R$ . The pyrometer calibration curve is shown in Fig. 4.3. The curve indicates that corrections of the order of  $50^\circ F$  were necessary at  $4000^\circ R$ . The required corrections for higher temperature we obtained by extrapolating the calibration curve.

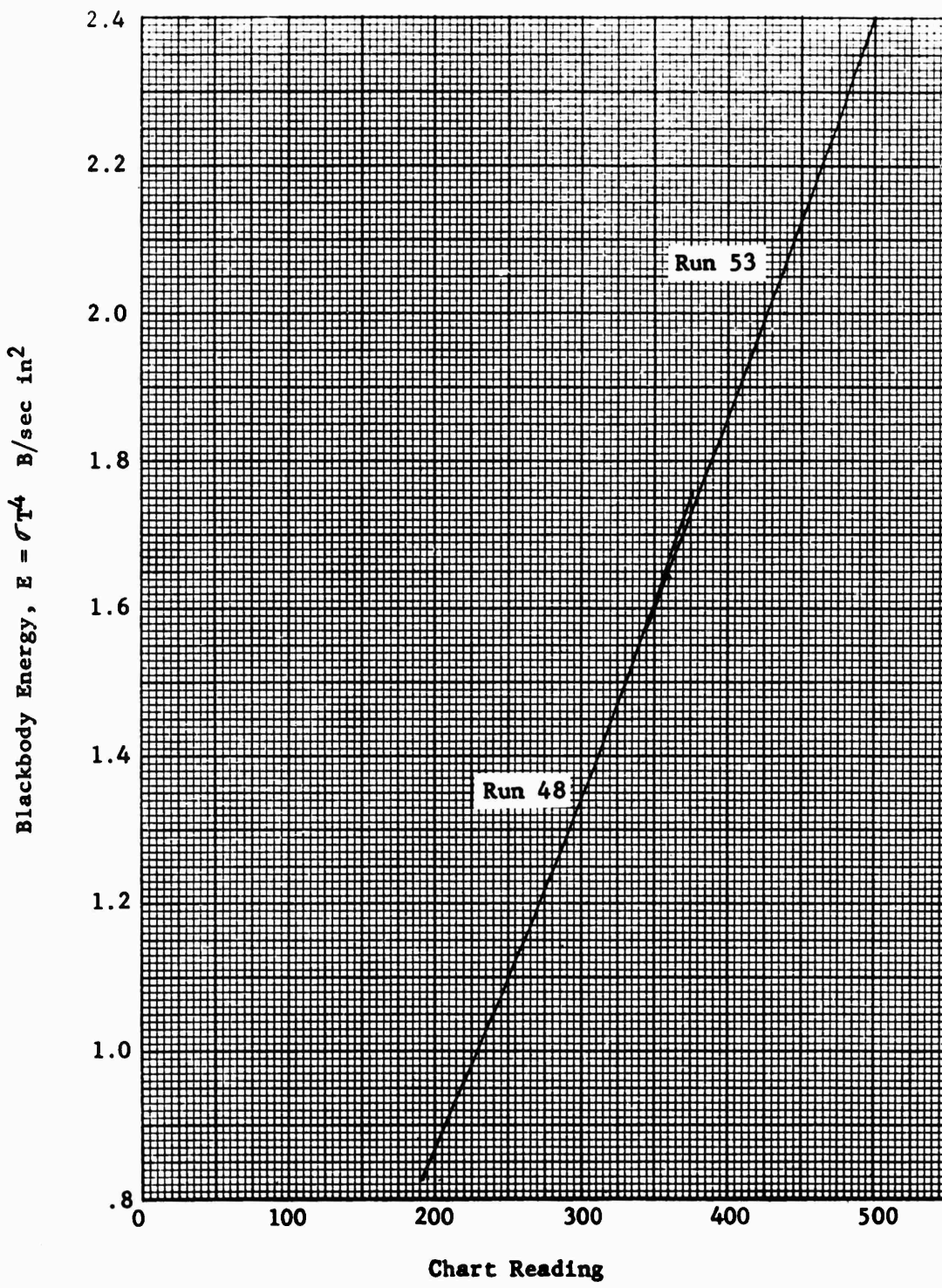


Fig. 4.2 Thermopile Calibration

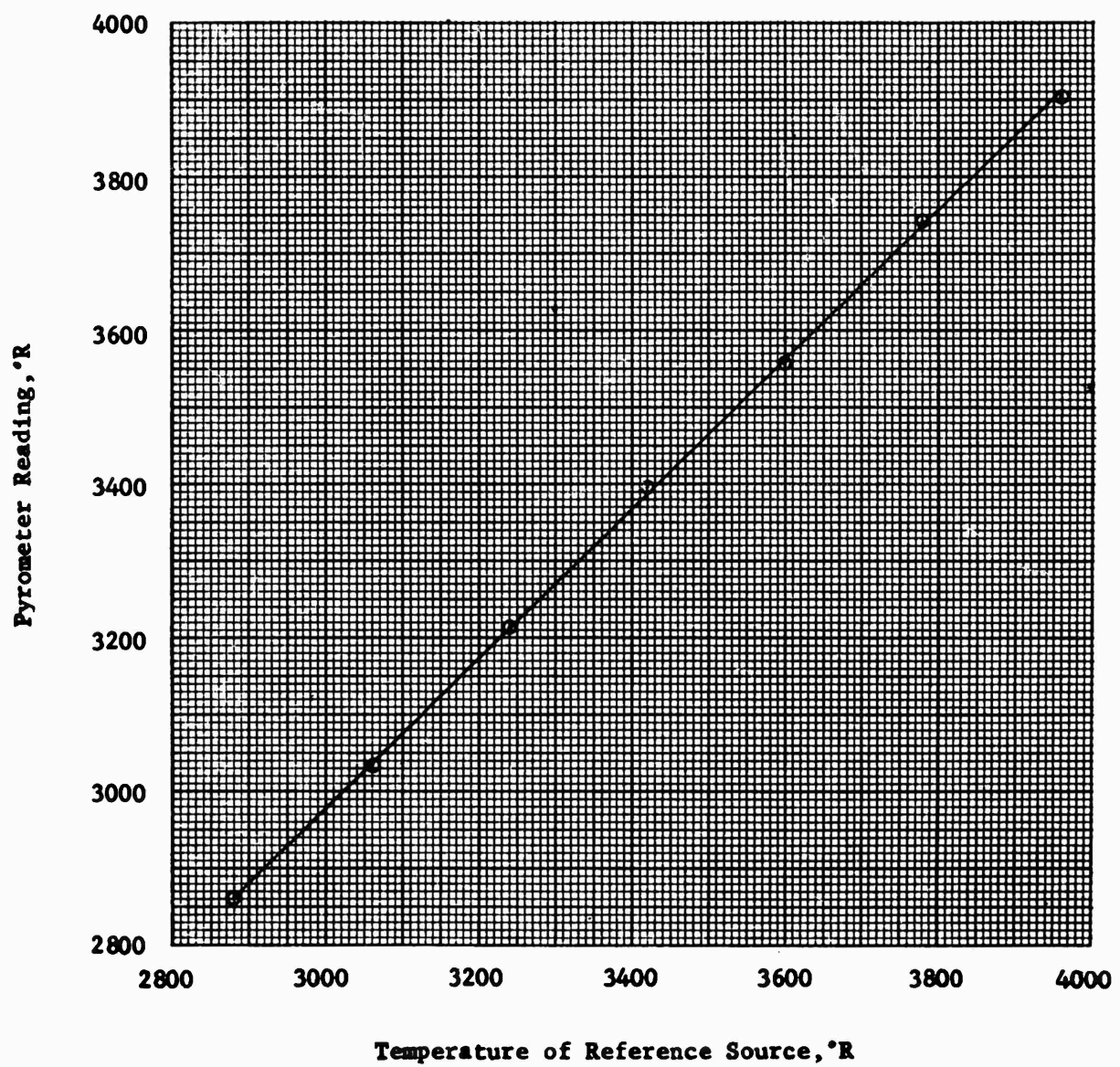


Fig. 4.3 Pyrometer Calibration

Corrections. Several corrections must be applied to obtain the true emissivity of the gas from the measured values. The most critical of these is the correction needed to account for the radiation reflected from the back wall of the combustion chamber. The equations required for the reflection correction are discussed in detail in a previous section (see Eqs. 2.63 and 2.65). The critical aspect regarding this correction is that for moderate emissivity values, the reflected energy is of the same order of magnitude as the energy emitted in line of sight through the observation aperture, and an error in determining the reflectivity of the background surface could produce a significant error in determining the true emissivity of the gas. The effect of the reflectivity  $f$  on the emissivity is illustrated in Figs. 4.4 and 4.5. Effective absorption coefficients of up to 0.16 were obtained in the present experiments. Figure 4.4 shows that a value of  $f = 1$  would yield a value of  $\epsilon_m$  of 8.745 compared with a value of  $\epsilon_m = 0.495$  if  $f = 0$ . The true emissivity in each case is obtained from the curve  $f = 0$ . This, if  $\epsilon_m = 0.745$  and  $f = 1$ ,  $\epsilon_{(f=0)} = 0.745$ . Thus, an uncertainty of at least 50% would exist in determining the value of the true emissivity if the reflectivity of the wall were unity. The percentage error is higher for low values of  $\mu$ . The effect of the reflectivity becomes negligible as the emissivity approaches unity.

The cold background surface was sandblasted copper. The reflectivity of the surface of this type are not described adequately in the literature. According to the literature<sup>(11)</sup>, the reflectivity of copper may vary from 0.24 for rough or buffed surface to 0.99 for highly polished surfaces. The reflectivity of copper apparently is also very sensitive to the slate of oxidation.

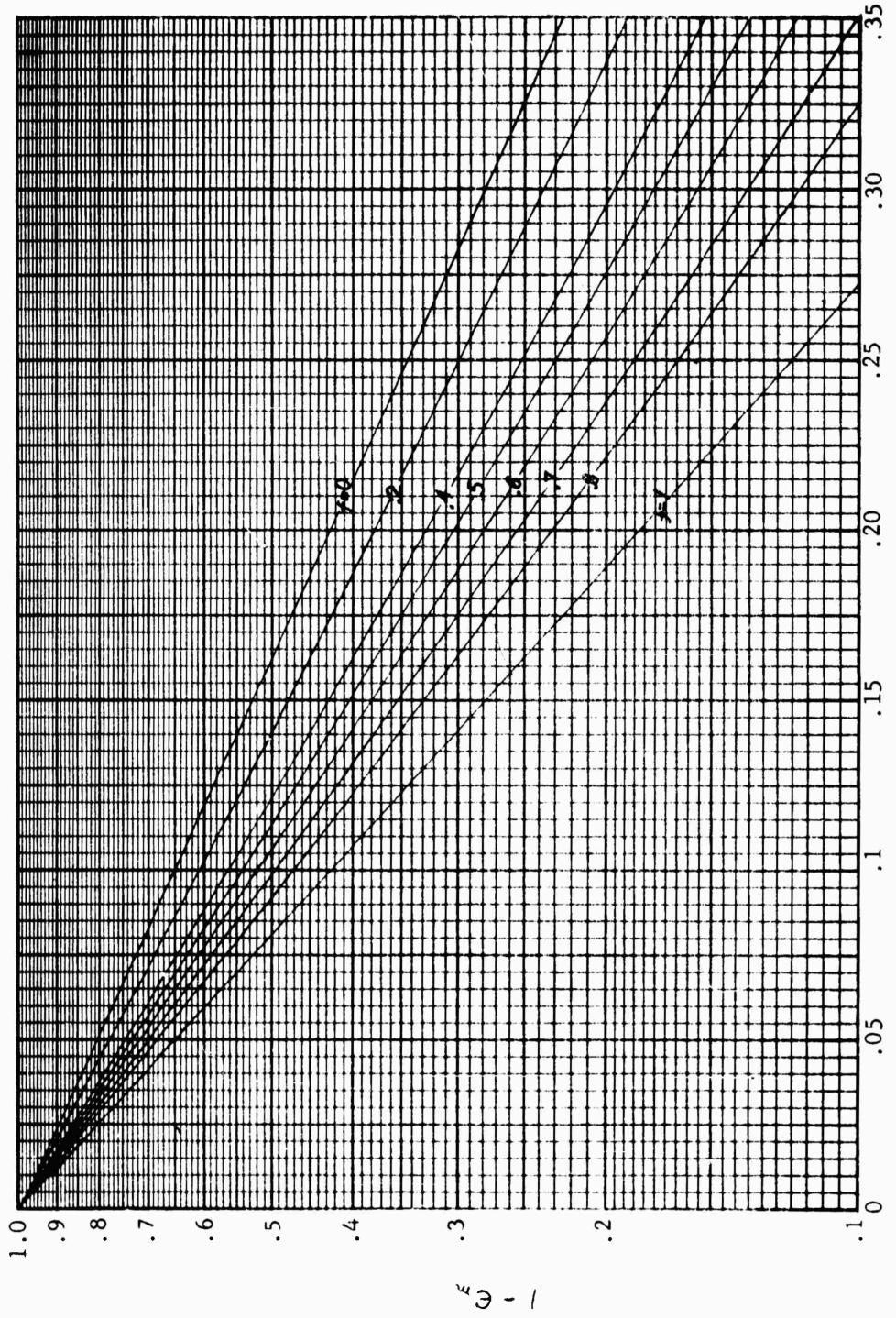


Fig. 4.4 Effect of Back Wall Reflection on the Observed Emissivity

Fig. 4.4 Effect of Back Wall Reflection on the Observed Emissivity

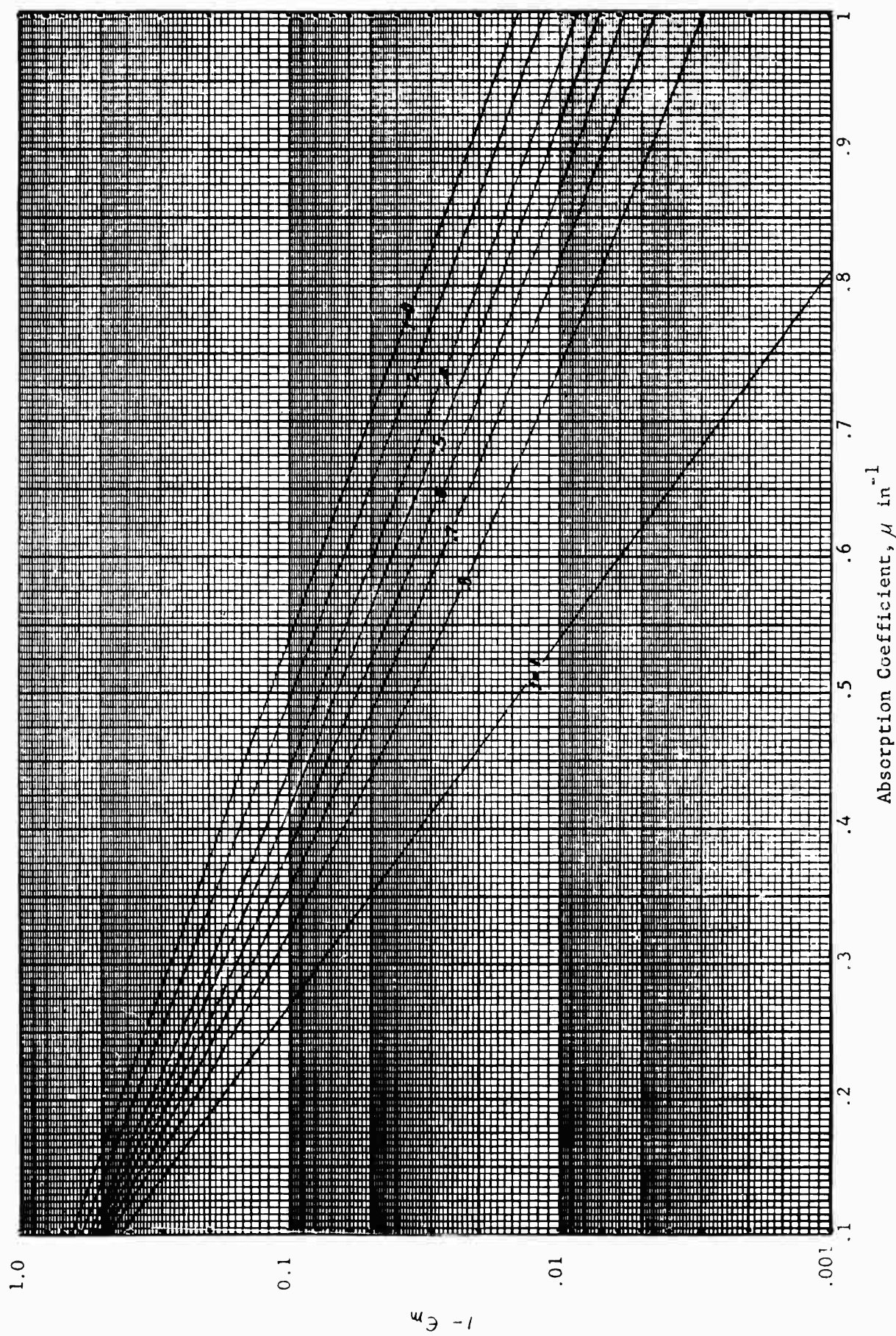


Fig. 4.5 Effect of Back Wall Reflection on the Observed Emissivity

Because of the wide variances in the reported reflectivities, it was necessary to measure the reflectivity of the actual background surface. The monochromatic reflectivity of the surface was determined by comparing the intensity of the light reflected normally from the background surface with, the intensity of the light reflected from a front surface optical mirror. A tungsten lamp was used as the light source. The reflectivity of the mirror was assumed to be unity. The reflectivity of the clean sandblasted surface was found to be less than 10% for all wavelengths. The reflectivity rose from nearly zero for wavelengths less than  $1\mu$  to a maximum of slightly over 7% between  $3\mu$  and  $4\mu$  and then decreased uniformly to approximately 1% at  $9\mu$ . The experimental data were fitted with a third degree equation for calculation purposes. The values determined from this equation are listed as  $f_\lambda$  in Table 3.

In order to show the effect of the reflectivity on the spectral emissivity and absorption coefficient, a separate calculation was made for Run 43 and Run 53 using a constant reflectivity of  $f_\lambda = 0.24$ . This value is the best estimate available from the literature. The results of these calculations are listed in Table 6. A comparison of the emissivities  $\epsilon_\lambda$  listed in Table 6 with those listed in Table 3 shows that the effect on  $\epsilon_\lambda$  is less than 10%.

In addition to the correction for the reflected energy, the spectrometer data required one other correction. The numerical integration was carried out only for wavelengths between  $1.14\mu$  and about  $10\mu$ . It is necessary, therefore, to account for the energy that appears in the spectrum above the upper integration limit and below the lower limit. The emissivity was assumed to be zero for wavelengths smaller than  $1.14\mu$ , unity for wavelengths greater than the upper integration limit. The total emissivities designated by  $\epsilon$  in Table 3 account for these corrections.

Table 6. Spectral Properties Based on a Background Reflectivity of  $f = 0.24$   
 RUN NO. 45 [H<sub>2</sub>O] 0.5875  $T_c$  4123 OR

$\lambda$ micron	$\epsilon_{m\lambda}$	$f_\lambda$	$\mu_\lambda$	$\epsilon_\lambda$
1.140+00	6.297-02	2.400-01	1.236-02	5.129-02
1.163+00	5.267-02	2.400-01	1.028-02	4.283-02
1.186+00	4.374-02	2.400-01	8.489-03	3.552-02
1.209+00	3.909-02	2.400-01	7.566-03	3.172-02
1.220+00	4.463-02	2.400-01	8.667-03	3.625-02
1.231+00	5.707-02	2.400-01	1.116-02	4.644-02
1.243+00	8.548-02	2.400-01	1.701-02	6.988-02
1.256+00	1.271-01	2.400-01	2.594-02	1.046-01
1.271+00	2.119-01	2.400-01	4.571-02	1.769-01
1.286+00	2.962-01	2.400-01	6.787-02	2.511-01
1.301+00	3.601-01	2.400-01	8.672-02	3.089-01
1.316+00	4.623-01	2.400-01	1.217-01	4.045-01
1.331+00	4.845-01	2.400-01	1.302-01	4.258-01
1.346+00	5.274-01	2.400-01	1.480-01	4.677-01
1.361+00	5.215-01	2.400-01	1.454-01	4.618-01
1.376+00	5.246-01	2.400-01	1.468-01	4.649-01
1.392+00	5.145-01	2.400-01	1.425-01	4.550-01
1.414+00	5.121-01	2.400-01	1.415-01	4.526-01
1.458+00	4.612-01	2.400-01	1.213-01	4.034-01
1.479+00	4.186-01	2.400-01	1.059-01	3.631-01
1.501+00	3.601-01	2.400-01	8.672-02	3.089-01
1.523+00	3.088-01	2.400-01	7.143-02	2.624-01
1.545+00	2.654-01	2.400-01	5.945-02	2.237-01
1.567+00	2.344-01	2.400-01	5.136-02	1.965-01
1.588+00	2.253-01	2.400-01	4.905-02	1.886-01
1.616+00	2.328-01	2.400-01	5.095-02	1.951-01
1.646+00	3.087-01	2.400-01	7.140-02	2.623-01
1.675+00	3.822-01	2.400-01	9.373-02	3.292-01
1.705+00	4.624-01	2.400-01	1.217-01	4.046-01
1.735+00	5.569-01	2.400-01	1.613-01	4.969-01
1.764+00	6.481-01	2.400-01	2.093-01	5.900-01
1.795+00	6.849-01	2.400-01	2.327-01	6.289-01
1.824+00	7.041-01	2.400-01	2.461-01	6.495-01
1.854+00	7.004-01	2.400-01	2.434-01	6.455-01
1.888+00	6.756-01	2.400-01	2.265-01	6.190-01
1.930+00	6.366-01	2.400-01	2.026-01	5.781-01
1.972+00	5.830-01	2.400-01	1.738-01	5.231-01
2.014+00	5.237-01	2.400-01	1.464-01	4.640-01
2.057+00	4.750-01	2.400-01	1.265-01	4.167-01
2.099+00	4.436-01	2.400-01	1.148-01	3.867-01
2.141+00	4.453-01	2.400-01	1.154-01	3.883-01
2.183+00	4.711-01	2.400-01	1.250-01	4.129-01
2.226+00	5.159-01	2.400-01	1.431-01	4.564-01
2.268+00	6.272-01	2.400-01	1.972-01	5.683-01
2.337+00	6.808-01	2.400-01	2.299-01	6.245-01
2.408+00	7.284-01	2.400-01	2.644-01	6.758-01
2.478+00	7.640-01	2.400-01	2.947-01	7.151-01
2.549+00	8.140-01	2.400-01	3.468-01	7.717-01
2.619+00	8.437-01	2.400-01	3.852-01	8.062-01
2.690+00	8.679-01	2.400-01	4.227-01	8.348-01

Table 6. (Continued)  
 RUN NO. 45 [H<sub>2</sub>O] 0.5875 T<sub>c</sub> 4123 °R

$\lambda$ micron	$\epsilon_{m\lambda}$	$f_\lambda$	$\mu_\lambda$	$\epsilon_\lambda$
2.761+00	8.866-01	2.400-01	4.569-01	8.572-01
2.831+00	8.996-01	2.400-01	4.844-01	8.730-01
2.902+00	9.121-01	2.400-01	5.145-01	8.883-01
2.988+00	8.941-01	2.400-01	4.723-01	8.663-01
3.084+00	8.400-01	2.400-01	3.800-01	8.019-01
3.181+00	7.638-01	2.400-01	2.946-01	7.149-01
3.277+00	6.809-01	2.400-01	2.300-01	6.246-01
3.374+00	6.219-01	2.400-01	1.942-01	5.628-01
3.470+00	5.561-01	2.400-01	1.609-01	4.961-01
3.567+00	4.872-01	2.400-01	1.313-01	4.284-01
3.663+00	4.711-01	2.400-01	1.250-01	4.129-01
3.760+00	4.586-01	2.400-01	1.203-01	4.010-01
3.856+00	4.725-01	2.400-01	1.256-01	4.143-01
3.953+00	5.033-01	2.400-01	1.373-01	4.441-01
4.049+00	5.497-01	2.400-01	1.579-01	4.897-01
4.243+00	6.496-01	2.400-01	2.102-01	5.916-01
4.436+00	7.473-01	2.400-01	2.800-01	6.966-01
4.629+00	8.531-01	2.400-01	3.990-01	8.173-01
4.809+00	9.398-01	2.400-01	6.009-01	9.227-01
4.976+00	9.998-01	2.400-01	1.935+00	9.997-01
5.142+00	9.272-01	2.400-01	5.574-01	9.069-01
5.309+00	9.487-01	2.400-01	6.376-01	9.339-01
5.475+00	9.307-01	2.400-01	5.687-01	9.113-01
5.642+00	8.120-01	2.400-01	3.444-01	7.694-01
5.809+00	9.125-01	2.400-01	5.155-01	8.888-01
5.975+00	9.417-01	2.400-01	6.082-01	9.251-01
6.142+00	9.685-01	2.400-01	7.503-01	9.591-01
6.307+00	8.890-01	2.400-01	4.617-01	8.601-01
6.451+00	8.081-01	2.400-01	3.399-01	7.649-01
7.028+00	8.825-01	2.400-01	4.489-01	8.523-01
7.605+00	8.662-01	2.400-01	4.198-01	8.328-01
8.068+00	9.999-01	2.400-01	2.098+00	9.999-01
8.517+00	9.481-01	2.400-01	6.350-01	9.331-01
8.943+00	9.999-01	2.400-01	2.098+00	9.999-01
9.348+00	9.999-01	2.400-01	2.098+00	9.999-01
9.748+00	9.999-01	2.400-01	2.098+00	9.999-01
1.013+01	9.999-01	2.400-01	2.098+00	9.999-01
1.050+01	9.999-01	2.400-01	2.098+00	9.999-01
1.085+01	9.999-01	2.400-01	2.098+00	9.999-01

Table 6. (Continued)

RUN NO. 53 [H2O] 0.4465 T<sub>c</sub> 5486 °R

$\lambda$ micron	$\epsilon_m \lambda$	$f_\lambda$	$\mu_\lambda$	$\epsilon_\lambda$
1.140+00	4.807-02	2.400-01	9.353-03	3.906-02
1.163+00	4.479-02	2.400-01	8.698-03	3.638-02
1.187+00	3.787-02	2.400-01	7.325-03	3.072-02
1.210+00	4.121-02	2.400-01	7.987-03	3.345-02
1.233+00	6.095-02	2.400-01	1.195-02	4.963-02
1.245+00	7.105-02	2.400-01	1.401-02	5.795-02
1.258+00	9.722-02	2.400-01	1.948-02	7.963-02
1.273+00	1.313-01	2.400-01	2.687-02	1.082-01
1.288+00	1.635-01	2.400-01	3.415-02	1.354-01
1.303+00	1.854-01	2.400-01	3.929-02	1.541-01
1.317+00	2.149-01	2.400-01	4.645-02	1.795-01
1.332+00	2.378-01	2.400-01	5.223-02	1.995-01
1.347+00	2.493-01	2.400-01	5.520-02	2.095-01
1.362+00	2.672-01	2.400-01	5.993-02	2.253-01
1.377+00	2.781-01	2.400-01	6.287-02	2.350-01
1.392+00	2.816-01	2.400-01	6.383-02	2.381-01
1.414+00	2.796-01	2.400-01	6.328-02	2.363-01
1.436+00	2.694-01	2.400-01	6.052-02	2.273-01
1.458+00	2.627-01	2.400-01	5.873-02	2.213-01
1.480+00	2.462-01	2.400-01	5.439-02	2.068-01
1.502+00	2.288-01	2.400-01	4.994-02	1.916-01
1.524+00	2.138-01	2.400-01	4.618-02	1.786-01
1.547+00	1.972-01	2.400-01	4.212-02	1.643-01
1.569+00	1.899-01	2.400-01	4.036-02	1.580-01
1.591+00	1.876-01	2.400-01	3.981-02	1.560-01
1.619+00	2.136-01	2.400-01	4.613-02	1.784-01
1.649+00	2.632-01	2.400-01	5.886-02	2.218-01
1.679+00	3.236-01	2.400-01	7.571-02	2.757-01
1.709+00	3.755-01	2.400-01	9.158-02	3.230-01
1.739+00	4.038-01	2.400-01	1.009-01	3.493-01
1.770+00	4.196-01	2.400-01	1.062-01	3.640-01
1.800+00	4.321-01	2.400-01	1.106-01	3.758-01
1.830+00	4.416-01	2.400-01	1.140-01	3.848-01
1.860+00	4.440-01	2.400-01	1.149-01	3.871-01
1.896+00	4.354-01	2.400-01	1.118-01	3.789-01
1.937+00	4.196-01	2.400-01	1.062-01	3.640-01
1.979+00	3.910-01	2.400-01	9.660-02	3.373-01
2.021+00	3.541-01	2.400-01	8.486-02	3.034-01
2.063+00	3.267-01	2.400-01	7.662-02	2.785-01
2.104+00	3.254-01	2.400-01	7.624-02	2.773-01
2.146+00	3.377-01	2.400-01	7.988-02	2.884-01
2.188+00	3.857-01	2.400-01	9.486-02	3.324-01
2.229+00	4.238-01	2.400-01	1.077-01	3.680-01
2.272+00	4.883-01	2.400-01	1.317-01	4.295-01
2.341+00	5.363-01	2.400-01	1.519-01	4.764-01
2.411+00	5.811-01	2.400-01	1.729-01	5.212-01
2.481+00	6.034-01	2.400-01	1.843-01	5.439-01
2.550+00	6.291-01	2.400-01	1.983-01	5.703-01
2.620+00	6.513-01	2.400-01	2.112-01	5.934-01
2.690+00	6.682-01	2.400-01	2.217-01	6.112-01

Table 6. (Continued)

RUN NO. 53 [H<sub>2</sub>C] 0.4465 T<sub>c</sub> 5486 °R

$\lambda$ micron	$\epsilon_{m\lambda}$	$f_\lambda$	$\mu_\lambda$	$\epsilon_\lambda$
2.759+00	6.897-01	2.400-01	2.360-01	6.340-01
2.829+00	7.064-01	2.400-01	2.477-01	6.519-01
2.899+00	6.882-01	2.400-01	2.349-01	6.324-01
2.983+00	6.570-01	2.400-01	2.147-01	5.994-01
3.081+00	6.261-01	2.400-01	1.966-01	5.672-01
3.178+00	5.718-01	2.400-01	1.683-01	5.118-01
3.274+00	5.199-01	2.400-01	1.448-01	4.603-01
3.373+00	4.780-01	2.400-01	1.277-01	4.196-01
3.470+00	4.384-01	2.400-01	1.129-01	3.818-01
3.567+00	4.221-01	2.400-01	1.071-01	3.664-01
3.665+00	4.093-01	2.400-01	1.027-01	3.544-01
3.762+00	4.279-01	2.400-01	1.091-01	3.718-01
3.859+00	4.460-01	2.400-01	1.156-01	3.890-01
3.956+00	4.710-01	2.400-01	1.250-01	4.128-01
4.054+00	5.051-01	2.400-01	1.386-01	4.458-01
4.151+00	5.314-01	2.400-01	1.497-01	4.716-01
4.248+00	5.672-01	2.400-01	1.661-01	5.072-01
4.346+00	5.898-01	2.400-01	1.772-01	5.300-01
4.443+00	6.194-01	2.400-01	1.929-01	5.603-01
4.540+00	6.465-01	2.400-01	2.084-01	5.884-01
4.637+00	6.707-01	2.400-01	2.233-01	6.138-01
4.734+00	6.858-01	2.400-01	2.333-01	6.298-01
4.818+00	7.205-01	2.400-01	2.583-01	6.672-01
4.902+00	7.500-01	2.400-01	2.823-01	6.996-01
4.985+00	7.392-01	2.400-01	2.732-01	6.877-01
5.069+00	7.543-01	2.400-01	2.860-01	7.043-01
5.153+00	7.603-01	2.400-01	2.914-01	7.110-01
5.237+00	7.773-01	2.400-01	3.074-01	7.300-01
5.320+00	7.776-01	2.400-01	3.076-01	7.303-01
5.404+00	8.162-01	2.400-01	3.494-01	7.743-01
5.488+00	7.703-01	2.400-01	3.006-01	7.221-01
5.571+00	7.273-01	2.400-01	2.636-01	6.746-01
5.655+00	7.348-01	2.400-01	2.696-01	6.828-01
5.739+00	7.611-01	2.400-01	2.921-01	7.119-01
5.823+00	7.675-01	2.400-01	2.980-01	7.190-01
5.906+00	7.512-01	2.400-01	2.833-01	7.009-01
5.990+00	7.148-01	2.400-01	2.539-01	6.610-01
6.753+00	8.866-01	2.400-01	4.569-01	8.572-01
7.472+00	9.165-01	2.400-01	5.262-01	8.937-01
8.084+00	9.999-01	2.400-01	2.098+00	9.999-01
8.656+00	9.966-01	2.400-01	1.270+00	9.955-01
9.164+00	9.999-01	2.400-01	2.098+00	9.999-01

Additional corrections were also applied to the emissivity data obtained from the thermopile. The thermopile observed the energy emitted by the gas and also the blackbody through a sapphire rod. Although sapphire transmits uniformly in certain regions of the spectrum, it has an upper and lower cut off point above and below which the transmission is essentially zero. The cut off wavelengths vary somewhat with thickness, but the upper cut off point (10% transmission) is about  $6\mu$ , while the lower value is about  $0.3\mu$ . The lower cut off point occurs in a region where the gas does not radiate and the required correction is not difficult. However, the emissivity of the gas is relatively high at wavelengths greater than  $6\mu$ , and the corrections necessary for this part of the spectrum are more involved. As it turns out, we must consider four separate zones to obtain the total correction.

Let  $a$ ,  $b$ ,  $c$ , denote respectively the low wavelength cut off, the high wavelength cut off, and the upper integration limit (see Table 3). The corrected emissivity is obtained by integrating over each zone and by dividing result by the total energy received from the blackbody. Thus,

$$\epsilon = \frac{\int_a^b \epsilon_\lambda B_\lambda d\lambda + \int_b^c \epsilon_\lambda B_\lambda d\lambda + \int_c^\infty \epsilon_\lambda B_\lambda d\lambda}{\int_0^\infty B_\lambda d\lambda} \quad (4.1)$$

The value of  $\epsilon$  from  $c$  to  $\infty$  is not known, but it is close to unity. Thus, for wavelengths greater than  $c$   $\epsilon$  will be taken to be unity. The energy emitted by the gas for wavelengths between  $b$  and  $c$  can be approximated closely by utilizing a mean value of the emissivity, which will be denoted by  $\bar{\epsilon}$ . The energy actually detected by the thermopile, from the blackbody as well as the gas occurs at wavelengths between  $a$  and  $b$ . Thus, the measured emissivity is actually

$$\epsilon_m = \frac{\int_a^b \epsilon_\lambda B_\lambda d\lambda}{\int_a^b B_\lambda d\lambda} \quad (4.2)$$

With these definitions, Eq. 4.1 can be expressed as

$$\epsilon = \frac{\epsilon_m \int_a^b B_\lambda d\lambda + \bar{\epsilon} \int_b^c B_\lambda d\lambda + \int_c^\infty B_\lambda d\lambda}{\int_a^\infty B_\lambda d\lambda} \quad (4.3)$$

The ratio of each integral term in the numerator is simply the fraction of the black energy that appears in each zone. If we let  $B_{va}$ ,  $B_{vb}$ , and  $B_{vc}$  denote respectively the fractions of energy that lies below wavelengths  $a$ ,  $b$ , and  $c$ , Eq. 4.3 becomes

$$\epsilon = \epsilon_m (B_{vb} - B_{va}) + \bar{\epsilon} (B_{vc} - B_{vb}) + 1 - B_{vc} \quad (4.4)$$

The fraction of black radiation  $B_v$  that occurs below a given wavelength  $\lambda_1$  is given as a function of  $\lambda_1 T$  in Ref. 10 and 13.

## LIST OF PRINCIPAL SYMBOLS

a, b, c	empirical coefficients
A	area, detector surface and nozzle flow
A <sub>1</sub>	area, background surface
B	areal intensity of black radiation
B <sub>v</sub>	fraction of black radiation from 0 to 1
c <sub>p</sub>	constant pressure, specific heat
c <sub>1</sub> , c <sub>2</sub>	constants in Planck's equation
d	diameter of experimental chamber
d <sub>e</sub>	effective beam length of experimental chamber
e	base for natural logarithm
E	observed radiant flux (thermopile)
f	reflectivity of background surface
F	radiant flux,
H	enthalpy of combustion gases
I	areal intensity of gas radiation
I <sub>f</sub>	reflected intensity
J	integral
J	heat equivalent of work
k	specific heat ratio
K	modulus of elliptic integral
L	general effective beam length
L	length of experimental chamber
m	mass

$m$	propellant mass flow rate
$p$	partial pressure
$p_c$	combustion pressure
$q$	radiant heat transfer rate
$Q$	nozzle heat rejection rate
$r$	radius or radius vector
$R$	specific gas constant
$T$	temperature
$T_c$	calculated combustion temperature
$T'_c$	theoretical combustion temperature
$V$	volume and velocity
$x, y, z$	Cartesian coordinates

#### GREEK

$\alpha$	angle of view
$\beta$	temperature calculation parameter
$\delta$	geometrical variable, diameter-to-length ratio
$\epsilon$	emissivity
$\epsilon$	emission coefficient
$\zeta$	geometrical variable, length-to-length ratio
$\rho, \psi, r$	spherical coordinates
$\kappa$	mass absorption coefficient
$\lambda$	wavelength
$\mu$	absorption coefficient
$\rho$	density of combustion gas

## GREEK (Continued)

$\rho, \alpha$	polar coordinates
$\sigma$	Stefan-Boltzmann constant
$\phi$	function
$\omega, \Omega$	solid angle

## SUBSCRIPTS

a	lower cut off point for thermopile system
b	upper cut off point for thermopile system
c	wavelength limit of measured spectral data
c	chamber
m	measured property
n	nozzle
o	initial
t	throat
$\lambda$	spectral or monochromatic property

## REFERENCES

1. S. S. Penner, Quantitative Molecular Spectroscopy and Gas Emissivities, Addison Wesley Publishing Company, Inc., Reading, Mass., 1959.
2. G. Herzberg, Molecular Spectra and Molecular Structure, I, D. Van Nostrand Co., New York, 1953.
3. W. Heitler, The Quantum Theory of Radiation, Clarendon Press, Oxford, 1954.
4. H. C. Hottel, Chapter III, Heat Transmission by W. C. Adams, 3rd Ed., McGraw Hill Book Co., New York, 1954.
5. R. W. Kebler, Optical Properties of Sapphire, Linde Air Products Company, New York.
6. J. N. Howard, D. C. Burch, D. Williams, Geophysical Research Paper No. 40, AFRC-TR 55 213, Ohio State University, Columbus, 1955.
7. M. Jacob, Heat Transfer II, John Wiley & Sons, Inc., New York, 1957.
8. S. Chandrasechar, Radiative Transfer, Clarendon Press, Oxford, 1950.
9. S. S. Ballard, K. A. McCarthy, and W. L. Wolfs, Optical Materials for Infrared Instrumentation, Report No. 2389-11-S. The University of Michigan, Willow Run Laboratories, 1960.
10. S. Flugge, Handbuch der Physik, Band XXVI Licht und Materie, Springer, Verlag, Berlin, 1958.
11. G. G. Gubareff, J. E. Janssen, R. H. Torborg, Thermal Radiation Properties Survey, Second Edition, Honeywell Research Center, Minneapolis, 1960.
12. V. Kourganoff, Basic Methods in Transfer Problems (Radiative Equilibrium and Neuter Differences), Clarendon Press, Oxford, 1952.
13. M. Czerny, Z. Physik 139, 302, 1954.
14. M. J. Zucrow, Aircraft and Missile Propulsion, II, John Wiley & Sons., Inc, 1958.
15. A. H. Shapiro, The Dynamics and Thermodynamics of Compressible Fluid Flow, I, The Ronald Press Company, New York, 1953.

## APPENDIX A

### PERFORMANCE AND PROPELLANT DATA

Theoretical values of the characteristic velocity and combustion temperature are shown in Figs. 5.1, 5.2, and 5.3 for the three propellant systems studied in this report.

Typical values of the calculated equilibrium composition of the products for the different propellant combinations are listed in Table 7.

Table 8 provides a list of each test run conducted for the present investigation.

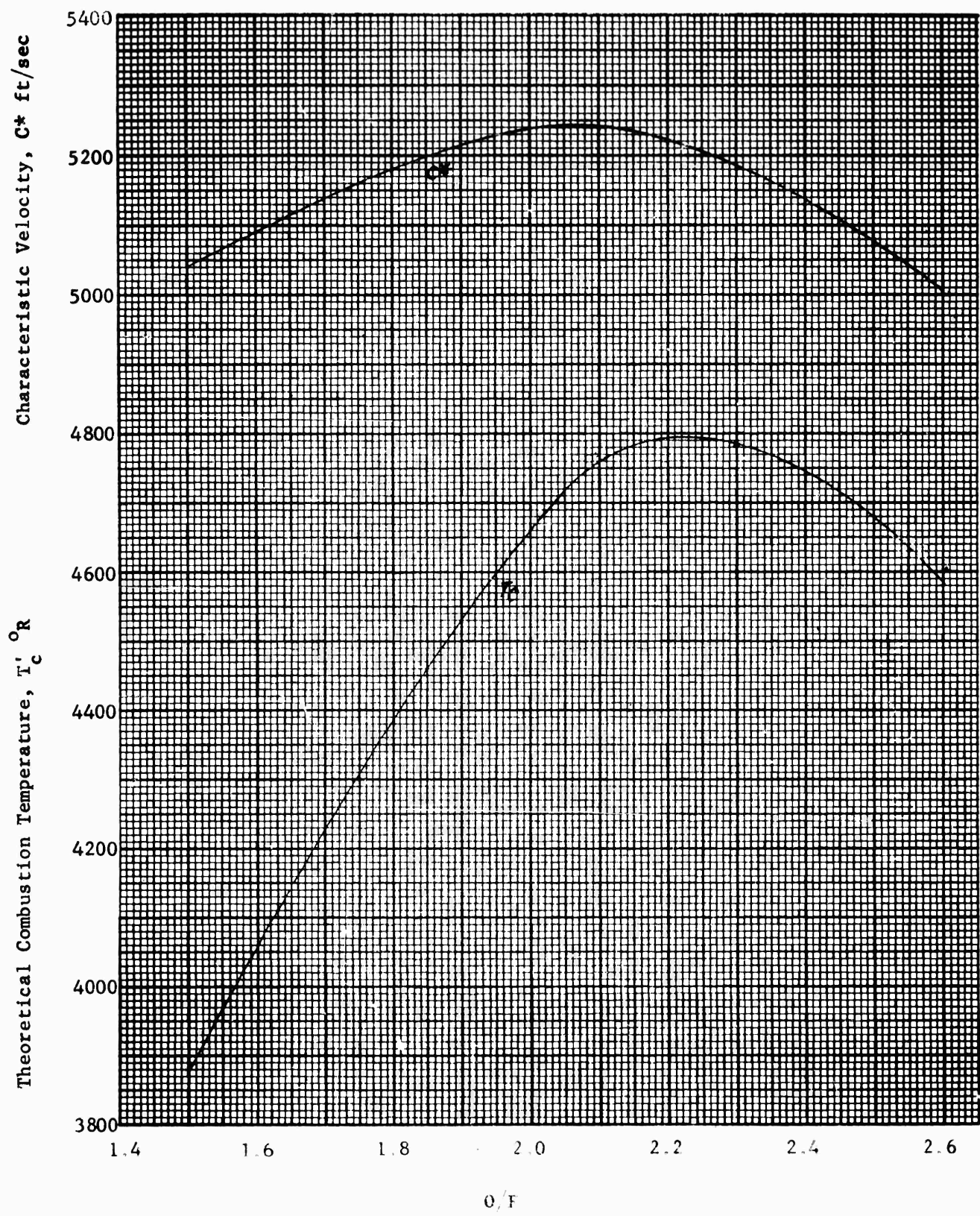
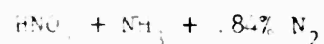


Fig. 5.1. Theoretical Performance at  $p_c = 700$  psia



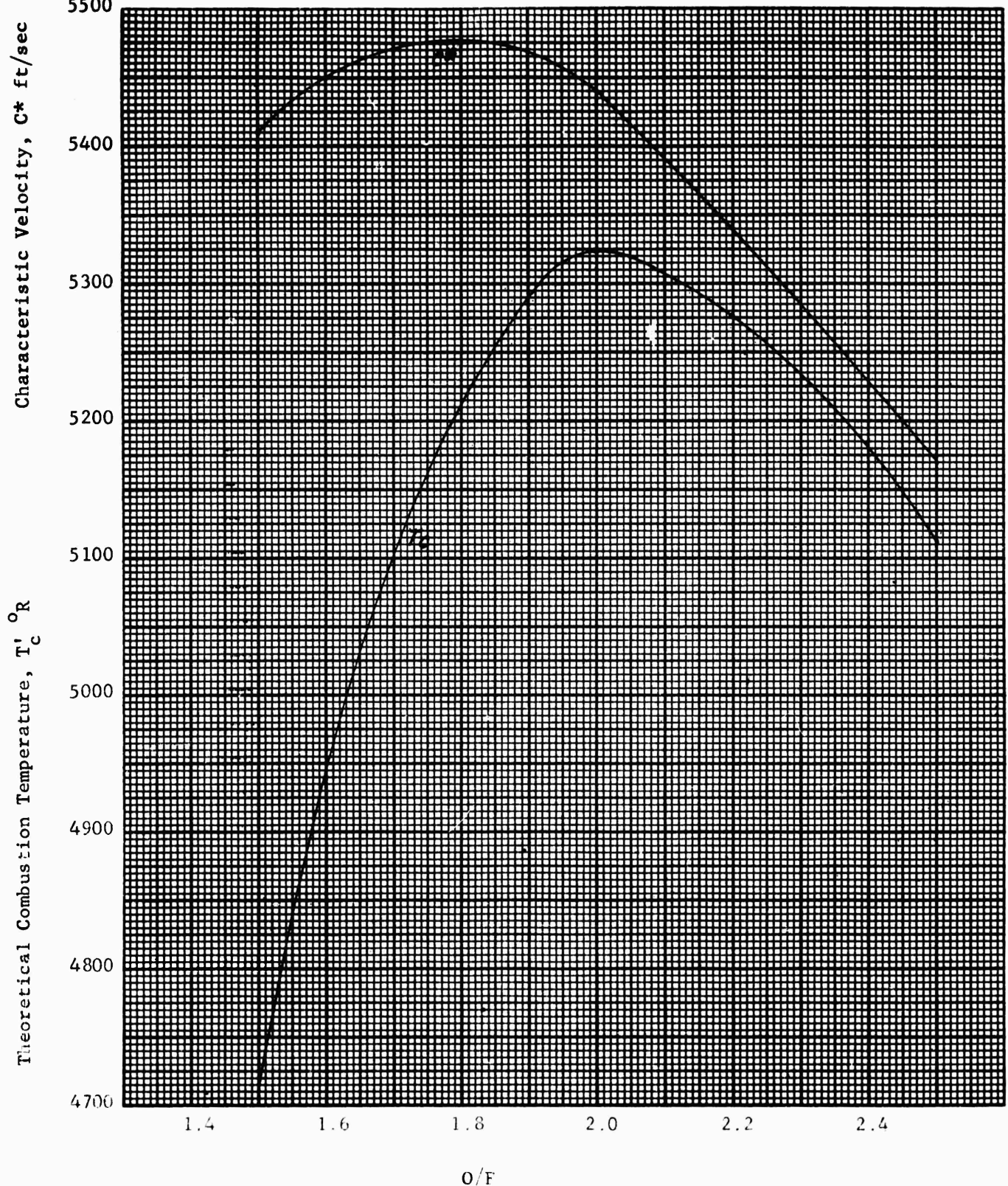


fig. 5.2 Performance Characteristics of  
 $N_2O_4 - NH_3 + .9\% N_2$

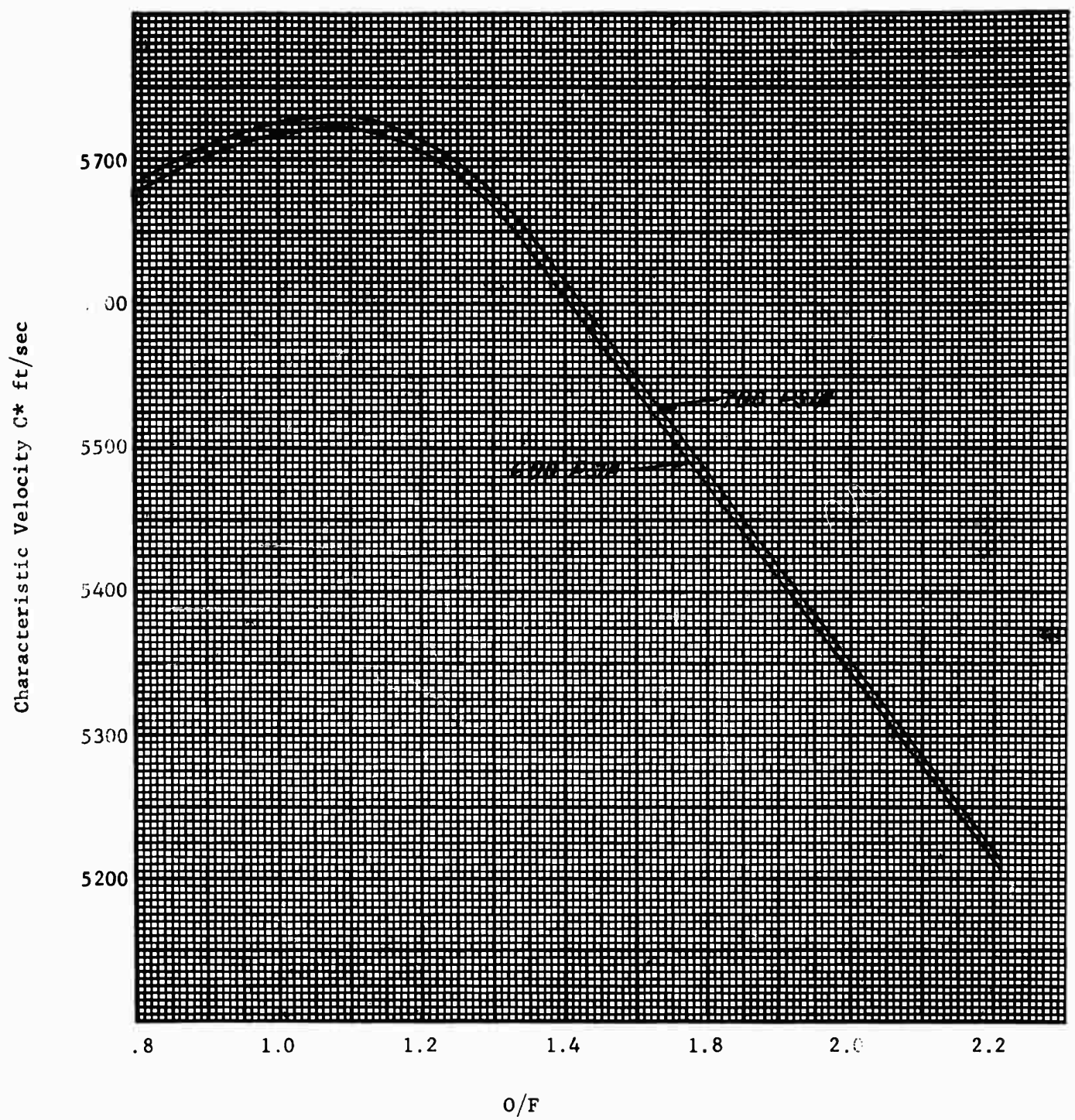


Fig. 5.3. Theoretical Performance of  $N_2O_4 - N_2H_4 + 1\% N_2$

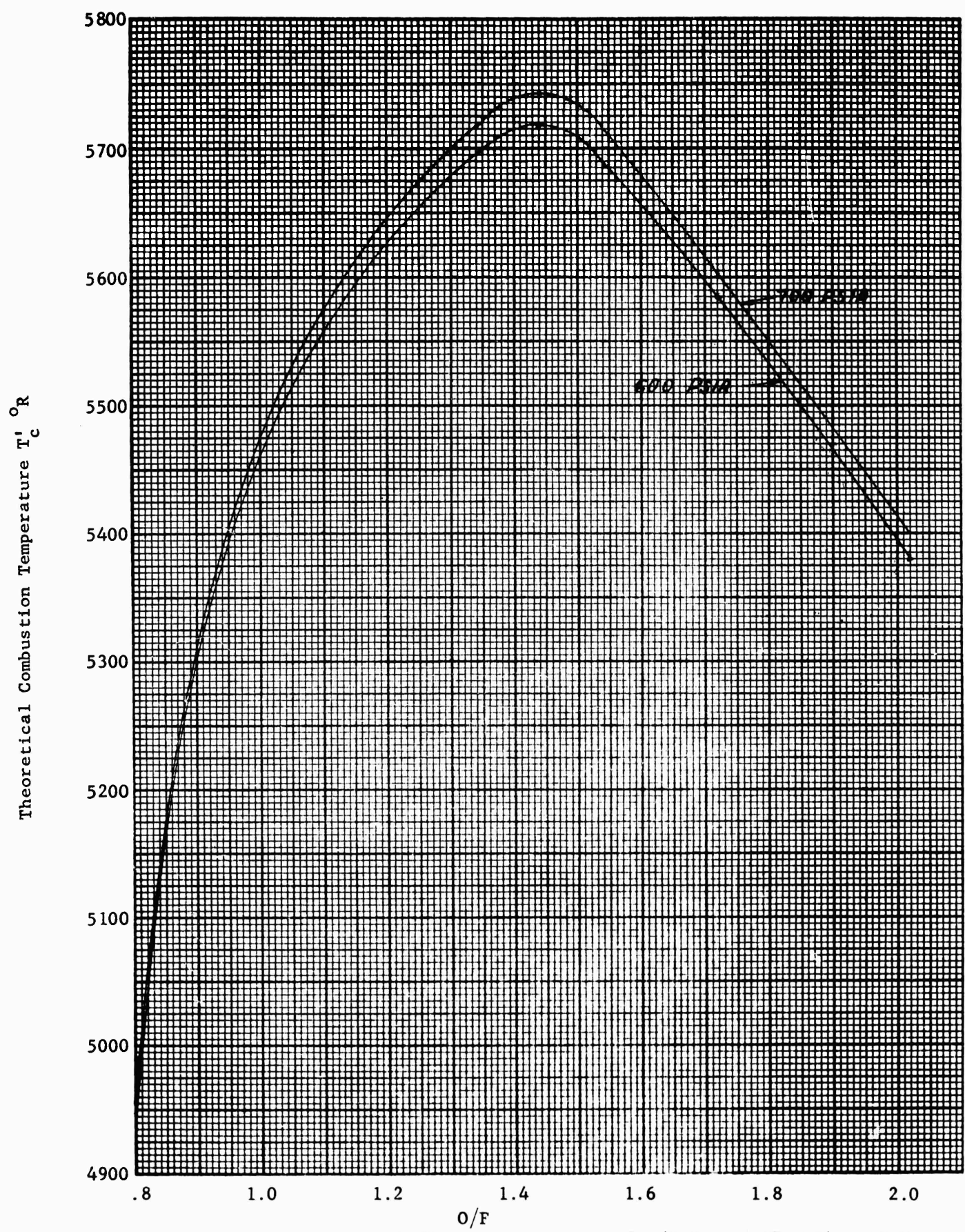


Fig. 5.4. Theoretical Flame Temperature  $N_2O_4 - (N_2H_4 + 1.7\% H_2O) + 1\% N_2$

Table 7. Typical Propellant Composition

	N <sub>2</sub>	H <sub>2</sub> O	O <sub>2</sub>	OH	H	O	H <sub>2</sub>	NO
NH <sub>3</sub> +(HNO <sub>3</sub> , 1.05% H <sub>2</sub> O) + .84% N <sub>2</sub>	.30473	.64689	0	.00552	.00137	.00013	.04017	.00119
O/F = 1.10 P <sub>c</sub> = 700 psia T <sub>c</sub> = 4768 R								
O/F = 1.80 P <sub>c</sub> = 700 psia T <sub>c</sub> = 4383	.30002	.58007	0	.00092	.00095	0	.11792	.00009
NH <sub>3</sub> +N <sub>2</sub> O + .9% N <sub>2</sub> O/F = 2.00 P <sub>c</sub> = 700 psia T <sub>c</sub> = 5324 R	.35381	.56449	.00741	.01933	.00395	.00132	.03769	.00599
O/F = 1.50 P <sub>c</sub> = 700 psia T <sub>c</sub> = 4712 R	.34449	.48159	.00002	.00171	.00248	.00002	.16951	.00018
N <sub>2</sub> O <sub>4</sub> +(N <sub>2</sub> H <sub>4</sub> +1.7% H <sub>2</sub> O) + 1% N <sub>2</sub>	.40305	.43576	.00089	.01338	.01110	.00072	.13250	.00258
O/F = 1.10 P <sub>c</sub> = 600 psia T <sub>c</sub> = 5575 R								

Table 8. List of Experimental Tests

Run No.	Ox.	Fuel	P <sub>c</sub> psia	O/F	Run Time sec	C* ft./sec	Remarks
1	HNO <sub>3</sub>	NH <sub>3</sub>	640	2.76	10.23	5103	
2			724	1.90	60.75	5080	
3			775	1.73	7.97	5125	
4			721	2.46	61.73	4883	
5							Fuel Flow Obstructed
6			696	2.38	30.68	5260	
7			346	1.92	8.12	4954	
8			730	1.98	11.50	5285	
9			680	1.77	20.48	4754	
10			688	1.70	20.07	4813	
11			704	2.06	15.42	5000	
12			705	1.90	15.40	4939	
13			698	1.55	17.88	5103	
14			698	1.83	8.33	4270	
15					6.43		Hardware Checkout
16			740	1.84	23.48	5086	
17			702	1.56	40.64	4634	
18			711	1.95	24.91	4821	
19	HNO <sub>3</sub>	NH <sub>3</sub>	714	2.20	41.38	4866	

Table 8. (Continued)

Run No.	Ox.	Fuel	P <sub>c</sub>	O/F	Run Time sec	C*	Remarks
			psia			ft./sec.	
20	HNO <sub>3</sub>	NH <sub>3</sub>			7.13		Hardware Checkout
21			710	1.82	39.29	4714	
22			758	1.91	40.48	5128	
23			733	1.54	59.56	4770	
24			728	1.79	59.64	4895	
25			714	1.84	60.05	4909	
26			678	1.86	31.13	4790	
27					89.37		Unreliable Data
28					60.20		Unreliable Data
29					90.19		Unreliable Data
30			683	1.59	58.10	4565	
31			674	1.875	94.60	4711	
32			717	1.66	40.55	4798	
33			762	1.85	96.38	5167	
34			692	1.78	60.17	5158	
35			700	2.49	99.22	4319	
36			730	2.38	100.20	4665	
37			709	2.35	102.08	4293	
38	HNO <sub>3</sub>	NH <sub>3</sub>	706	2.02	104.38	4936	

Table 8. (Continued)

Run No.	Ox.	Fuel	P <sub>c</sub> psia	O/F	Run Time sec	C* ft./sec.	Remarks
39	HNO <sub>3</sub>	NH <sub>3</sub>	688	2.92	90.79	4509	
40			683	3.11	73.52	3944	
41			398	2.71	100.52	2283	
42			707	2.32	101.71	4909	
43*			697	2.13	100.21	5010	
44			683	2.16	58.99	4362	
45*			691	1.85	75.47	4810	
46*	HNO <sub>3</sub>	NH <sub>3</sub>	686	2.75	64.45	4608	
47*	N <sub>2</sub> O <sub>4</sub>	NH <sub>3</sub>	693	1.62	20.22	5080	Hardware Checkout
48*			702	1.99	70.17	5208	
49*			700	2.00	65.03	5253	
50*	N <sub>2</sub> O <sub>4</sub>	NH <sub>3</sub>	694	1.66	70.17	5297	
51*	N <sub>2</sub> O <sub>4</sub>	N <sub>2</sub> H <sub>4</sub>	608	1.11	18.82	5616	Hardware Checkout
52							Hardware Failure
53*			615	1.27	59.95	5598	
54*			700	1.39	65.05	5521	
55**			667	1.75	20.06	5584	
56	N <sub>2</sub> O <sub>4</sub>	N <sub>2</sub> H <sub>4</sub>	764	1.22	20.25	5636	

\* Spectograph and Thermopile Data Run

\*\* Thermopile Data Run Only

Table 9. Propellant Specifications

Nitrogen Tetroxide,  $N_2O_4$ , Mil. Spec. P-26539

Hydrazine,  $N_2H_4$ , Mil. Spec. P-26536, 1.7%  $H_2O$

Ammonia,  $NH_3$ , anhydrous 99.99% pure

Nitric Acid,  $HNO_3$  commercial white fuming, 1.05%  $H_2O$

DISTRIBUTION LIST

<b>ASTIA (TIPCR)</b> Arlington Hall Station Arlington 12, Virginia	(10 copies)	<b>Lewis Research Center (NASA)</b> Attn: Technical Library 21000 Brookpark Road Cleveland 35, Ohio	(1 copy)
<b>OTS, Dept. of Commerce</b> Technical Reports Branch Washington 25, D. C.	(1 copy)	<b>Wallops Station (NASA)</b> Attn: Technical Library Wallops Island, Virginia	(1 copy)
<b>AFOSR (SRGL)</b> Washington 25, D. C.	(2 copies)	<b>Institute of Technology (AU) Library</b> MCLI-LIB, Bldg. 125, Area B Wright-Patterson AFB, Ohio	(1 copy)
<b>RAND Corporation</b> 1700 Main Street Santa Monica, California	(2 copies)	<b>ASD (Lib)</b> Wright-Patterson AFB, Ohio	(1 copy)
<b>National Aeronautics &amp; Space Adminis.</b> Attn: Library 1520 H Street, N. W. Washington 25, D. C.	(1 copy)	<b>ARGMA (ORDXR-OTL)</b> Redstone Arsenal, Alabama	(1 copy)
<b>Ames Research Center (NASA)</b> Attn: Technical Library Moffett Field, California	(1 copy)	<b>Chief, R&amp;D Dept. of the Army</b> Attn: Scientific Information Branch Washington 25, D. C.	(1 copy)
<b>High Speed Flight Station (NASA)</b> Attn: Technical Library Edwards AFB, California	(1 copy)	<b>Institute of the Aeronautical Sciences</b> 2 East 64th Street New York 21, New York	(1 copy)
<b>Langley Research Center (NASA)</b> Attn: Technical Library Langley AFB, Virginia	(1 copy)	<b>Applied Mechanics Reviews</b> Scuthwest Research Institute 8500 Culebra Road San Antonio 6, Texas	(2 copies)
<b>Chairman, Canadian Joint Staff (DRB/DSIS)</b> 2450 Massachusetts Avenue, N. W. Washington, D. C.	(1 copy)	<b>EOAR</b> The Shell Building 47 Rue Cantersteen Brussels, Belgium	(1 copy)
<b>Marshall Space Flight Center</b> Attn: Library Huntsville, Alabama	(1 copy)	<b>AFOSR (SRLTL)</b> Holloman AFB, New Mexico	(1 copy)
<b>AFCRL (Library)</b> L. G. Hanscom Field, Massachusetts	(1 copy)	<b>AFFTC (Library)</b> Edwards AFB, California	(1 copy)

AFSC (SCRS) Andrews AFB Washington 25, D. C.	U. S. Atomic Energy Commission Tech. Information Service 1901 Constitution Avenue Washington 25, D. C. (1 copy)
AECD (Library) Arnold AF Stn, Tennessee (1 copy)	Commanding Officer White Sands Proving Ground Attn: Library White Sands, New Mexico (1 copy)
U. S. Naval Res. Lab. Library Washington 25, D. C. (1 copy)	Jet Propulsion Lab (NASA) CIT, Pasadena, California (1 copy)
ARL (Technical Library) Building 450 Wright-Patterson AFB, Ohio (1 copy)	Signal Corps Engineering Laboratory (SIGFM/EL-RPS) Fort Monmouth, New Jersey (1 copy)
AFSWC (Library) Kirtland AFB, New Mexico (1 copy)	Director, Ballistics Research Lab. Aberdeen Proving Ground Aberdeen, Maryland (1 copy)
Army Research Office Duke Station Attn: CRD-AA-IP Durham, North Carolina (1 copy)	Naval Ordnance Laboratory Attn: Library White Oak, Silver Spring, Maryland (1 copy)
National Bureau of Standards Attn: Library Washington 25, D. C. (1 copy)	AFSC (BSD) Attn: Library AF Unit PO Los Angeles 45, California (1 copy)
Chief of Naval Research Department of Navy Attn: Library Washington 25, D. C. (1 copy)	AFOSR (SRHP) OAR Washington 25, D. C. (1 copy)
Naval Bureau of Weapons Attn: Library Washington, D. C. (1 copy)	Brooklyn Polytechnic Institute Attn: Dr. Vito Agosta 99 Livingston Street Brooklyn, New York (1 copy)
North American Aviation Corporation Attn: Dr. R. B. Lawhead 6633 Canoga Avenue Canoga Park, California (1 copy)	Princeton University James Forrestal Research Center Attn: Dr. I. Glassman Princeton, New Jersey (1 copy)

General Electric Company  
Attn: Library  
3198 Chestnut Street (1 copy)  
Philadelphia 4, Pennsylvania

Sundstrand Tool Company  
Turbo Division  
Attn: Library  
Pacoima, California (1 copy)

Massachusetts Inst. of Technology  
Attn: Dr. T. Y. Toong  
Cambridge 39, Massachusetts (1 copy)

Armour Research Foundation  
Attn: Dr. T. P. Torda  
10 West 35th Street  
Chicago, Illinois

Liquid Propellant Information Agency  
Applied Physics Laboratory  
Johns Hopkins University  
8621 Georgia Avenue  
Silver Spring, Maryland (3 copies)

Harvard University  
Attn: Dr. H. Emmons  
Cambridge, Massachusetts (1 copy)

Ohio State University  
Department of Aeronautical Engineering  
Attn: Loren Bollinger  
Rocket Laboratory  
Columbus 10, Ohio (1 copy)

Reaction Motors Division  
Thiokol Chemical Company  
Attn: H. Wolfhard  
Denville, New Jersey (1 copy)

Purdue University  
Attn: Dr. J. Osborn  
Lafayette, Indiana (1 copy)

A. D. Little  
Attn: W. Tobey  
Cambridge, Massachusetts (1 copy)

General Electric Corporation  
Attn: Dr. D. Robison  
Cincinnati 15, Ohio (1 copy)

Hq USAF (AFDR)  
Attn: Col. P. Atkinson  
Washington 25, D. C. (1 copy)